

# Hydraulics

## 15. Hydraulics

The three segments of this chapter introduce phenomena that are of specific interest in the area of hydraulics. Where applicable (Cavitation, Sect. 15.1 and Sediment Transport, Sect. 15.3) introductory and descriptive material regarding the topic is provided. Terminology, physical examples and motivating descriptions introduce the comprehensive Cavitation subsection. Examples of the types of flows in which cavitation occurs are provided. This information sets the stage for a description of the types of facilities and instrumentation that are necessary to study the problem. Numerous photographs and descriptive sketches clarify and complement the text.

The wave height measurement segment first deals with fixed position single "point" techniques. More advanced techniques for: i) wave surface shape along a horizontal line, and ii) two-dimensional surface geometry measurements for laboratory and field observations are then described.

Following the introduction to sediment transport phenomena and terminology, the methods of measurement: manual, optical and acoustic are given detailed descriptions including calibration techniques for the latter two methods. Bed load sediment measurements: pressure difference, sediment trapping and acoustic are next described. Total load and the less common measurement techniques, plus references complete the subsection.

<b>15.1 Measurements in Cavitating Flows</b>	959
15.1.1 Fundamentals	961
15.1.2 Types of Cavitating Flows	967
15.1.3 Cavitation Damage	970
15.1.4 Facilities	972
15.1.5 Water Quality Measurements	979
15.1.6 Cavitation Inception	984
15.1.7 Measurements in Cavitating Flows	988
<b>15.2 Wave Height and Slope</b>	1009
15.2.1 Temporal Point Measurements at Fixed Geometric Positions	1009
15.2.2 One-Dimensional Spatial Measurements	1014
15.2.3 Two-Dimensional Spatial Measurements	1015
15.2.4 Special Surface Elevation Measurements for Large Laboratory or Field Use	1018
<b>15.3 Sediment Transport Measurements</b>	1020
15.3.1 A Brief Introduction to Sediment Transport	1020
15.3.2 Methods of Measuring Suspended Sediment Transport	1022
15.3.3 Bed Load Sediment Measurements	1029
15.3.4 Total Load Measurements	1032
15.3.5 Other Measurement Techniques	1032
<b>References</b>	1033

### 15.1 Measurements in Cavitating Flows

Cavitation is normally defined as the formation of the vapor phase in a liquid. The term cavitation (originally coined by R. E. Froude) can imply anything from the initial formation of bubbles (inception) to large-scale, attached cavities (supercavitation). The formation of individual bubbles and subsequent development of attached cavities, bubble clouds, etc., is directly related

to reductions in pressure to some critical value, which in turn is associated with dynamical effects, either in a flowing liquid or in an acoustical field. Cavitation can be distinguished from boiling in the sense that the former is induced by the lowering of the hydrodynamic pressure, whereas the latter is induced by the raising of the vapor pressure to some value in excess of the hy-

drodynamic pressure. The two phenomena are related. Cavitation inception and boiling can be compared in terms of the vapor-bubble dynamics of sub-cooled and superheated liquids [15.1]. Quite often a clear distinction between the two types of phenomena cannot be made. This is especially true for cavitation in liquids other than cold water.

Any device handling liquids is subject to cavitation. Cavitation can affect the performance of turbomachinery, resulting in a drop in head and efficiency of pumps and decreased power output and the efficiency of hy-

droturbines. The thrust of propulsion systems can be cavitation-limited and the process can degrade the accuracy of fluid meters. Noise and vibration occur in many applications. In addition to the deleterious effects of reduced performance, noise and vibration, there is the possibility of cavitation erosion. The extent of cavitation erosion can range from a relatively minor amount of pitting after years of service to catastrophic failure in a relatively short period of time as shown in Figs. 15.1, 2. Figure 15.1 illustrates the damage that can occur on a spillway. This damage occurred after only four hours of operation. The second example is cavitation damage in a hydraulic turbine due to the formation of secondary vortices in the outlet flow. *Arndt et al.* [15.2] have identified cavitation erosion in turbines as a very common problem.

Although cavitation is normally considered to be an undesirable effect or phenomenon, it sometimes serves useful purposes. Cavitation applications include ultrasonic cleaning and the homogenization of milk. Various chemical processes are enhanced by cavitation, such as coagulation, formation of suspensions and degassing of liquids. Cavitation can be used to increase heat and mass transfer in liquids, to promote crystallization and to enhance various sonochemical reactions such as polymerization and polymer degradation. Biomedical applications include the removal of kidney stones and automated drug delivery to patients. Important new applications in the pollution control area are of interest [15.3,4].

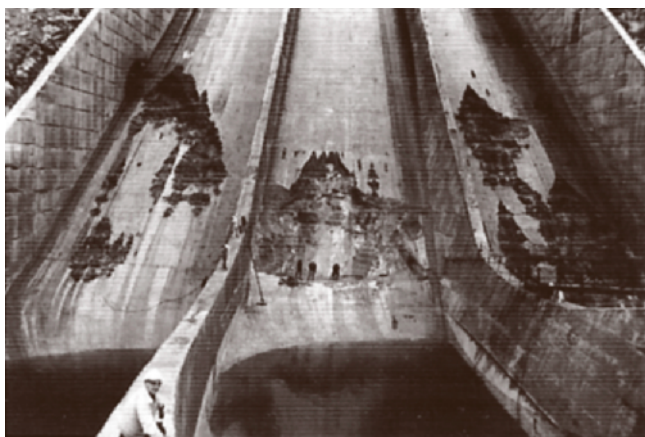


**Fig. 15.1** Example of cavitation damage on a spillway. The extent of the damage is evident when compared with the workmen in the figure. This damage occurred after only four hours of operation

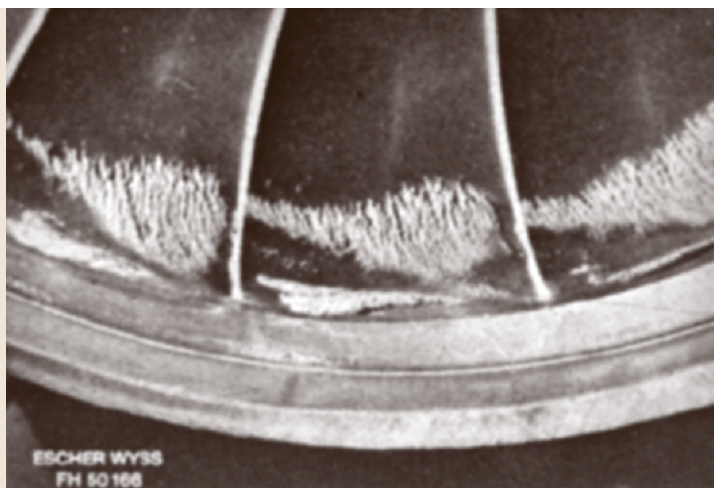
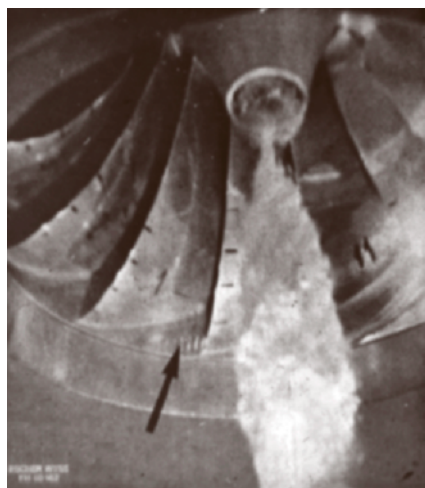


**Fig. 15.2** Example of vortex cavitation induced damage in a hydroturbine. Two types of cavitation are shown on the left, a hub vortex, and a secondary vortex pattern that develops in the runner passages as illustrated by the arrow. These relative small cavitating structures are responsible for the damage shown in the *inset* (Courtesy of A. Keller)

Cavitation has been studied for many years. Leonhard Euler is credited with being the first person to postulate the possibility of cavitation in his 1754 memoir on the theory of hydraulic machines. Osborne Reynolds (1894) carried out what was probably the first fundamental study of the problem by observing cavitation in tubular constrictions. The introduction of propellers for marine propulsion led to an almost immediate need for cavitation research. The most significant early example of applied research is probably that of Parsons in 1897 [15.5]. His approach to a cavitation problem sets the stage for the techniques used in modern research. The HMS Turbinia was designed by him to demonstrate the application of the compound steam turbine in marine propulsion. The first trials were miserable failures. Parsons examined this problem in a water tunnel with a special stroboscope, both of his own design. He determined that the heavily loaded single screw on the vessel was cavitating and was unable to produce the required thrust. His solution was to replace the original propulsion system with three smaller turbines with the same total horsepower driving nine propellers. A speed of 32.6 knots was finally achieved, amply demonstrating the application of steam turbine technology in marine propulsion. This brought fame and fortune to Parsons and his colleagues.

Other noteworthy efforts include the work of Barnaby and Thornycroft (1898), who were studying problems that evolved during the trials of the HMS Daring. This early work led to the classic study of the potency for damage due to bubble collapse by Lord Rayleigh [15.6]. Minnaert [15.7] then set the stage for understanding the acoustics of cavitation and gas-filled bubbles. The foundations of our knowledge of bubble dynamics and its interrelationship to cavitation are found in several papers by Plesset and his coworkers [15.1, 8, 9].

Because of the myriad of applications, cavitation research has been an active discipline for more than a century. The complex physics involved have dictated the development of sophisticated experimental techniques, innovative analytical methods and, more recently, the development of powerful numerical schemes for addressing the investigation of a broad variety of phenomena. An enormous quantity of literature has been written on the subject of cavitation. There are several reviews of the topic, e.g., Eisenberg [15.10], Wu [15.11], Acosta and Parkin [15.12], Plesset and Posperetti [15.13], Arndt [15.14–16], Blake and Gibson [15.17], and Rood [15.18].

The state of the art is well summarized in the textbook by Knapp et al. [15.19] and more recently by Young [15.20], Brennen [15.21] and Franc and Michel [15.22]. There are other texts in languages other than English. Notable examples are the exhaustive treatise by Anton [15.23] in Romanian and the text by Isay [15.24] in German. Numerous symposia have been devoted to the topic in the United States and elsewhere.

In spite of significant advances in computational techniques, there is still a need for experimental research. In fact, recent numerical studies have underscored the need for new experimental data, utilizing advanced experimental techniques. Recently cavitation research has been carried out utilizing an interactive numerical/experimental approach. One of the aims of this chapter is to illustrate how numerical and experimental approaches are integrated in modern cavitation research. Emphasis will be placed on the special instrumentation requirements for cavitation research that are in addition to the instrumentation required in single-phase fluid mechanics.

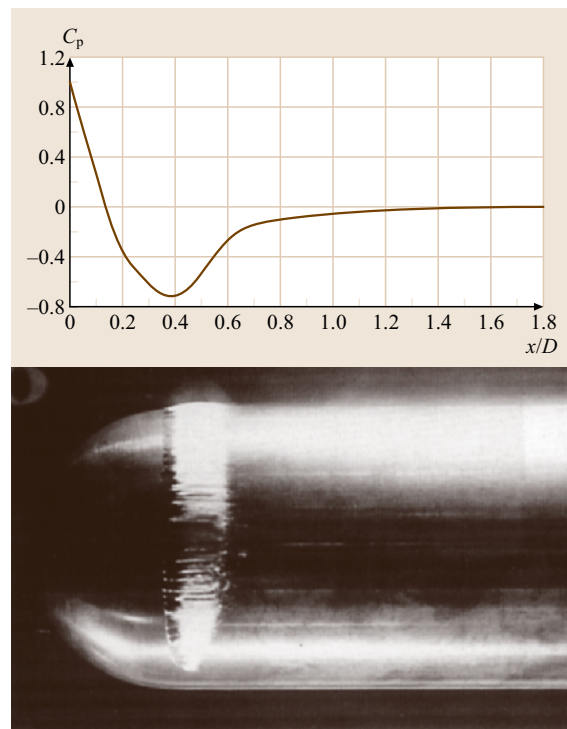


**Fig. 15.3** Cavitation inception on a hemispherical-nosed body. The curve in the top panel is the pressure distribution on the body (Courtesy of A. Keller)

### 15.1.1 Fundamentals

#### Occurrence of Cavitation

Examples of cavitation as viewed in the laboratory are shown in Figs. 15.3, 4, 5, 6, 7. Limited cavitation in the form of a ring of bubbles surrounding a hemispherical-nosed body is shown in Fig. 15.3. Note that when Fig. 15.3a,b are compared, cavitation appears to occur in a region that is downstream of the calculated minimum-pressure point. The pressure distribution in Fig. 15.3a was calculated using potential flow theory. Actually cavitation is occurring at the trailing edge of a laminar separation bubble that is not accounted for in the inviscid theory. Figure 15.4 is an outtake of high-speed video of an individual cavitation event on a National Advisory Committee for Aeronautics (NACA) 0015 hydrofoil. In this case inception begins very close to the minimum-pressure point on the foil. As the resulting vapor bubble moves downstream into a region of higher pressure it continues to grow. Finally the growth is arrested and the bubble collapses at about a length of  $3/4$  chord from the leading edge. After the initial collapse, the bubble rebounds and collapses again several times before the trailing edge is reached. Figure 15.5 illustrates cavitation occurring away from the surface of a body in a turbulent jet. Figure 15.6 contains some information on propeller cavitation. Figure 15.6a is an observation of cavitation on a model propeller in the University of Tokyo water tunnel. Note that cavitation occurs in the blade tip vortices and in the hub vortex. Figure 15.6b is a view, from a different perspective, of propeller cavitation made in one of the water tunnels at the Marine Institute of the Netherlands (MARIN). Note that there is a tip vortex and blade surface cavitation. The fact that several different types of cavitation can occur simultaneously in practice makes the scaling of these physical phenomena in the laboratory very challenging. Figure 15.7 is an example of cavitation on a hydrofoil and is presented to indicate several salient features of the cavitation problem. More than one type of cavitation can occur simultaneously (sheet cavitation on the surface of the blade, vortex cavitation at the tips). It is also important to note that in many practical applications cavitation is a nonsteady phenomenon. In a marine propeller for example, the degree of cavitation varies with the angular position of each blade due to the periodic passage of each propeller blade through the ship's wake. This induces periodic variations in thrust and torque that in some cases can cause severe vibration.

These examples illustrate the complexity of the cavitation process. It is clear that cavitation occurs in regions of low pressure. For example the calculation of minimum pressure in Fig. 15.3a was made using potential flow theory that ignores viscous effects. A shear layer associated with the instability of the separated flow in a separation bubble induces pressure fluctuations that are responsible for the incipient cavitation. Classical poten-



**Fig. 15.4** Bubble growth visualized with high-speed video. Flow is from left to right. Note that several rebounds occur after the initial collapse at about the  $3/4$  chord position



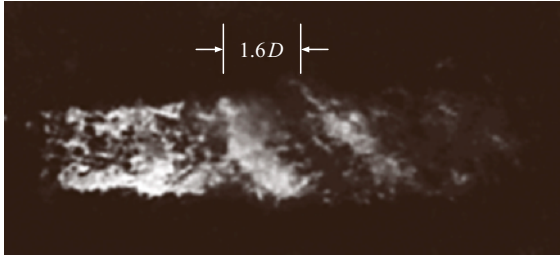


**Fig. 15.5** Cavitating jet. Note the existence of a *smoke-ring-like* structure close to the nozzle ( $m = 0$ ) and a helical structure ( $m = 1$ ) further downstream [15.25]

tial flow theory argues that the minimum pressure in a flow must occur at a boundary. This is clearly not the case for the turbulent flow shown in Fig. 15.5, which contains an example of jet cavitation. Careful inspection of the cavitation process in turbulent flows also indicates that cavitation occurs in vortical structures. The influence of vorticity on cavitation is also evident in Fig. 15.5. However, careful inspection of sheet cavitation as seen in Fig. 15.6 will also indicate the existence of highly vortical structures at the trailing edge of sheet cavitation. These photos only hint at the complexity of the problem.

### Cavitation Scaling

The fundamental parameter in describing the physics of the process is the cavitation index, defined by

$$\sigma = \frac{(p_0 - p_c)}{\frac{1}{2}\rho U_0^2}, \quad (15.1)$$

where  $p_0$  and  $U_0$  are a characteristic pressure and velocity, respectively,  $\rho$  is the density, and  $p_c$  is a critical pressure or cavity pressure depending on the application. Often  $\sigma$  is defined by setting  $p_c$  equal to the vapor pressure,  $p_v$ . Various hydrodynamics parameters such as lift and drag coefficient, torque coefficient, and efficiency, are assumed to be unique functions of  $\sigma$  when there is geometric similitude between the model and prototype. Generally speaking, these parameters are independent of  $\sigma$  above a certain critical value of  $\sigma$ . This critical value is often referred to as the incipient cavitation number. It should be emphasized that the point where there is a measurable difference in performance is not the same value of  $\sigma$  where cavitation can be first detected visually or acoustically.

The rationale for  $\sigma$  as a scaling parameter is as follows. Cavitation is normally assumed to occur when

the minimum pressure in a flow is equal to the vapor pressure. For steady flow over a streamlined body the nondimensional minimum pressure coefficient is given by

$$C_{p_m} \equiv \frac{p_m - p_0}{\frac{1}{2}\rho U_0^2}. \quad (15.2)$$

When  $p_m = p_v$ , the *incipient* value of  $\sigma$  is given by

$$\sigma_i = -C_{p_m}. \quad (15.3)$$

We can think of  $\sigma_i$  as a performance boundary such that for  $\sigma > \sigma_i$  there are no cavitation effects, while for  $\sigma < \sigma_i$  cavitation effects such as performance degradation, noise, and vibration occur.

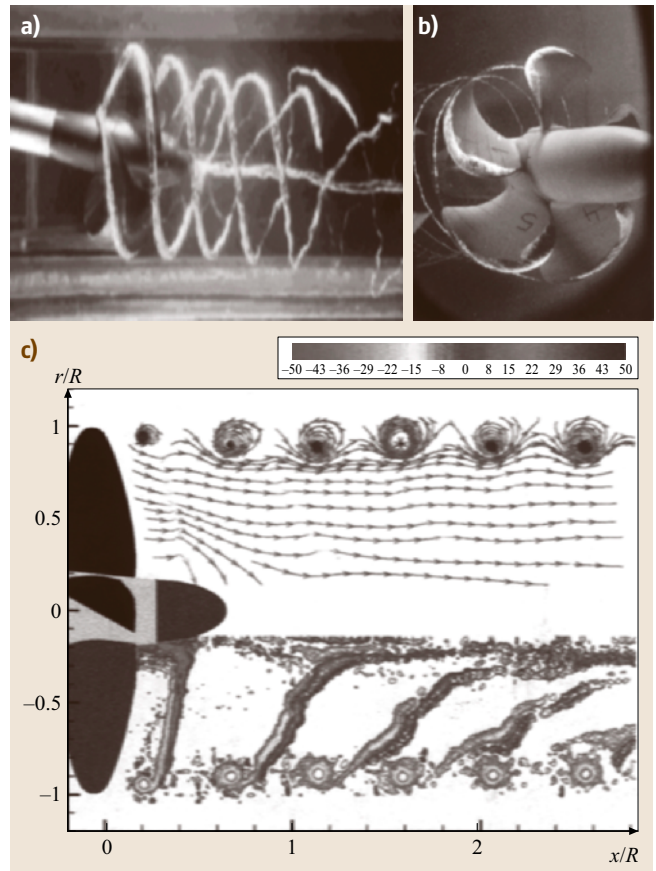


**Fig. 15.6a–c** Propeller cavitation. (a) Example of cavitation in the tip and hub vortices of a propeller (courtesy of H. Kato) (b) Example of tip vortex and surface cavitation on a propeller (courtesy of G. Kuiper) (c) Measurement of the trailing vortex structure behind a propeller using PIV (Courtesy of G. Felice)

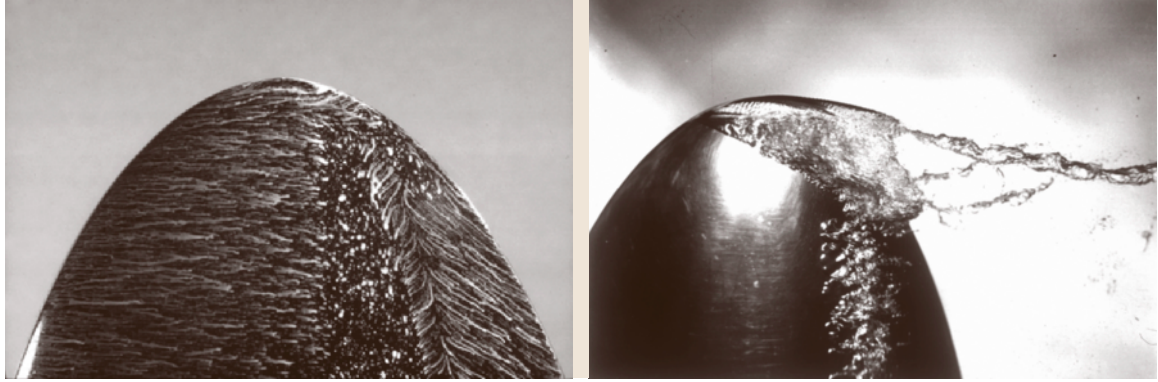


**Fig. 15.7** Cavitation on a NACA 662 – 415 hydrofoil. The photograph on *left* is an oil film visualization made in a wind tunnel. The photo on the *right* is an observation of cavitation on the same foil at the same angle of attack and Reynolds number. Note the existence of both surface cavitation (emanating from a separation bubble at about 60% chord) and tip vortex cavitation

Other definitions of the critical value of the cavitation index exist. Cavitation desinence refers to the conditions necessary to eliminate cavitation. This is denoted by the desinent cavitation number  $\sigma_d$ , which in general is higher than  $\sigma_i$ .

### Inception Dynamics

The simple model of inception described by (15.3) is inadequate [15.14, 15]. This is generally an oversimplification since cavitation inception is governed by the single-phase flow characteristics (including turbulence) and the critical pressure,  $p_c$ . Hence a more general form of the inception cavitation index is given by

$$\sigma_i = -C_{pm} + K \frac{\sqrt{p'^2}}{\frac{1}{2}\rho U^2} - \frac{T}{\frac{1}{2}\rho U^2} \quad (15.4a)$$

where the second and third terms on the right-hand side of (15.4a) incorporate the effects of unsteadiness and bubble dynamics, respectively. The second term, which is proportional to the intensity of pressure fluctuations, is very important in free shear flows and boundary layers adjacent to smooth and roughened walls [15.14, 15, 26]. For example, the value of  $C_{pm}$  in a turbulent jet is roughly equal to zero whereas the second term has values ranging from about 0.2 to 1.0, corresponding to the factor  $K$  being of order 10. The effects of turbulence are found to scale well with a shear stress coefficient defined as

$$C_f = \frac{\tau_0}{\frac{1}{2}\rho U^2} \quad \text{boundary layers} \quad (15.4b)$$

or

$$C_f = \frac{\overline{u_1 u_2}}{\frac{1}{2}\rho U^2} \quad \text{free-shear flows} . \quad (15.4c)$$

$T$  is defined as the tensile strength of the liquid ( $p_v - p_c$ ), which can be an important factor in cavitation testing. It is generally accepted that cavitation inception occurs as a consequence of the rapid or explosive growth of small bubbles or nuclei that have become unstable due to a change in ambient pressure. These nuclei can be either imbedded in the flow or find their origins in small cracks or crevices at the bounding surfaces of the flow.

By considering the static equilibrium of a spherical bubble, the tension that a liquid can sustain before cavitating is found to depend on the size of nuclei in the flow

$$T = \frac{4S}{3R_n} \left[ 3 \left( 1 + \frac{p_0 - p_v}{\frac{2S}{R_n}} \right) \right]^{-\frac{1}{2}} \quad (15.5a)$$

where  $S$  is the surface tension and  $p_0$  is the free-stream pressure when the nucleus radius is  $R_n$ . Note that the tensile strength of the liquid  $T$  should not be confused with the surface tension  $S$ .

Equation (15.5a) implies that the critical pressure for cavitation inception approaches the vapor pressure when there is a sufficient supply of nuclei greater than approximately 100  $\mu\text{m}$ . When the number of sufficiently large nuclei is small, the pressure required for cavitation inception can be *negative*, i. e., the flow is locally in *tension*. Measured nuclei size distributions vary greatly in

various facilities. This leads to significant discrepancies in the measured value of  $\sigma_i$ .

Techniques for the measurement of cavitation nuclei have been developed over the past 30 years. A coherent review of nuclei measurement is given by Billet [15.28]. Many investigators have considered the details of how these nuclei exist. Rood [15.18] provides a review of these efforts. It is only recently that reliable measurements are possible. Most methods of cavitation nuclei measurement are tedious and require sophisticated equipment, as will be outlined subsequently.

Most of the early progress in understanding the details of the inception process has been made through consideration of the dynamic equilibrium of a spherical bubble containing vapor and non-condensable gas. The Rayleigh–Plesset equation describes this equilibrium [15.13]:

$$R\ddot{R} + \frac{3}{2}\dot{R}^2 = \frac{1}{\rho} \left[ p_i - p_\infty(t) - \frac{2S}{R} - 4\mu \frac{\dot{R}}{R} \right], \quad (15.5b)$$

where  $R$  is the time-dependent bubble radius,  $p_i$  is the pressure inside the bubble and  $p_\infty$  is the externally applied pressure. However, as pointed out by Rood, *spherical bubbles passively convected by the mean flow* cannot adequately model real fluid effects on the inception process. Rood goes on to make a very strong argument that inception physics is crucially related to the interaction of bubble dynamics and vortical structures. The problem is complicated by non-spherical bubble deformation and complex modification of the interacting vortical structures. In addition, Joseph [15.29] has pointed out that the cavitation threshold is related to the *maximum* tensile stress in the liquid rather than the *minimum* thermodynamic pressure in the flow. These issues are underscored by the work of Gindroz and Billet [15.30] who were able to demonstrate the effect of the size/number distribution of nuclei on propeller cavitation. Particularly noteworthy for this discussion is their findings that tip vortex cavitation is particularly sensitive to nuclei content (water quality).

#### Influence of Dissolved Gas

Non-condensable gas in solution can also play a role in vaporous cavitation, since the size and number of nuclei in the flow are related to the concentration of dissolved gas. Under certain circumstances, cavitation can also occur when the lowest pressure in the flow is substan-

tially *higher* than the vapor pressure. In this case bubble growth is due to *diffusion* of dissolved gas across the bubble wall. This can occur when nuclei are subjected to pressures below the saturation pressure for a relatively long period of time. Holl [15.31] suggested that *gaseous* cavitation could occur when the flow is locally supersaturated. He suggested an equilibrium theory such that

$$(p_m - p_v)_c \leq p_s = \beta C_g, \quad (15.6)$$

where  $p_s$  is the saturation pressure,  $\beta$  is Henry's constant and  $C_g$  is the concentration of dissolved gas. Henry's constant is a function of the type of gas in solution and the water temperature. As a rule of thumb  $\beta \approx 6700 \text{ Pa/ppm}$  for air, when concentration is expressed in a mole/mole basis. In other words, water is saturated at one atmosphere when the concentration is approximately 15 ppm. Thus, for gaseous cavitation an upper limit on  $\sigma_i$  is given by

$$\sigma_i = -C_{p_m} + \frac{\beta C_g}{\frac{1}{2}\rho U_0^2}. \quad (15.7)$$

The experiments of Holl [15.31] indicate that both gaseous and vaporous cavitation can occur in the same experiment. This is an important consideration when examining the trends of experimental data such as shown in Fig. 15.28. The two types of cavitation are different physical processes and it is sometimes difficult to distinguish between them. Dissolved gas can also influence the measured values of hydrodynamic loads in cavitating flows [15.14, 15].

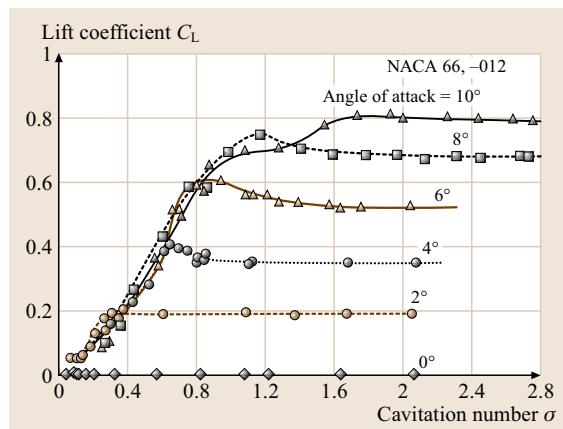
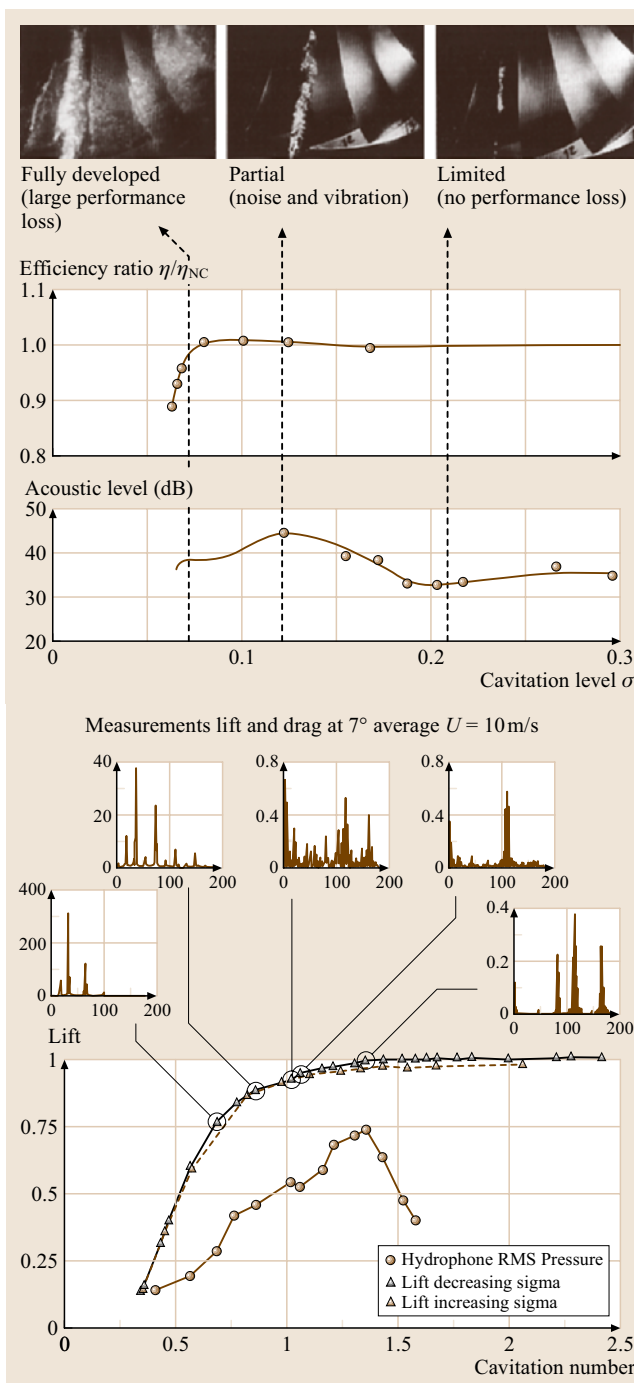


Fig. 15.8 Variation in the lift coefficient of a hydrofoil (after [15.27] with permission by Annual Reviews Inc.)



**Fig. 15.9** (a) Schematic of the relationship of performance breakdown and noise with various stages of cavitation (b) Variation of lift, noise and spectral content of lift oscillations on a NACA 0015 hydrofoil (after [15.32])

### Effects of Cavitation

Once cavitation occurs, a given flow field is significantly modified because the lowest pressure in the flow is typically limited to the vapor pressure. Thus

$$C_{pm} = -\sigma \quad \sigma \leq \sigma_1. \quad (15.8)$$

Since the lift coefficient of a hydrofoil scales with  $-C_{pm}$ , this parameter will decrease with decreasing  $\sigma$ , as shown in Fig. 15.8. The torque coefficient for a turbomachine has a similar trend.

Under some circumstances, inconsistencies are found when analyzing data similar to that shown in Fig. 15.8. This can sometimes be circumvented by measuring the cavity pressure  $p_c$  directly and defining the cavitation number in terms of the cavity pressure  $p_c$ :

$$\sigma \equiv \frac{p_0 - p_c}{\frac{1}{2}\rho U_0^2}. \quad (15.9)$$

The effect of cavitation on lift is directly related to the observed degradation of performance of turbomachinery due to cavitation. This is illustrated in Fig. 15.9. This figure is a composite of turbine model tests (courtesy of Voith Company) and acoustic data from *Deeprise* et al. [15.33]. The turbine head defines the cavitation number in this figure:

$$\sigma_T \equiv \frac{H_{sv}}{H}, \quad (15.10)$$

where  $H_{sv}$  is the net positive suction head [15.34] and  $H$  is the total head under which a given machine is operating.  $\sigma_T$  and  $\sigma$  are qualitatively equivalent. The accompanying photos in the figure clearly illustrate that cavitation occurs at much higher values of  $\sigma_T$  than at the point of performance degradation (as indicated by a reduction in efficiency). This illustrates that  $\sigma_T$  and  $\sigma$  are qualitatively equivalent.

Cavitation can also influence vortex dynamics in subtle ways. For example, *Young and Holl* [15.35] and *Belahadji and Michel* [15.36] found that cavitation strongly influenced the frequency of vortex shedding behind wedges. Because cavitation modifies the forcing frequency due to flow over a body, there is a possibility of unexpected hydroelastic vibration if a closer match between forcing frequency and a structural mode of vibration occurs. An even subtler feature is the *production* of vorticity at the trailing edge of attached cavitation [15.37, 38].

Cavitation is also basically a nonsteady phenomenon. For example, steady flow over a hydrofoil at a value of  $\sigma$  below  $\sigma_1$  results in a highly dynamic form



of sheet cavitation [15.32, 39]. Figure 15.9a illustrates how the dynamics of lift oscillations can change dramatically with  $\sigma$ . Using a simple reentrant jet model, Arndt et al. [15.40] were able to show that for cavity lengths  $l$  less than about 75% of a chord length, an estimate of the frequency of oscillation is given by

$$\frac{fl}{U} = \frac{1}{4}\sqrt{1+\sigma}, \quad (15.11)$$

where  $\sigma$  is defined by the pressure in the cavity (which may not be equal to the vapor pressure [15.14]). Kawanami et al. [15.41] have reviewed cavity oscillation data from several sources, including their own measurements. Equation (15.11) fits their published data very well. Stinebring [15.42] found a similar result for sheet cavitation on a zero caliber ogive. For more developed cavitation, the problem is more complex.

## 15.1.2 Types of Cavitating Flows

### Shear Flows

Turbulent shear flows typically consist of vortical structures that are randomly distributed in space and time. Coherent structures in the flow can play an important role in the cavitation process. For example, Daily and Johnson [15.43] showed that cavitation occurred in a turbulent boundary layer when the wall pressure was greater than the vapor pressure. Cavitation nuclei are entrained into the middle of the boundary layer by large-scale vortical structures where cavitation was observed to occur. Arndt and Ippen [15.44] were able to measure the inception pressure in the cores of these vortical structures by observing the rate of bubble growth during inception with the aid of high-speed cinema photography. The observed growth rate was related to inception pressure utilizing the Rayleigh–Plesset equation. Instantaneous pressure drops of the order of ten times the root-mean-square (RMS) wall pressure were found. Further details can be found in Arndt and George [15.45] and Arndt [15.15].

Figure 15.5 contains an example of cavitation occurring in a turbulent jet. Two cylindrical modes of coherent structure (described by  $\cos m\theta$ ) in the flow are evidenced by cavitation. A smoke-ring-like instability ( $m = 0$ ) is evident close to nozzle, whereas further downstream a helical mode ( $m = 1$ ) is evident. The calculations of Michalke [15.46] indicate that the growth rate of both modes is about equal. Apparently the helical mode dominates downstream. The axial wavelength of this mode is calculated to be about  $1.6D$  where  $D$  is jet diameter, which fits very well with the observations. The

tendency for coherent structures to form in turbulent jets was explored by Chahine and Johnson [15.47]. In developing a patented underwater cleaning device, they found that an underwater jet could be induced to *self-resonate* at a Strouhal number of about 0.3 [15.48]. They showed that the energy content at this natural frequency could be dramatically amplified by creating a feedback mechanism with a resonant chamber. In this manner, the cavitation inception number can be increased by factors greater than two. The jet shear layer organizes into ring vortices that cavitate to form a toroidal cloud of bubbles that is highly erosive. The enhanced cavitation in these structured jets have important applications in deep hole drilling, cleaning, cutting and underwater sound generation. An interesting biological application is used by the *snapping shrimp* that relies on cavitation induced by a high-speed jet to stun his prey [15.49].

Although coherent structures in turbulent jets are important in the cavitation process [15.50], the apparent mechanisms are complex. The inception process appears to occur in micro-vortices that are the *debris* from the pairing process [15.51–53]. Apparently very high negative peaks in pressure are associated with the pairing process. This issue is more complex than previously thought. Gopalan et al. [15.54] found significant differences in the inception mechanism for naturally occurring jets and jets whose nozzle boundary had been tripped. Their experiments revealed that inception in a naturally occurring jet occurred in secondary, axially oriented vortices in the form of inclined cylindrical bubbles at axial distances ( $x/D$ ) of 0.55 with cavitation indices of 2.5. The measured alignment of the cylindrical bubbles was equal to the direction of the measured principal strain. Upon tripping the nozzle boundary layer, inception was observed to occur at  $x/D \approx 2$  as distorted *spherical* bubbles within the primary ring-like structures with an inception index of 1.7. These results indicate that cavitation inception can occur both in the form of distorted spherical bubbles in the primary vortical structures and within secondary axial vortices in the form of cylindrical bubbles. Tripping the boundary layer of the jet apparently suppresses the secondary vortex cavitation.

By observing the growth of injected bubbles [15.55], Ran and Katz [15.50] found that measured negative peaks in pressure are more than a factor of 10 higher than the RMS pressure, similar to the results of Arndt and Ippen [15.44] for a turbulent boundary layer. They also noted that the nuclei distribution in a jet was significantly different from uniform. Nuclei are entrained into low-pressure regions in the flow, enhancing the

probability for cavitation. Similar ideas have been promulgated in the past (e.g., [15.56]), but this study is the first *quantitative* analysis of this factor.

### Attached Cavitation

Various types of cavitation on surfaces can be found in practice, including bubble cavitation, sheet cavitation, cloud cavitation, and various forms of vortex cavitation, depending upon how the low-pressure regions are generated. In spite of considerable research, there are still many features of the problem that have not been properly explored. For example, inception studies are based on fully wetted flow properties, i.e., pressure distribution, turbulence level etc., in the absence of cavitation. Also, classical models of developed cavitation consider only cavitation number as the primary variable. What has not been given adequate attention is a class of partially cavitating flows in which there is an interaction between fluid turbulence and cavitation. For example, vortex generation at the trailing edge of sheet cavitation is a manifestation of the cavitation itself [15.37, 38]. Cavitating microstructures are created that are highly energetic and are responsible for significant levels of noise and erosion. This is an important finding since turbulence is normally attributed to being a factor in the inception process, but cavitation as a mechanism for turbulence generation has been given scant attention.

The details concerning the transition of sheet cavitation to cloud cavitation are still not understood and are beyond the scope of this review [15.38, 57, 58]. It is well known that the modeling of even partial, time-averaged cavities is not simple, due to the inverse character of the flow representation in the vicinity of the cavity and its wake. In addition, partial cavity models cannot explain the breakup of sheet cavitation at the trailing edge into detached cavitation clouds. The process is inherently unsteady even for steady free-stream conditions. Within a certain envelope of cavitation number,  $\sigma$ , and angle of attack,  $\alpha$ , of a lifting surface, the process is also periodic [15.32]. This creates a modulation of the trailing cloud cavitation that is highly erosive and very noisy [15.59]. A typical view of sheet/cloud cavitation on a NACA 0015 hydrofoil is shown in Fig. 15.10a. Figure 15.10b contains a pictorial display of the various types of cavitating flow that were observed on this hydrofoil at various combinations of angle of attack  $\alpha$  and cavitation number  $\sigma$ . Several different cavitating regimes occur depending on the combination of  $\sigma$  and  $\alpha$ . The demarcation between *inception* and  $-C_{pm}$  (computed) varies such that  $\sigma_i$  is always less than  $-C_{pm}$ , as

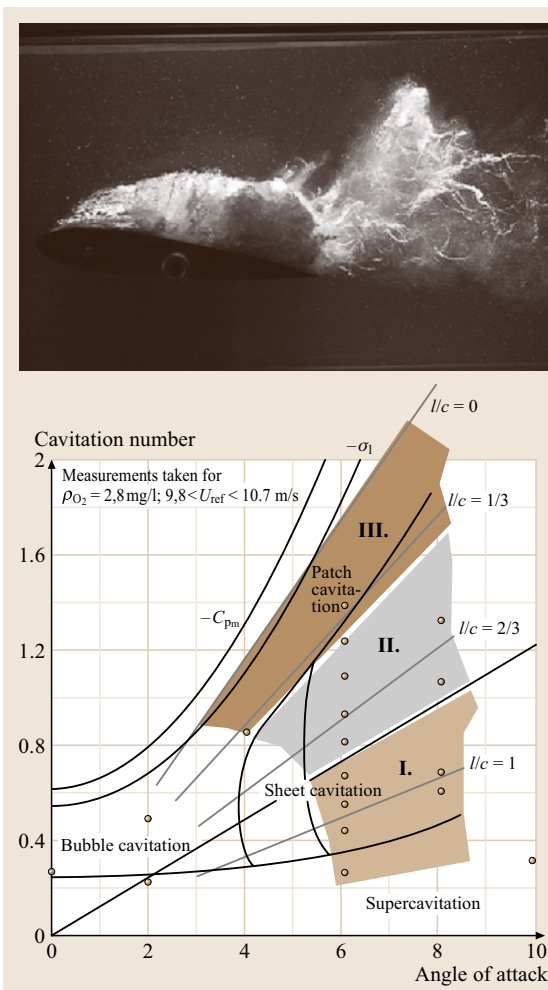


**Fig. 15.10** Sheet/cloud cavitation. The figure on the *right* depicts the various types of dynamics that can occur over a range of  $\sigma$  and  $\alpha$ . Note the lateral extent of the wake

expected. This illustrates that there are some effects of water tensile strength in these data. The solid black lines denote the results of visual inspection. It was noted that sheet cavitation could be subdivided into two regions such that at higher angles of attack ( $\alpha \geq 5^\circ$ ) the flow had a wider dynamic range. At low angle of attack, roughly less than  $4^\circ$ , only bubble cavitation occurred. A sample of bubble cavitation is shown in Fig. 15.4. At intermediate angles of attack and relatively high values of  $\sigma$ , cavitation inception is in the form of patchy cavitation.

Further lowering of the cavitation number results in sheet cavitation that is dominated by relatively low-frequency oscillations,  $fc/U \leq 0.3$ . At higher angles of

attack,  $\alpha \geq 5^\circ$ , a more-complex sequence of events occurs. The flow is still dominated by sheet cavitation. However, the characteristic frequencies of oscillation increase with increasing  $\sigma$ , as will be shown in subsequent plots. Sheet cavitation with large scale break-off of cavitation clouds is also observed.

Cavitation-induced lift oscillations have spectral characteristics that vary considerably over a range of  $1.0 \leq \sigma/2\alpha \leq 8.5$ , where  $\alpha$  is the angle of attack, as shown in Fig. 15.11. The process was found to be highly dynamic. The amplitude of the fluctuations can exceed 100% of the steady-state lift and are associated with the periodic shedding of vortical clouds of bubbles into the flow. Three types of oscillatory behavior are noted [15.39]:

1.  $1.0 \leq \sigma/2\alpha \leq 4.0$ : a strong spectral peak exists at a Strouhal number,  $fc/U = K$ , that is independent of cavitation number.
2.  $4.0 \leq \sigma/2\alpha \leq 6.0$ : a higher-frequency, albeit weaker, spectral peak dominates. The frequency of this peak is almost a linear function of the cavitation number and corresponds to a constant Strouhal number, based on cavity length, of about 0.3.
3.  $6.0 \leq \sigma/2\alpha \leq 8.5$ : bubble/patch cavitation can occur. This induces a distinct, very low-frequency spectral peak.

Frequency data collected from high-speed video of the flow are also shown in Fig. 15.11. These data agree

very well with the lift data. Note that at approximately  $\sigma/2\alpha \approx 4$  there is a sharp transition from one type of frequency trend to the other. The transition that occurs at  $\sigma/2\alpha = 4$  corresponds to a relative cavity length  $l/c$  of about 0.75, as predicted by the linearized analysis of Watanabe et al. [15.60]. Utilizing joint frequency–time analysis (JFTA), Arndt et al. [15.39] found that two mechanisms are at play and that they do not occur simultaneously.

The constant  $K$  is found to vary in the range 0.06–0.30. This raises an important issue concerning cavitation testing. The variation in the volume of cavitation gives rise to compliance in the test section of a water tunnel or other type of test loop (discussed subsequently). Thus the dynamic response of the test facility may play a role [15.61]. This issue is further described in Franc [15.62]. A series of photos showing how cavitation varies over a range of  $\sigma/2\alpha$  is shown in Fig. 15.12.

Of interest to this discussion is the formation of highly vortical structures at the trailing edge of the sheet. Horseshoe vortices are clearly evident in the photos in Fig. 15.12. This phenomenon is well known. Avellan et al. [15.63] and Yamaguchi et al. [15.64] postulated the existence of these structures on the basis of flow instabilities that develop and become unstable on the surface of the sheet [15.65]. More-recent information indicates that baroclinic vortex generation is the primary factor [15.38].

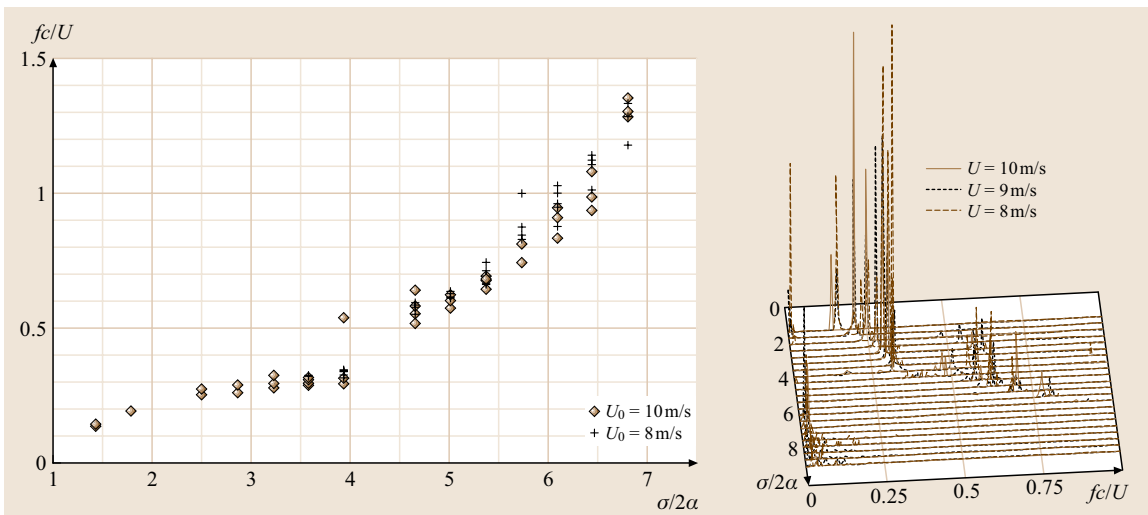


**Fig. 15.11** Frequency of oscillation determined at Obernach with high-speed video (left) and with lift measurements (right) (after [15.39])

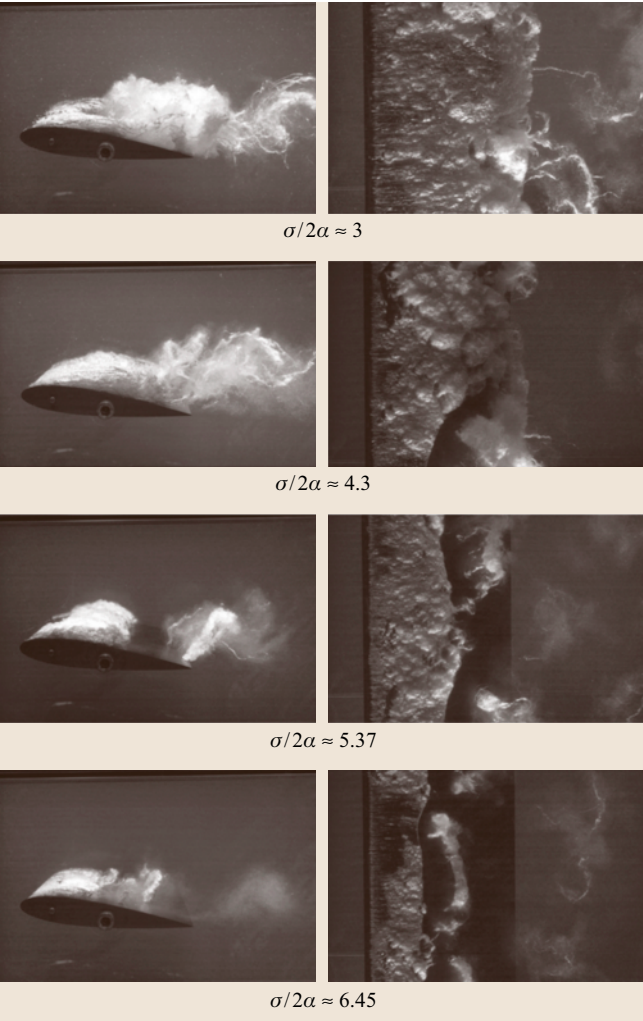


**Fig. 15.12** Variation of sheet cloud cavitation with  $\sigma/2\alpha$ ,  $Re = 1.2 \times 10^6$

**Developed Cavitation**

When a vapor- or gas-filled cavity is very long in comparison to the body dimensions, it is classified as a supercavity. Generally speaking, the shape and dimensions of vapor-filled and ventilated cavities (sustained by air injection) are the same when correlated with the cavitation number based on cavity pressure. The engineering importance of supercavitation relates especially to the design of very high-speed hydrofoil vessels as well as to the design of supercavitating propellers for very high-speed watercraft and supercavitating inducers for rocket pumps and other applications that require the pumping of highly volatile liquids. An example of supercavitation behind a sharp-edged disk is shown in Fig. 15.13. A detailed discussion of supercavitation can be found in Knapp et al. [15.19].

Ventilated cavities require a certain quantity of ventilation gas in order to be maintained. The issues involved are complex. This has been discussed recently by Schauer [15.67] and Wosnik et al. [15.68]. Figure 15.14 illustrates the relationship between air demand, cavitation number and cavity dimensions.

**15.1.3 Cavitation Damage**

The physics of cavitation damage is a complex problem. At the heart of the problem is the impulsive pressures created by collapsing bubbles [15.6]. Recent numerical techniques permit detailed examination of the collapse of individual bubbles [15.17, 69]. This work has been complemented by a wide variety of experimental stud-

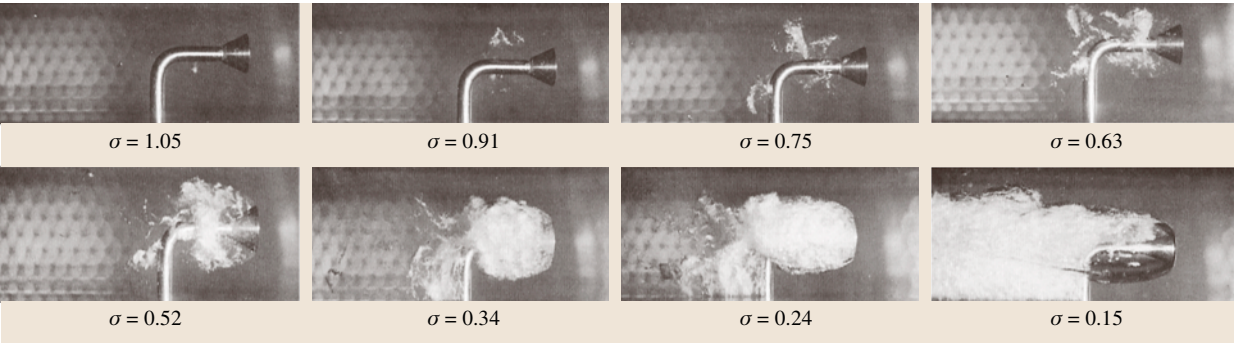


**Fig. 15.13** Sequence of photos illustrating the transition from shear flow cavitation in the wake of a sharp-edged disk to fully developed supercavitation. Flow is from right to left (after [15.66])



ies [15.70–72]. All of these studies indicate that the final stages of collapse result in the formation of a micro-jet that can be highly erosive (Fig. 15.15). The collapse pressure is estimated to be greater than 1500 atmospheres.

Very little is known about the correlation between cavitation damage and the properties of a given flow field. However, it is important to bear in mind that cavitation erosion will scale with a high power of velocity at a given cavitation number and that cavitation erosion does not necessarily increase with a decrease in the cavitation index [15.73]. It has also been observed that the cavitation pitting rate is measurably reduced with an increased concentration of gas [15.73]. An important factor is that the pitting rate scales with a very high power of velocity (typically in the neighborhood of six). Since the velocity in turbomachinery passages is proportional to the square root of the head, this also implies that the magnitude of the erosion problem is more severe in high-head machinery.

Thiruvengadam [15.74] has analyzed a great deal of erosion data and has concluded that, for engineering purposes, the erosive intensity of a given flow field can be quantified in terms of depth of penetration per unit time  $\dot{y}$  and the strength  $S_e$  of the material being eroded,

$$I = \dot{y} S_e. \quad (15.12)$$

The intensity  $I$  is a function of a given flow field. Many different forms of  $S_e$  have been tried. The most used value appears to be ultimate strength, which is basically a weighted value of the area under a stress-strain curve [15.75]. Although various materials have different rates of weight loss when subjected to the same cavitating flow, a normalized erosion rate versus time characteristic is often similar for a wide range of materials. Hence, a simplified theory allows for a rapid determination of  $I$  for a given flow by measuring  $\dot{y}$  for a soft material in the laboratory. Service life for a harder material can then be predicted from the ratio of the strengths of the hard and soft materials.

Although the basic physics of the damage process in turbomachinery is complex, the essential features can be simulated by experiments with partially cavitating hydrofoils in a water tunnel [15.63, 76–80]. These studies indicate that maximum erosion occurs at the trailing edge of a cavity. The cavitation cloud at the trailing edge contains complex vortical structures that are highly erosive.

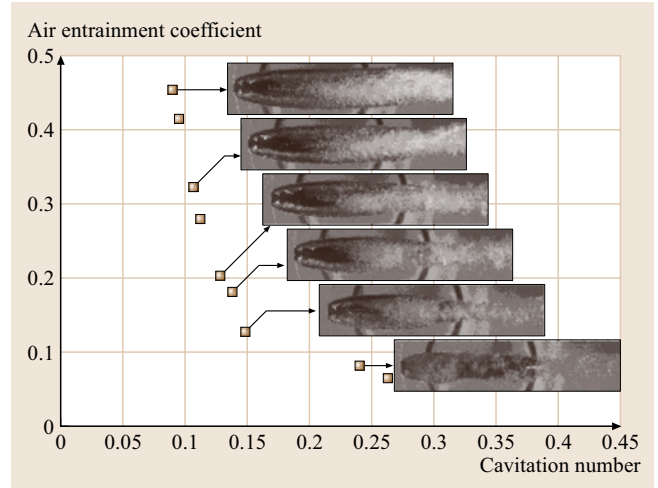


Fig. 15.14 Air entrainment coefficient  $Q/Ud^2$  versus cavitation number for a ventilated cavity (after [15.67])

### Partial Cavitation and its Relation to Erosion

In practical problems, the collective collapse of a cloud of bubbles is an important mechanism. Hansson and Mørch [15.81] suggested an energy-transfer model of concerted collapse of clusters of cavities. Because of mathematical difficulties this problem has not been studied in detail until recently [15.82, 83]. Earlier work [15.84] had already indicated the damage potential of a collapsing cloud of bubbles. Recent work supports this contention [15.85]. Very little is known about the correlation between cavitation damage and the properties of a given flow field. However, it is important to bear in mind that cavitation erosion will scale with

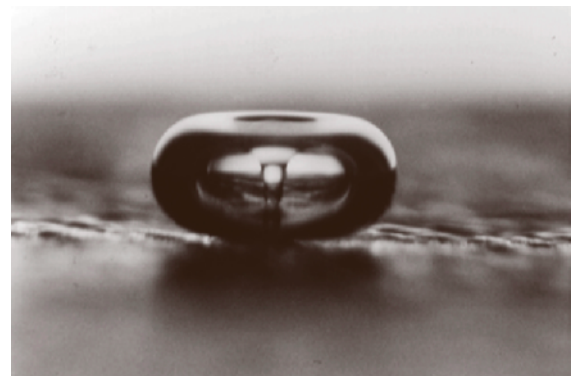
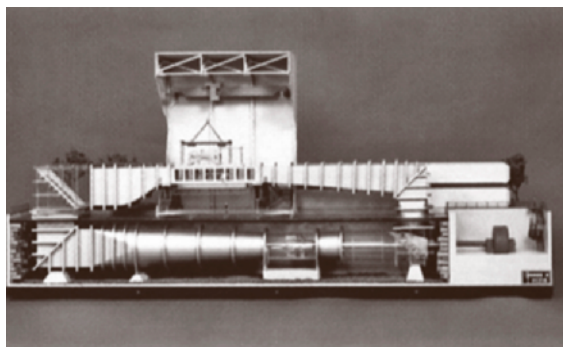


Fig. 15.15 Asymmetric bubble collapse near a surface (note the jet located in the bubble center). The bubble is approximately 0.2 cm in diameter

a high power of velocity at a given cavitation number and that cavitation erosion does not necessarily increase with a decrease in the cavitation index [15.73]. It has also been observed that the cavitation pitting rate is measurably reduced with a break-up of sheet cavitation at the trailing edge into detached cavitation clouds. The process is inherently unsteady, even for steady free-stream conditions. This creates a modulation of the trailing cloud cavitation that is highly erosive [15.40, 77, 78]. These details cannot be modeled with current numerical codes.



**Fig. 15.16** Model of the US Navy large cavitation channel. This facility is approximately 10 storeys high and has a test section that is  $3\text{ m} \times 3\text{ m} \times 16\text{ m}$ . The maximum flow velocity is approximately  $16\text{ m/s}$ . The recirculating pump is powered by a 14 000 hp motor

### 15.1.4 Facilities

Most cavitation observations and measurements are made in the laboratory. The exception to this is the recent development of cavitation monitoring techniques for hydroturbines [15.86]. Typical laboratory facilities include

1. Water tunnels;
2. Depressurized flumes;
3. Depressurized towing tanks;
4. Pump and turbine test loops;
5. Cavitation erosion test apparatus.

#### Water Tunnels

Water tunnels have been used for a wide variety of cavitation testing and research for about a century. The first known use of a water tunnel for cavitation research is due to *Parsons* in 1895 [15.20]. Since that time these facilities have grown in size and complexity. As of this writing (2004), the largest facility of its kind is the US Navy large cavitation channel [15.87,88]. A view of this facility is shown in Fig. 15.16. Much smaller facilities are more common in research laboratories, especially at universities. Examples of some smaller facilities are shown in Figs. 15.17, 18.

Important features necessary for cavitation tests include accurate, stable, independent control of pressure and velocity, measurement equipment for velocity, pressure, temperature, dissolved gas content and nuclei content and control, and photographic and video equipment. Because of the unsteady nature of cavitation and the extremely rapid physical processes that occur during bubble collapse and erosion, many laboratories are equipped with highly specialized high-speed video and photographic cameras that are capable of very high frame rates. Unsteady lift and drag measurements necessitate specially designed force balances [15.39]. A typical test section set up is shown in Fig. 15.19. Figure 15.20 illustrates the special monitoring equipment that is necessary for cavitation research.

#### Depressurized Flumes and Towing Tanks

A variety of facilities have been developed for studying cavitation phenomena in free surface flows. These include water tunnels with a variable pressure free surface test section, variable pressure towing tanks, and specialized variable pressure tanks for hydraulic model tests. It is important to note that cavitation testing in free surface flows can be especially demanding in terms of pressure

- |  |                           |  |
|--|---------------------------|--|
| 1. Test section, $1270 \times 190\text{ SQ}$ | 6. Axial flow pump, 150HP | 11. Contraction and partial shape transition |
| 2. Test section dome                         | 7. Diffuser screens       | 12. Nozzle                                   |
| 3. Skimmer                                   | 8. Gas collector dome     | 13. Booster pump                             |
| 4. $7^\circ$ diffuser                        | 9. Gas separator, 2134D   |  |
| 5. Guide vane elbow                          | 10. Honeycomb             |  |

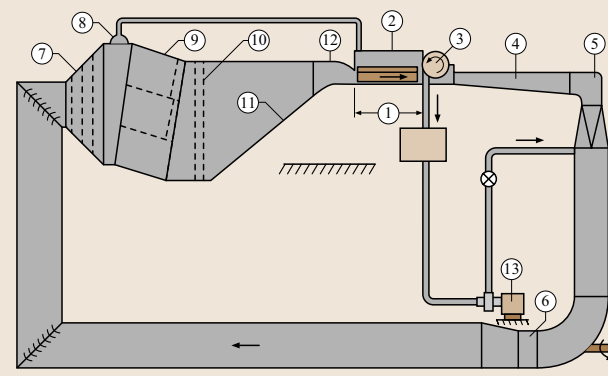


**Fig. 15.17** The SAFL high-speed water tunnel at the University of Minnesota. The test section is  $0.19\text{ m} \times 0.19\text{ m} \times 1\text{ m}$ . The maximum flow velocity is  $30\text{ m/s}$

control. Simultaneous modeling of cavitation number and Froude number requires scaling of the free surface pressure:

$$\frac{(p_0 - p_v)_m}{(p_0 - p_v)_p} = \frac{l_m}{l_p} \quad (15.13)$$

In other words tests with a 1/25 model would have to be carried out at approximately (1/25)-th of an atmosphere.

The Vacutank at the Marin Institute, Netherlands (formerly NSMB) is a unique facility that was specially designed for ship propeller research using large ship models with simultaneous identity of Froude number and cavitation number. It differs from a standard towing tank because of its capability to maintain the pressure above the free surface in the range 40–1000 millibars. Broadly speaking the pressure must be reduced in proportion to the model scale; 40 millibars is the approximate pressure necessary for testing with a 1:30 model. The basin is 240 m in length, 18 m wide, and 8 m deep. A sketch of the facility is shown in Fig. 15.21. Ship models as large as 13 m in length can be studied in this facility, which has been recently upgraded (2003).

### Pump and Turbine Test Loops

Pump and turbine test loops are similar in concept to water tunnels. Model testing is an important element in the design and development phases of turbine manufacture. Manufacturers own most of the laboratories that are equipped with model turbine test stands. However, there are independent laboratories available where relative performance evaluations between competing manufacturers can be carried out. An example is shown in Fig. 15.22, which is the Independent Turbine Test Facility at the Saint Anthony Falls Laboratory.

All test loops perform basically the same function. A model turbine is driven by high-pressure water from a head tank and discharges into a tail tank. The flow is recirculated by a pump, usually positioned well below the elevation of the model to ensure cavitation-free performance of the pump while performing cavitation testing with the turbine model. One important advantage of a recirculating turbine test loop is that cavitation testing can be done over a wide range of cavitation indices at constant head and flow, which is difficult, if not impossible, to accomplish in the field.

### Cavitation Erosion Test Facilities

In many cases the service life of equipment and hydraulic structures subject to cavitation erosion can range from months to years. Because of the relatively lengthy

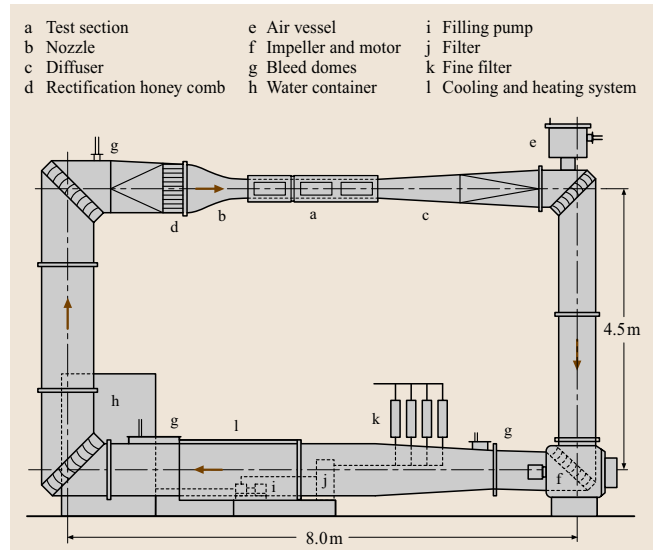


**Fig. 15.18** The 30 cm-square water tunnel at the Versuchsanstalt für Wasserbau (VAO) in Oberrach, Germany. The maximum flow velocity is about 16 m/s

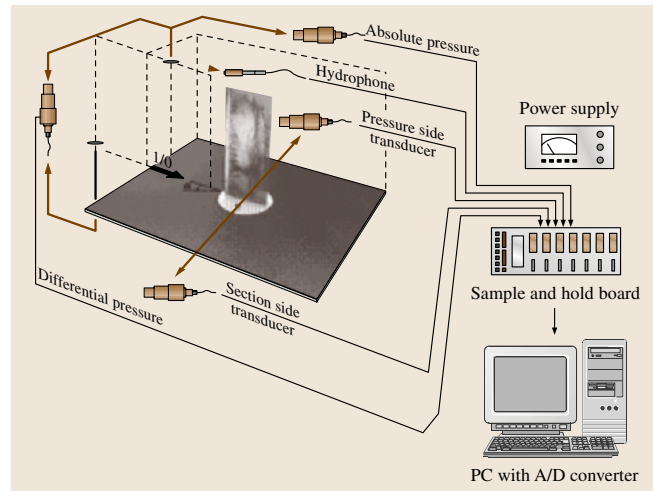


**Fig. 15.19** Typical instrumentation setup for investigation of hydrofoil cavitation in the SAFL water tunnel

periods required to observe measurable erosion in the field, many different techniques have been developed in the laboratory to achieve significant time compression. The time compression factor achieved in accelerated erosion tests is as high as  $10^5$  [15.89]. Many of the devices used have little relationship to actual field conditions. For this reason they have typically been used for screening tests of different types of materials. Recent

research is aimed at relating screening tests to predictions of service life in various applications [15.40]. The most commonly used device is the American Society for Testing and Materials (ASTM) vibratory apparatus. An oscillating horn produces a periodic pressure field that induces the periodic growth and collapse of a cloud of cavitation bubbles. A sample placed at the tip of the horn or immediately below it is easily eroded. The standard frequency of operation is 20 KHz, which produces a very high erosion rate due to the rapid recycling of the cavitation process.

As already mentioned new methods are being developed for measuring the erosion rate in the field. Usually the erosion rate is inferred from the measurement of noise or vibration. Measuring the impact pressure of the microscopic pressure jets caused by bubble collapse is a difficult task. Since the impact area is on the order of  $\mu\text{m}^2$  and the duration of the impact is on the order of  $\mu\text{s}$ , advanced methods are needed to measure the impact. Arndt et al. [15.59] used a piezoelectric polymer, polyvinylidene fluoride (PVDF) to measure pressure impulses on a cavitating hydrofoil. Soyama and Kumano [15.90] used PVDF film to measure the impact

energy of bubble collapse in a cavitating jet facility and estimated the threshold at which erosion will occur.

Quantifying cavitation erosion is a nontrivial endeavor as well. Perhaps the most commonly investigated parameters are pitting rate and mean depth of erosion penetration rate (MDPR), which is the number of pits caused by cavitation per unit time and the mean depth of erosion per unit time respectively. Determining the number of pits and average depth requires a microscope and well-positioned lighting since pit diameters are generally in the range 10–150  $\mu\text{m}$  range (soft aluminum [15.19, 91]). In addition, other parameters include volume loss rate, maximum penetration depth, incubation period, and time until maximum damage rate. The last two give an indication of time before erosion actually occurs. In some cases, cavitation initially acts to harden the material, similar to shot peening. For this reason, an incubation period is often of interest, where the material is actually hardened. In addition to measuring cavitation erosion, the cavitating jet method is being investigated as a method of surface hardening materials.

As mentioned, it is necessary in an experimental investigation to compress the erosion time to a point where

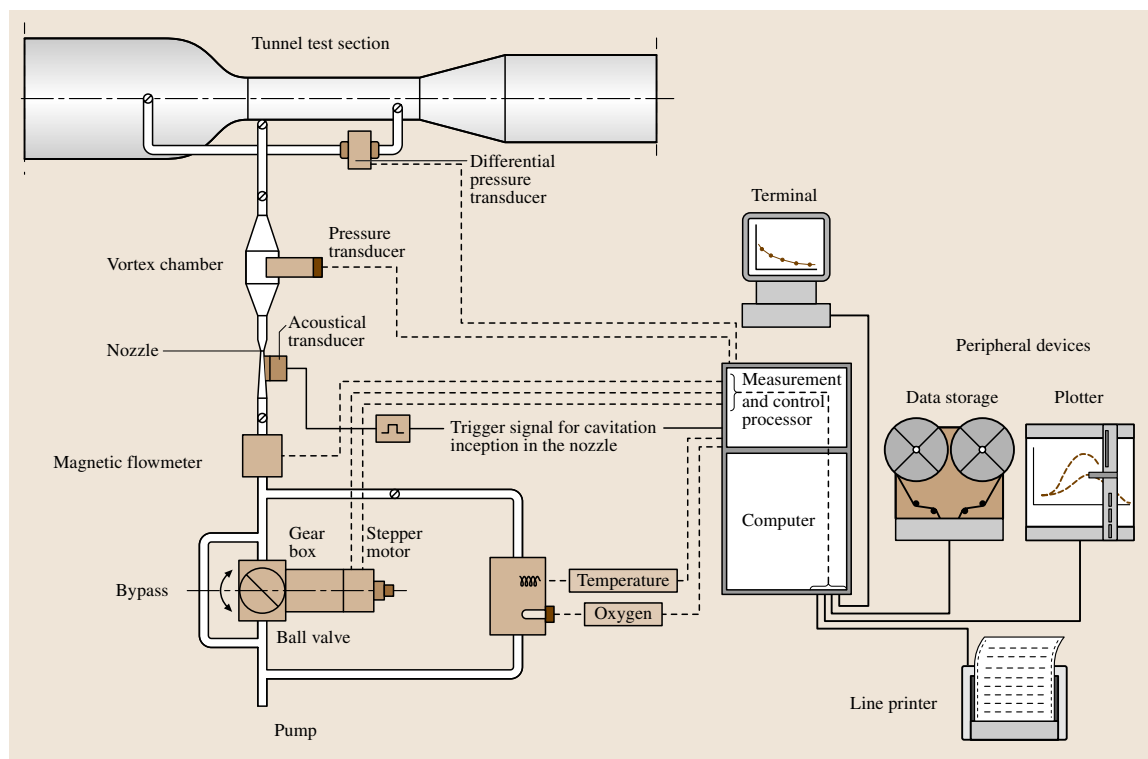


**Fig. 15.20** Instrumentation for monitoring water quality at the water tunnel in Obernach, Germany



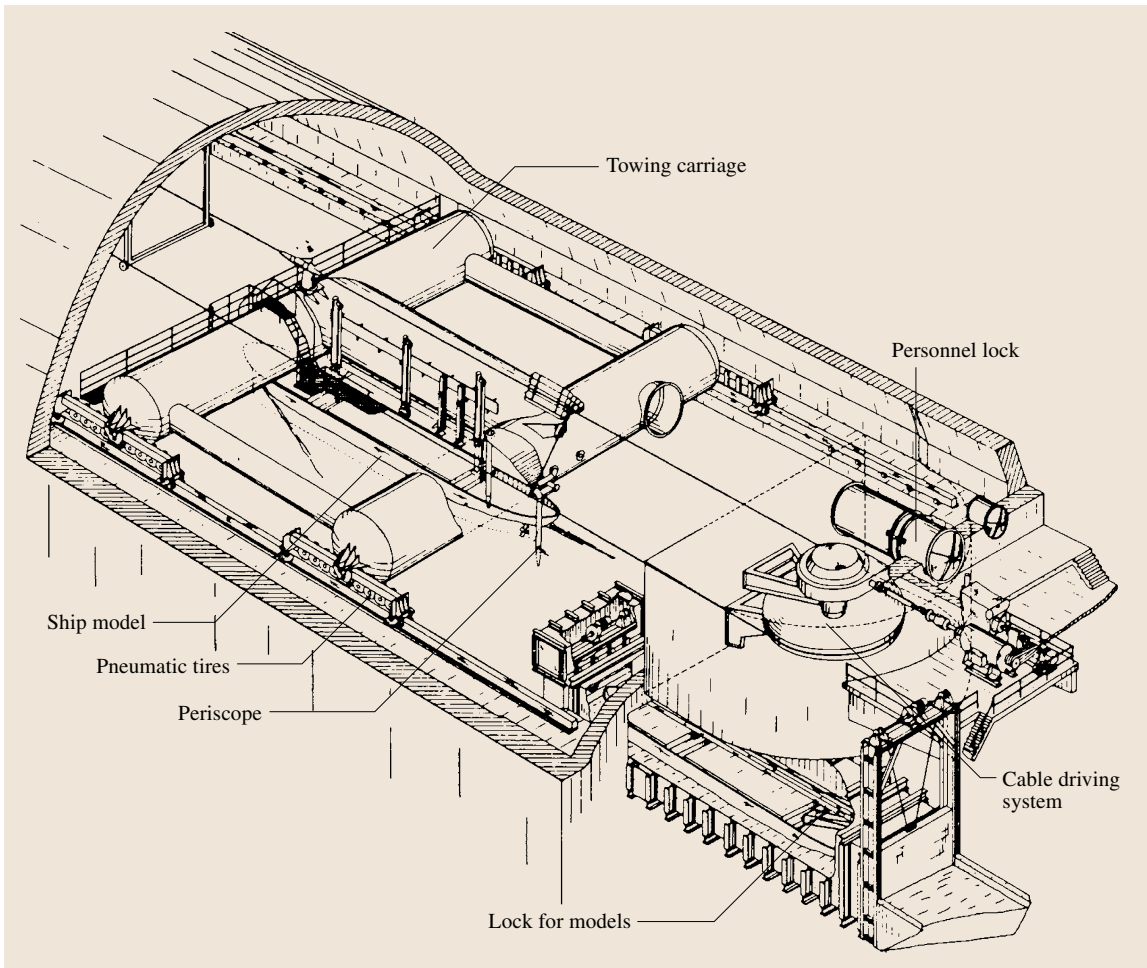


**Fig. 15.21** Depressurized towing tank at MARIN

meaningful information can be acquired in a reasonable amount of time. While significantly increasing the erosion rate on a given material, these methods provide only a qualitative comparison of erosion rates, rather than a means for estimating erosion rate. The five most common methods are discussed: the vibratory method, the rotating disk method, the Venturi method, cavitating jets, and the liquid impingement method.

### Venturi Method

The Venturi method has the least amount of time compression, but also most closely resembles flow conditions in practical applications. While a standard device does not exist, most Venturi erosion systems are a variation of the same principle. A test body is placed slightly

downstream of the throat of a Venturi nozzle or in the test section of a high-speed water tunnel. The test body can either be a portion of the test section wall, or located in the center of the flow. The constriction of the throat can produce liquid velocities upwards of 100 m/s, causing rapid erosion.

Numerous researchers [15.73,92,93] have found that pitting rate scales with velocity to the  $\sim 6$ th power, despite significant variation in test section geometries. As a result, maintaining the same velocity from actual conditions to test specimen should result in identical erosion rates. Furthermore, a 25% increase in velocity will increase the pitting rate by nearly a factor of four. This trend will not increase indefinitely, however. Belahadji et al. [15.93] argue that the power should tend towards

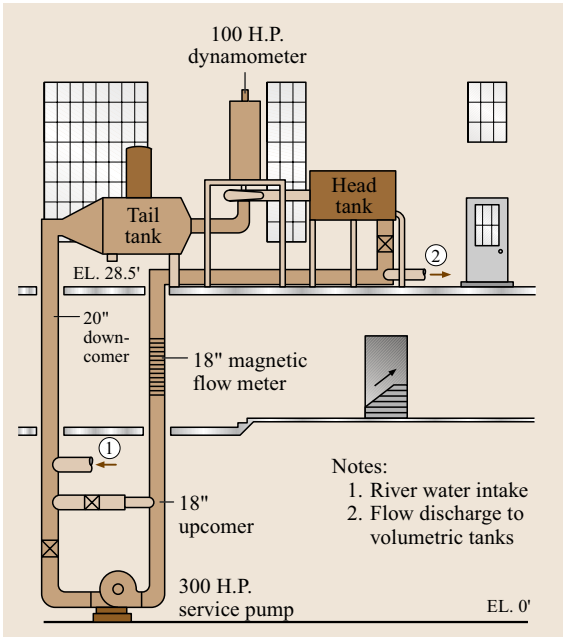


**Fig. 15.22** Turbine test stand at the Saint Anthony Falls Laboratory (after [15.75])

unity as velocity increases and showed that the scaling does indeed break down at higher velocities.

In practice, a direct correlation between Venturi tests and actual applications is not always possible. These facilities are very expensive to build and operate. In addition, despite the power relation, the flow velocities necessary to perform tests that are analogous to the situation in the field in a reasonable amount of time are often still too high.

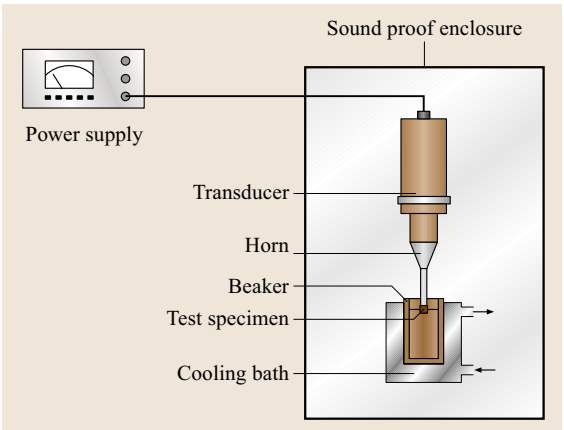


**Fig. 15.23** ASTM G-32 standard vibratory apparatus

### Vibratory Method

As mentioned previously, the vibratory method is perhaps the most common method used to carry out erosion studies. The vibratory method utilizes a rapidly oscillating disk to generate cavitation. The oscillation can be induced by amplified high-frequency sound waves or a magnetostriction device. In either case, a specimen is made to oscillate at a frequency on the order of 10 kHz with an amplitude less than 100  $\mu\text{m}$  in the desired liquid, creating cavitation and rapid erosion. The surface being examined can either be the oscillating disk (moving specimen), or a sample placed directly below the oscillating disk (stationary specimen). This method provides a low-cost alternative to the Venturi method. In addition, cavitation in various liquids for various materials can be studied with relative ease, since the specimens are naturally small and easy to manufacture, and the volume of liquid needed is much smaller. This method has been used to study cavitation in mercury and high-temperature liquid metals, a capability unique to this method.

The vibratory method is capable of compressing the erosion time anywhere from 300 to 700 times for steel [15.89]. Unfortunately, a correlation of erosion time between the vibratory method and field conditions does not exist. As a result, the method only allows for qualitative comparison. An extensive discussion on the vibratory method along with results for numerous metals is given by Knapp et al. [15.19].

### Rotating Disk Method

The rotating disk employs a perforated, thin, rapidly rotating disk submerged in a fluid to create cavitation. Small holes are made in desired positions on the disk and inserts are placed either flush to the disk at the same radius or protruding perpendicular to the disk face. Under high rotational speeds, cavitation bubbles are created by the holes and collapse on the inserts. The collapse of the cavitation bubbles results in erosion. The advantage of the rotating device is that it more closely mimics the flow patterns seen in rotating machinery, such as pump impellers, hydroturbines, and the like. The disadvantages, however, include a more complex flow field than the other methods.

### Cavitating Jet Method

The cavitating jet method causes erosion by introducing a high-pressure jet into a low-pressure stagnation chamber where a specimen is placed at some distance from the nozzle. Vortex cavitation forms in the high-shear regions on either side of the jet core. As the jet propagates downstream and expands, periodic

cloud cavities are observed [15.94]. The cavitating jet has some advantages over other methods. With relative ease, the upstream and downstream pressures of the jet can be varied to simulate a wide variety of cavitating conditions.

### Impinging Jet Method

While the cause of erosion in the impinging jet method is not cavitation, the method is worthy of note. A liquid jet is made to impact the surface of a rotating wheel. Similar to the rotating disk, inserts are placed in the disk such that it crosses the path of the liquid jet(s). The disk is made to rotate very rapidly and the impact between the test specimen and a liquid jet of moderate velocity causes erosion similar to cavitation. This situation closely resembles erosion that occurs in Pelton-wheel-type hydroturbines. This method is capable of the most rapid erosion rates and can compress erosion time by as much as 9400 times [15.89].

Table 15.1 gives a comparison of the five methods as taken from results of the international cavitation erosion test (ICET). It is clear that the liquid jet method yields the highest erosion rates, followed by the rotating disk method. The vibratory and tunnel methods have

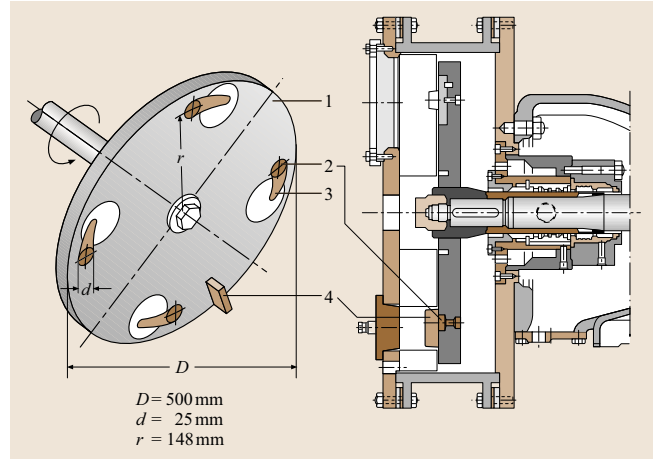


**Fig. 15.24** Rotating disk device used by KSB, 1 – rotating disk, 2 – cavitation generating holes, 3 – cavitating wake, 4 – stationary specimen (KSB Aktiengesellschaft, Frankental, Germany, [http://www.imp.gda.pl/icet/KSB/KSB\\_rd.html](http://www.imp.gda.pl/icet/KSB/KSB_rd.html))

similar erosion rates for most metals, and the cavitating jet has the lowest erosion rate. It should be noted that erosion rates are highly dependent on flow conditions

**Table 15.1** Maximum erosion rates for various methods and various test metals (a: vibration amplitude, s: standoff distance) [Taken from the ICET results (<http://www.imp.gda.pl/icet>)]. ARMCO: American Rolling Mill Company

	Parameters	MDPR <sub>max</sub> (μm/min)				
		Cr–Ni steel	C steel	ARMCO Fe	Brass	Al alloy
Cavitation tunnel	$P_1 = 1030 \text{ kPa}$ , $u = 30 \text{ m/s}$	0.05	0.06	0.15	0.25	2.35
	$P_1 = 103 \text{ kPa}$ , $u = 14 \text{ m/s}$	0.15	0.32	0.33	0.74	2.01
Vibratory rig	(stationary) $a = 0.05 \text{ mm}$ $s = 0.35 \text{ mm}$	0.19	0.17	0.56	0.56	6.90
	(moving) $a = 0.040 \text{ mm}$	0.45	0.39	1.83	1.42	6.10
Rotating disk	$P = 255 \text{ kPa}$ , $u = 42.5 \text{ m/s}$	> 0.44	> 0.43	0.77	3.10	18.20
Cavitating jet	$P_1 = 19 \text{ MPa}$ $P_2 = 0.1 \text{ MPa}$ , $s = 18 \text{ mm}$	0.03	0.14	0.09	0.17	1.38
Liquid jet	Jet vel.=6.75 m/s, sp. vel.=80 m/s	1.32	> 2.60	> 2.60	11.10	33.75

**Table 15.2** Compression times of MDPR for aluminum and steel (From [15.89])

Experimental set up		MDPR (μm/h)		Compression time	
Method	Parameters	Al	St. G-X5	Al	St. G-X5
Venturi	60 m/s	4.35	0.0134	1.0	1.0
	80 m/s	24	0.072	5.5	5.4
	110 m/s	160	0.49	37	37
Magnetostriction oscillator	Stationary specimen ( $s = 1.2 \text{ mm}$ )	–	2.51	–	187
	Moving specimen ( $a = 0.010 \text{ mm}$ )	537	4.24	123	316
	Moving specimen (0.015 mm)	847	6.77	195	505
	Moving specimen (0.025 mm)	1528	11.3	351	843
Jet cavitation	$P_1 = 250 \text{ bar}$ , $P_2 = 1.3 \text{ bar}$ , $s = 21 \text{ mm}$	1166	9.9	268	739
Drop impingement	jet vel. = 410 m/s $d = 1.2 \text{ mm}$	50 400	1260	11 586	94 030

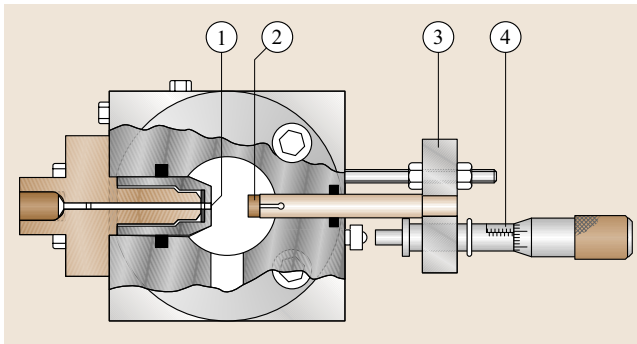


**Fig. 15.25** ASTM G-134 standard cavitating jet apparatus, 1 – nozzle, 2 – specimen, 3 – specimen holder, 4 – micrometer head. (KSB, Frankental, Germany, [http://www.imp.gda.pl/icet/KSB/KSB\\_rd.html](http://www.imp.gda.pl/icet/KSB/KSB_rd.html))

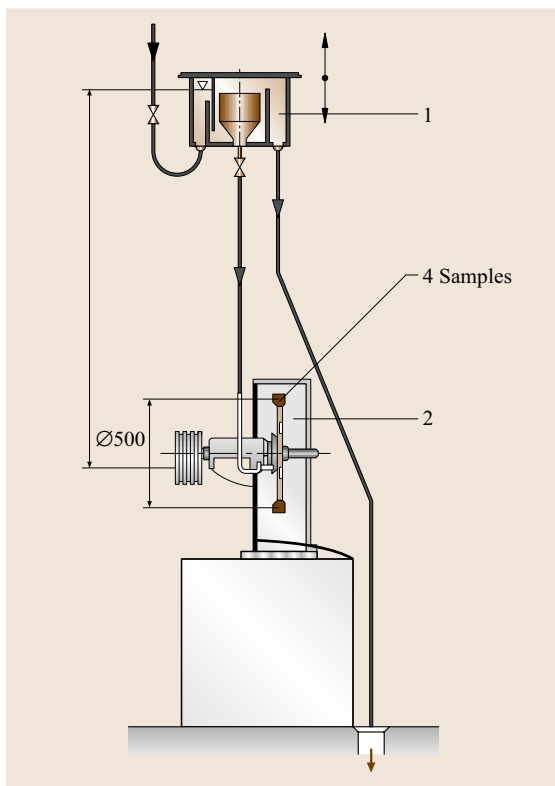


**Fig. 15.26** Impinging jet device used by SIGMA, 1 – tank with controlled water level, 2 – test chamber. (SIGMA Research Institute Olomouc, Czechoslovakia, [http://www.imp.gda.pl/icet/SIGMA/Sigma\\_li.html](http://www.imp.gda.pl/icet/SIGMA/Sigma_li.html))

and it is difficult to generate analogous conditions between methods. Due in part to a lack of standards and

difficulties in determining and correlating actual field conditions to test conditions, it has been argued that erosion tests should be performed on the actual field models [15.95].

Table 15.2 gives the erosion rates and compression time for various methods taken from *Durrer* [15.89]. Similar trends are noted in Table 15.1, except the compression time is significantly larger than seen in Table 15.2. It should also be noted that, while in both cases aluminum experiences the most severe erosion rates, the compression time between methods is the smallest. This further complicates attempts to scale erosion tests to the full-scale model where, in addition to the flow conditions, the difference in material plays a crucial role.

In general, however, the erosion rate decreases with increasing material strength. Various researches have investigated various scaling relations. *Syamala Rao et al.* [15.96] studied various methods and attempted to scale volume loss rate using different material properties. They found that results scaled best when scaling volume loss rate with the product of ultimate resilience and Brinell hardness. Figure 15.27 contains a plot of relative erosion rate using the concept developed by *Thiruvengadam* [15.74]. In this plot the erosive intensity expressed in terms of depth of penetration per unit time  $\dot{y}$  is plotted versus time. Both the abscissa and the ordinate are normalized with respect to  $\dot{y}_{\max}$  and the time at which it occurs  $t_{\max}$ . In this way a variety of different materials are shown to have the same relative time history of erosion. *Thiruvengadam* argues that erosion tests with a relatively soft material can be scaled up to prototype conditions with a harder material.

The relative erosion concept suggests another method for investigating erosion on a model or full scale is using soft metal inserts. If the proper scaling rates between metals can be determined, then softer metal inserted in cavitating equipment can be used to investigate erosion. This method requires drilling a hole in the model at the location of interest. Metal inserts are placed flush with the model surface, and cavitation tests are performed. Soft metal inserts placed in various locations on a turbine blade, for instance, give an indication of the relative erosion rate at a given location. With this knowledge, problematic areas can be treated to extend the life of the blade.

One of the simplest methods for erosion tests on full-scale equipment or scaled models can be done with a paint coating. Researchers found that a mixture of black stencil ink and thinner is capable of indicating areas where significant erosion will occur on a ship propeller in less than an hour. The international towing tank



conference (ITTC) committee proposed technique using a soft surface made of stencil ink and ethyl alcohol for cavitation erosion tests. *Kadoi and Sasajima* [15.97] followed this procedure with some modifications to investigate erosion damage at different velocities on a model ship propeller. Recent tests at SAFL indicate that Dykem *Steel Blue* layout fluid also works well for qualitative visualization of cavitation erosion. Surface preparation, paint concentration, application method (brush versus spray) and drying time critically affect the paint erosion result, and need to be determined on a case-by-case basis.

While much knowledge has been gained concerning the cause and behavior of erosion due to cavitation, an accurate scaling procedure from test to field conditions is still not available. Results suggest that, in addition to flow and liquid characteristics, the material properties of the surface in question also play an important role. An acceptable scaling relation and theoretical explanation of cavitation erosion is a worthy endeavor and sorely needed.

### 15.1.5 Water Quality Measurements

Numerous studies highlight the importance of water quality monitoring when investigating cavitation. One well-known example is the ITTC test body that was tested at various international facilities. Cavitation inception was measured versus flow velocity. The results showed a large variation in measured inception value (Fig. 15.28). Differences in water quality are partly to blame for the huge discrepancy. Cavitation occurs when the pressure in a flow goes below a critical value, causing microscopic nuclei to expand explosively. A flow containing a large supply of nuclei will necessarily cavitate more readily than a flow with relatively few nuclei. An indication of the ability of a liquid to resist cavitation is the tensile strength. In theory, water without nuclei can withstand tensile stresses of approximately  $10^4$  atmospheres before cavitation occurs [15.99]. In practice, great care is needed even to produce water capable of withstanding more than two atmospheres.

Various factors influence the water quality of a given liquid. The presence of particulate matter in a liquid acts to decrease the surface tension of a bubble. *Church* [15.100] found that the surface tension of *clean bubbles* void of particle impurities on the liquid–gas interface is more than twice the value of *dirty bubbles* containing chemical and particle impurities. *Marschall et al.* [15.101] studied the effects of particle size on wa-

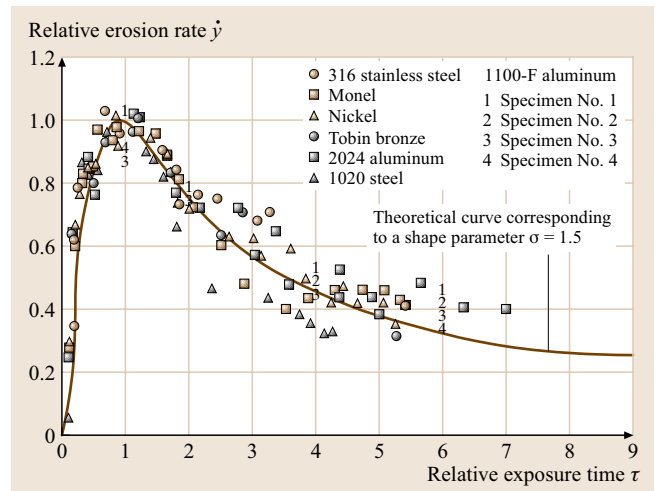


Fig. 15.27 Relative erosion rate versus dimensionless time for various metals

ter quality in degassed tap water and found that particle size, shape, and hydrophobic/hydrophilic characteristics influence the tensile strength. *Ma* [15.102] observed that tensile strength increased when water is stored under high pressure for a prolonged period of time. The high pressure, in addition to decreasing the mean nuclei size, causes gas bubbles to dissolve, decreases the number of available nuclei.

Numerous researchers have studied the effects of water quality on cavitation behavior. It is well known that

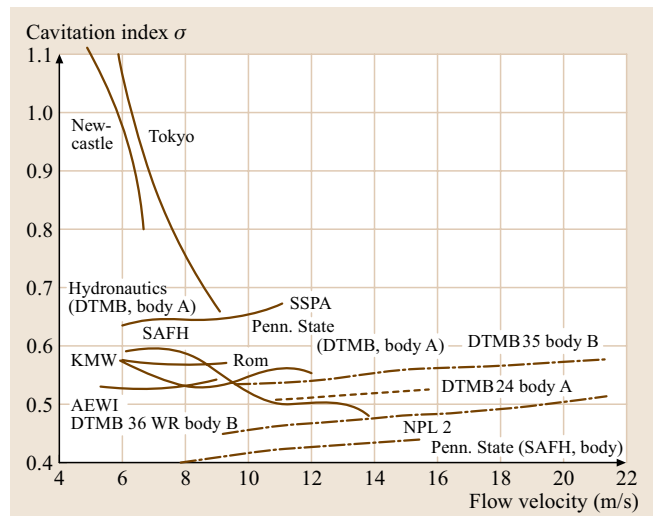


Fig. 15.28 Inception values for the same body measured at different water tunnels [15.98]

water quality effects influence the behavior of cavitation. *Van der Meulen* [15.103] studied water quality effects on inception and desinent cavitation on hemispherical-nosed bodies. In an extensive review of the subject, *Keller* [15.104] noted that not only is the value of the inception index affected, but water quality has an influence on the appearance of cavitation as well. *Kawakami et al.* [15.105] found that water quality can affect the lift dynamics on a cavitating hydrofoil. While it is well known that water quality affects cavitation behavior, a quantitative scale that accurately correlates cavitation behavior to water quality does not exist. In fact, it is unclear how the sum of various factors, such as gas content, particulate matter, and pressure history combine to characterize the tensile strength of a liquid. Indeed, even the tensile strength of a liquid can vary depending on how it is measured.

From a practical point of view, the tensile strength  $T$ , defined as  $T = P_v - P_{\text{crit}}$ , can be varied over a wide range in typical research facilities, and is a function of total gas content, system pressure and the history of the water. It should be emphasized that the relationship between tensile strength and preconditioning of the water is facility dependent. The tensile strength obtained as a result of these procedures is specific to the water tunnel being used. Different water tunnels require different procedures and a great deal of experience is necessary before water quality can be varied in a predictable manner. Care also has to be taken to ensure that there is not an excess of bubbles in the flow, which can result in pseudo-cavitation at local pressures considerably in excess of the vapor pressure of the liquid.

### Gas Content Measurement

The van Slyke apparatus is used to measure total dissolved gas content of a liquid. The apparatus arose from an investigation of gas and electrolyte equilibria in blood in the early 1920s [15.106]. Developed by Donald van Slyke, the device was originally designed to measure gas content in blood. Because the device is very accurate, easy to use, and requires a small sample amount, it is ideal for water quality investigations as well. It utilizes cavitation to bring gas out of solution by creating a Torricellian vacuum above a sample of liquid. Figure 15.29 is a photograph of the modified van Slyke apparatus used at SAFL.

Numerous researchers have developed similar devices utilizing the same basic principle. *Numachi* [15.107] modified the van Slyke apparatus to allow for separate storage of released gas and water sample. *Numachi's* device also was easier to handle [15.108].

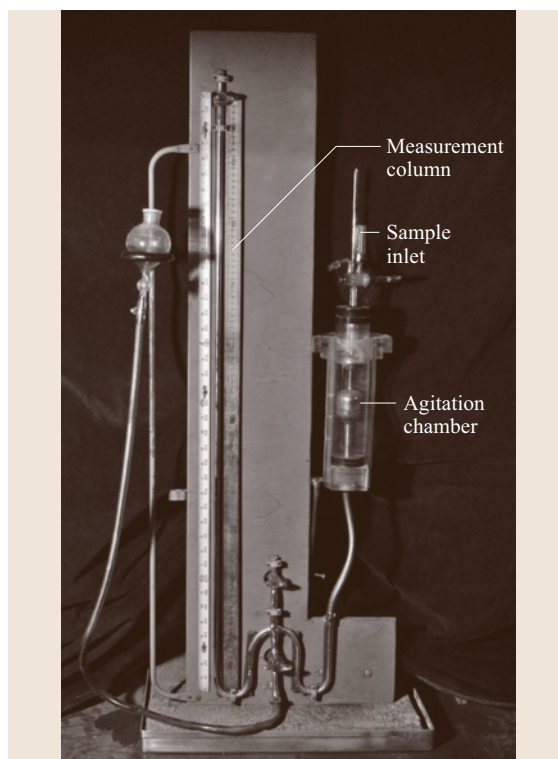


Fig. 15.29 Van Slyke apparatus

Schöneberger also made modifications to the van Slyke meter to more accurately measure gas content. Since each device is similar, only the van Slyke device will be discussed in detail. A 10 cm<sup>3</sup> sample is introduced and sealed in the apparatus. Lowering the mercury level creates a vacuum. The sample is mechanically shaken for approximately 10 min to ensure the dissolved gas is released from the sample. The partial pressure of released gas is measured and compared with the partial pressure of water vapor. The total dissolved gas is determined by the resulting pressure difference using the following relation.

$$Q = 2 \frac{273}{273 + T} \frac{P_v - P_g}{7.6}, \quad (15.14)$$

where  $P_v$  denotes the partial pressure of the vapor and  $P_g$  is the partial pressure resulting from the released gas, and  $T$  is the fluid temperature in °C.  $Q$  is the total gas content in per milliliter. It should be noted that neither  $P_v$  nor  $P_g$  is measured, but rather it is the difference that is determined from the device. While capable of measuring the total dissolved gas in a liquid quickly, accurately, and over a wide range with a small sample, the large amount

of mercury needed to operate the device has recently made it undesirable to use from an occupational health hazard point of view.

Recently, some mercury-free devices to measure gas content have been developed. Based on the same principle as the van Slyke meter, Brandt constructed and patented a device that uses an inflatable rubber membrane in place of mercury to create a vacuum; the amount of gas is determined volumetrically, therefore no pressure measurements are needed. *Heller* [15.109] developed a device that uses a bellows to create a vacuum and a pressure transducer to determine gas content. These devices, however, are not widely used or well known. Instead methods that infer total gas content from the concentration of other gases have become popular.

In an effort to replace the van Slyke meter, dissolved oxygen probes have been used to infer gas content. Most dissolved oxygen probes rely on an oxygen-permeable membrane and an electrolyte solution to determine dissolved oxygen in solution. Oxygen diffuses across a membrane into the solution where an anode and cathode are separated. The measured dissolved oxygen is a function of the current generated. While this method has been shown to be accurate in inferring total dissolved gas, caution should be taken when using this method. Unlike the van Slyke meter, this method requires regular calibration and maintenance. The solution and membrane must be periodically changed, or inaccurate reading will result. Also, it is incorrect to assume that the rate of oxygen diffusion into or out of a liquid is equal to that of other gases. The volume ratio of oxygen and nitrogen in air is not the same in water or other liquids under equilibrium conditions. In addition, the chemical oxygen demand of the tunnel water due to dissolved impurities is also a factor. While dissolved oxygen generally gives a qualitative indication of the amount of total dissolved gas, it should not be used as a method to infer total dissolved gas on a quantitative basis.

As already discussed, in addition to the difficulty of determining total dissolved gas, this parameter alone does not necessarily give a true indication of water quality. Since microscopic nuclei are needed for cavitation to occur, it is possible that a liquid with large total dissolved gas content will contain relatively few nuclei if exposed to high pressure for a sufficient amount of time. Under normal conditions, this is not the case. *Peterson* [15.110] found that the size and number of nuclei in a flow varies with gas content. *Arndt* and *Keller* [15.111] found that a doubling in gas content resulted in a tenfold increase in nuclei content.

### Acoustic Techniques for Nuclei Measurement

Acoustic determination of nuclei content has many advantages in a variety of applications. The acoustic method is non-intrusive and does not require a transparent boundary between the instrument and fluid in question. The method is based on the acoustics of bubbles. In a simplified form, a bubble can be represented by a spring-bob system. The gas within the bubble acts as a spring to external forcing. The emission of an acoustic wave into a liquid medium containing bubbles will naturally cause the bubbles to oscillate. *Minnaert* [15.7] determined the resonance frequency of a bubble as a function of the radius and free-stream pressure.

$$\omega_0 = \frac{1}{R_0} \sqrt{\frac{3\kappa p_0}{\rho}}; \quad (15.15)$$

$R_0$  and  $p_0$  denote the mean radius and pressure, respectively,  $\rho$  is the density of the liquid, and  $\kappa$  is an unknown constant to take into account the effects of heat conduction. When heat conduction effects are negligible,  $\kappa$  is unity. In theory, introducing an acoustic wave into a liquid will cause bubbles to oscillate. The resulting bubble oscillations will create acoustic waves in the liquid that are characteristic of the bubble size and number. The resulting energy scatter or absorption and attenuation of the sound wave by the bubbles are measured. This technique is termed resonance excitation or the attenuation method since it uses the resonant frequency of a bubble to determine the nuclei content in a flow.

*Duraiswami* et al. [15.112] proposed using a dispersive method to determine nuclei content. A dispersive method utilizes attenuation and the difference in the speed of sound between a liquid and gas. A pure liquid, without bubbles, will propagate sound at a different rate than a liquid with bubbles. By comparing the propagated sound speed with the theoretical value for a pure liquid, the nuclei content can be determined. *Chahine* and *Kalumuck* [15.113] used two hydrophones placed in a flow and recorded bursts of sound emitted from one and received by the other. By recording the interference caused by the bubbles, the bubble size distribution and number is determined.

Acoustic methods, however, have limitations. Acoustic methods tend to overestimate nuclei content for liquids with small nuclei, and underestimate nuclei content in liquids with large nuclei [15.112]. In addition, the accuracy is sensitive to the surrounding materials. Highly acoustically reflective surfaces can

have an adverse effect on the signal acquired [15.114]. *Leighton* [15.115] notes that, when using the attenuation method, large bubbles in a liquid can emit a stronger signal than much smaller bubbles resonating at their natural frequency. *Oldenziel* [15.116] also found that the best results are attainable only when the concentration of bubbles is low. In addition, the attenuation method assumes spherical, linear bubble oscillation.

### Optical Techniques for Nuclei Measurement

The simplest optical method uses photography. By illuminating a plane in the liquid and taking a photo, bubble size and number can be determined. This method is a simple, brute-force approach. It requires a camera with sufficient resolution, and individually measurement of the radius of each bubble in the image. In cases where nuclei content varies over a wide range, and where numerous conditions are studied, this method quickly became impractical. Recent advances in digital photography and image-processing techniques, however, have spurred interest in this method.

Holographic techniques have recently been developed along these lines. In holographic interferometry a laser beam is split into two coherent beams. One beam, the subject wave, is passed through the volume of interest. The other, the reference wave, bypasses the measurement volume and is directed onto a recording medium, where it is recombined with the subject wave. By recording the difference in amplitude and phase between the reference and subject wave, a hologram is produced.

Holographic images provide a high-resolution, three-dimensional image of a given flow sample. Once an image has been acquired and constructed, it is a matter of time to process and analyze the images. Holographic techniques provide many advantages. Direct visualization of a sample removes the need for calibration procedures. In addition to nuclei distribution, objects of all types are easily observed and distinguished, an advantage which is lacking in all other methods. In addition, holography can be used to measure objects as small as  $5\text{ }\mu\text{m}$ . *O'Hern* [15.53] was able to examine nuclei and particle distribution in oceanic waters with great detail using a submersible holographic system. In addition to the cost of a holographic system, a considerable amount of time is needed to obtain meaningful information about water quality. As is the case with the photographic method, this technique is impractical for routine water quality measurements.

*Keller* [15.117] used light scattering to determine nuclei size in a flow. Using a HeNe gas laser to illuminate a control volume, a receiver lens is positioned perpendicular to the laser and light scattered by nuclei passing through the control volume is collected by the lens. The scattered light then passes through a photomultiplier and is collected by a pulse-height processor. The intensity of the scattered light is assumed to vary with nuclei size. By knowing the light intensity, the size spectrum can be determined. The procedure requires calibration using particles of known size and number. As a result, the accuracy of the method is largely dependent on the care and precision with which the calibration is performed. This method is accurate but has many limitations. The volume of the laser light/receiver path intersection limits the maximum size that can be measured. Keller's original apparatus was used to measure nuclei in the range of approximately  $5\text{--}500\text{ }\mu\text{m}$ . In addition, only a small portion of the flow can be analyzed.

Along similar lines, phase Doppler anemometry (PDA) devices offer accurate nuclei size and velocity measurement without the need for calibration. PDA measures the phase shift created by particles passing through the probe volume and is capable of measuring particles in the range of approximately  $1\text{ }\mu\text{m}$  to  $1\text{ mm}$  [15.118]. The PDA has the advantage of measuring both nuclei content and liquid flow rate with high accuracy [15.119]. The sampling rate of the system is limited by the number of particles that pass through the probe volume in a given time, allowing for very high sampling rates. A sample, however, is taken only when a particle passes through the control volume, resulting in variable time separations between sampling. Like Keller's device the probe is not able to distinguish between solid particles and bubble nuclei, which can give potentially misleading results.

### Cavitation Susceptibility Meters

*Cavitation susceptibility meters (CSM)* have evolved from a technique for determining nuclei content that measures the inception of cavitation in a known pressure field, and compares the pressure at inception with vapor pressure. Cavitation is caused in a pre-designed area of minimum pressure ( $C_{pm}$ ). The inception events for given flow conditions are observed and recorded. Knowing the pressure at inception, a formula can be derived from the equilibrium theory for the mean number and size of nuclei in the flow.

*Schiebe* [15.120] first proposed using mathematically derived axisymmetric bodies, known as *Schiebe*



bodies, to measure cavitation inception. Using potential flow theory, a set of bodies with known value and location of  $C_{pm}$  were developed and experimentally tested. An analytical model was developed where the cavitation occurrence rate is predicted for a flow with a given nuclei content. The body is tested in a flow, and the occurrence rate is acoustically measured. By adjusting the parameters of the analytical model until the occurrence rate matches that of the experiment, the nuclei distribution of the flow was determined.

While this method proved unsuccessful, an alternative use for CSM devices was proposed. Instead of measuring nuclei content, Silberman et al. [15.122] proposed generating a set of inception event curves for a given test body under different water qualities. These curves could then serve as a reference for future cavitation tests. By measuring cavitation events on the designed test body and comparing with previously generated curves, the tensile strength of the liquid can be determined. As a result, the focus of water quality monitoring becomes one of tensile strength of the test liquid, rather than nuclei content.

CSM devices using Venturi nozzles have been developed by numerous researchers [15.109, 123, 124] to measure the tensile strength of a liquid directly. Cavitation is caused in the throat of the nozzle by increasing the flow rate until inception is observed. The pressure and the flow rate through the nozzle are measured and the pressure in the throat is inferred. If cavitation is observed at pressures well below vapor pressure, the liquid is considered strong.

Oldenziel [15.123] first proposed using a Venturi nozzle to measure cavitation susceptibility. Inception in the nozzle throat was detected visually using a shadowgraph method. A light source and photodiode are placed on opposite sides of the nozzle. The explosion of a bubble causes light scattering and a change in voltage of the photodiode. Lecoffre and Bonnin [15.124] used a steel Venturi nozzle and a pressure sensor located on the downstream side of the nozzle to measure cavitation susceptibility. Many variations of the basic concept have been developed to measure water quality. One such device is discussed below.

### Vortex Nozzle

One example of a modern susceptibility meter is the vortex nozzle. Detailed measurements by d'Agostino and Acosta [15.125] indicated that conventional Venturi devices suffer from inaccuracies due to viscous effects. To circumvent this problem, Keller [15.121] developed a so-called vortex nozzle for the measurement of tensile

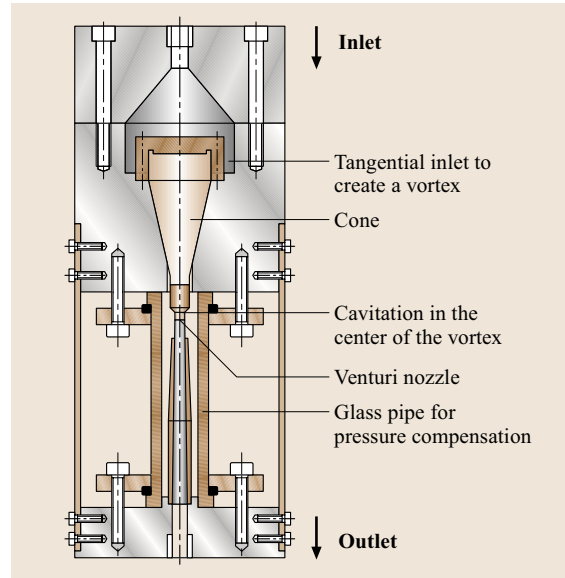


Fig. 15.30 Vortex nozzle susceptibility meter [15.121]

strength. The nozzle device consists of a vortex chamber followed by a Venturi nozzle. The vortex chamber superimposes a circulation on the flow to ensure that cavitation occurs at the center of the throat, away from the flow boundaries. The pressure drop across the nozzle is measured using pressure transducers. The throat pressure is calculated using an empirically derived equation. The throat pressure when inception occurs equals the critical pressure. With the critical pressure known, the tensile strength of the water is determined.

An empirical relation for the pressure in the throat is given by

$$P_T = P_1 - C\rho \left( \frac{Q}{A_T} \right)^2, \quad (15.16)$$

where the density and dimensions of the nozzle are assumed to be fixed,  $P_1$  is measured at the inlet to the device and  $C$  is an experimentally derived calibration constant, and  $Q$  is the flow rate. substituting  $P_T = P_v - T$ , where  $T$  is the tensile strength, and  $P_v$  is the liquid vapor pressure, the tensile strength is:

$$T = C\rho \left( \frac{Q}{A_T} \right)^2 - P_1 + P_v. \quad (15.17)$$

$Q$  is a function of the pressure drop across the nozzle, a measured quantity, thus the tensile strength of a liquid can be determined and the average nuclei size can be inferred. In the above equation,  $P_1$  and  $Q$  are determined

for the instance when inception is first observed in the vortex nozzle. Inception can be measured visually or acoustically depending on the available instruments and material with which the nozzle is constructed.

In principle, an equation for the minimum pressure in the throat area could be obtained by calculating an idealized flow in the nozzle throat consisting of a uniform axial flow and a superimposed rotational vortex the nozzle throat is of interest. *Ma* [15.102] carried out such a calculation numerically and was able to correlate the tension measured in the vortex apparatus with the tension inferred from measurements of inception in tip vortex flow.

Regardless of the techniques used to measure tension, it should be noted that tensile strength is also a function of the static pressure of the liquid. This can be inferred from a simple equilibrium model. Under equilibrium conditions,

$$P_1 - P_\infty - \frac{2S}{R} = 0, \quad (15.18)$$

where  $R$  is the bubble radius,  $P_1$  is the internal bubble pressure, and  $P_\infty$  the surrounding liquid pressure. The internal bubble pressure is the sum of both vapor pressure and pressure due to incondensable gas. The pressure due to incondensable gas can in turn be determined by the ideal gas law.

$$P_1 = P_v + P_g = P_v + \frac{M_g G \theta_g}{\frac{4}{3}\pi R^3}, \quad (15.19)$$

where  $M_g$ ,  $\theta_g$ , and  $G$  denote the moles of gas, temperature of gas, and universal gas constant, respectively. Combining (15.18) and (15.19) and letting the  $R_c$  denote the critical radius at which the bubble becomes unstable, the tensile strength is written:

$$T = P_v - P_\infty = \frac{2S}{R_c} - \frac{M_g G \theta_g}{\frac{4}{3}\pi R_c^3}. \quad (15.20)$$

It is impractical to measure the necessary quantities to determine the tensile strength of a liquid from the above equation. *Blake* [15.126] showed that, for isothermal expansion, the critical bubble radius can be written:

$$R_c = \left( \frac{9M_g \theta_g G}{8\pi S} \right)^{1/2}. \quad (15.21)$$

Substituting (15.21) in (15.20) yields,

$$T = \frac{4S}{3R_c}. \quad (15.22)$$

The ratio of the tensile strength of a liquid at two different liquid pressures is

$$\frac{T_1}{T_2} = \frac{R_{c2}}{R_{c1}}. \quad (15.23)$$

Using the ideal gas law for the pressure inside the bubble, (15.23) can be written as

$$\frac{T_1}{T_2} = \left( \frac{P_1}{P_2} \right)^{1/3}. \quad (15.24)$$

Thus, the tensile strength of the liquid scales with the cube root of the pressure. When determining the tensile strength of a liquid using any CSM device, it is important to note the pressure history and conditions under which the measurement is taken. In addition to reducing the bubble size, high pressure increases the gas saturation level of the liquid and causes gaseous nuclei to dissolve. While the theoretical estimate of the tensile strength of water is on the order of  $10^4$  atmospheres, this is never the case due to the large number of nuclei present in the liquid. When inception studies are made in a closed-circuit tunnel, it is necessary to insure that a continual supply of nuclei exists for cavitation to occur. The source of persistent nuclei in a flow has been the subject of much debate. *Fox* and *Hertzfeld* [15.127] proposed that an organic skin membrane forms around bubbles, preventing gas diffusion. Experimental evidence for this theory has been observed, but the model fails to explain why nuclei still persist in inorganic liquids and other liquids containing chemicals that should alter the behavior of the organic material. *Harvey* et al. [15.128] postulated that gas pockets become trapped in the crevices of surfaces and free-stream solid particles. These gas bubbles form concave surfaces with the surrounding liquid. The pressure in the bubble is lower than the surrounding liquid so the gas does not dissolve into the liquid. The surface tension caused by the hydrophobic surface acts to repel the liquid, establishing a stable condition for the trapped gas pocket. The pocket remains in a stable equilibrium until the vapor pressure is reached in the near vicinity. While no direct verification of the model has been made, it is generally accepted.

### 15.1.6 Cavitation Inception

#### Detection

The most common measurement in cavitation research is the determination of the conditions for inception. This may appear to be a trivial exercise, but measurements are fraught with difficulties. Although the definition of

cavitation appears to be relatively simple and straightforward, there is some ambiguity in the experimental determination of  $\sigma_i$ . The inception process tends to be intermittent and difficult to quantify (see the Appendix in [15.129] for a simple model of intermittency). One factor is the relatively large range of nuclei sizes that tend to cavitate at different values of pressure. As the cavitation number is decreased, the cavitation events occur at an increasing rate. This behavior makes it difficult to define a concise point of inception. Numerous researchers have used a microphone or hydrophone to detect inception acoustically. The rapid expansion of a bubble produces easily detected acoustic waves in the audible range. Small hydrophones placed near the inception location provide an easy and accurate method for detecting cavitation inception. Often cavitation can be detected acoustically before it can be visually observed. This method is especially advantageous in cases where visual access to the test section is difficult or impossible. *Lecoffre and Bonnin* [15.124], *Ma* [15.102], and *Heller* [15.109] used a microphone to detect inception in a Venturi-type device in order to determine tensile strength.

As pointed out later, unexpected variations in  $\sigma_i$  occur because of factors not accounted for in the basic scaling law. In addition, there is a large source of error inherent to the various methods we use to characterize the onset of cavitation. Inception is usually defined by the visual appearance of bubbles. In the laboratory, testing is normally carried out in a water tunnel at constant velocity with the static pressure slowly lowered until cavitation is observed. An alternative scheme is to lower the pressure even further and then gradually raise it until the cavitation is extinguished (cavitation desinence). There is a discrepancy between  $\sigma_i$  defined by inception and that defined by desinence. This is referred to as a hysteresis effect and has been discussed in detail by *Holl and Treaster* [15.130].

Because of the noise associated with cavitation, it has been common for many years to use acoustic techniques to define the inception point. Sample acoustic data are shown in Fig. 15.31. Figure 15.31a is a presentation of acoustic data obtained in a plug valve, plotted in the form of noise intensity in various frequency bands as a function of the cavitation index. Inception is defined by the point where there is a rapid increase in noise level with further lowering of pressure.  $\sigma_i$  so measured depends on the frequency band of the data, the low-frequency noise being relatively insensitive to cavitation index. A different acoustic technique is illustrated in Fig. 15.31b where the number of cavitation

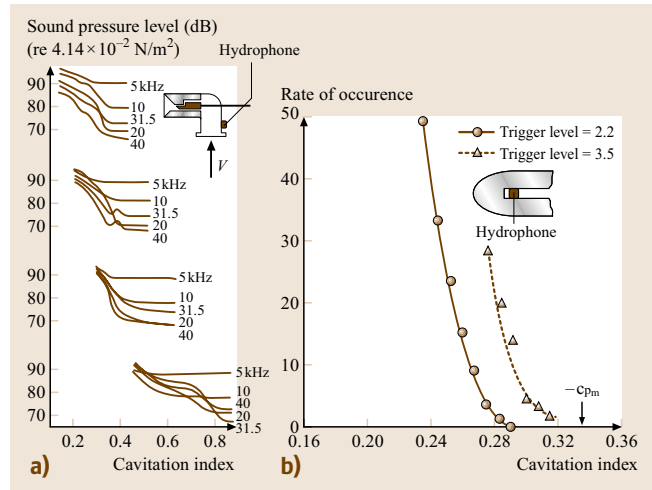


**Fig. 15.31a,b** Acoustic inception techniques [15.15]. (a) Acoustic intensity method. (b) Rate of occurrence

events per unit time is determined with a hydrophone and an electronic counter. To isolate the cavitation noise from background noise, a Schmidt trigger arrangement is used. In this situation,  $\sigma_i$  is defined by a rapid rise in the rate of occurrence. Unfortunately, the measured value of  $\sigma_i$  is sensitive to the threshold level of the Schmidt trigger, as shown in the diagram. While this method is useful to determine the first inception event, it has proven unable to measure the number of inception events accurately. *Pham et al.* [15.114] compared the number of inception events in a combination Venturi-center body-type device as measured acoustically, and

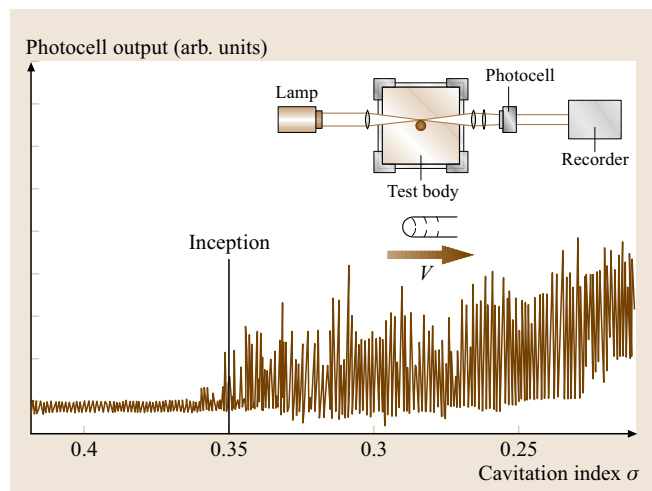


**Fig. 15.32** Example of an optical detection technique [15.15]

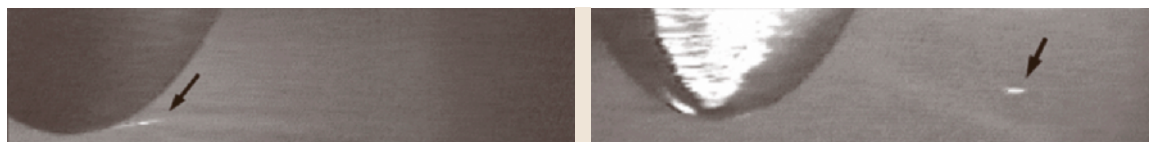


**Fig. 15.33** Tip vortex inception in weak water (*left*) and strong water (*right*). The cavitation number for inception in strong water is so low that sheet cavitation on the surface of the foil occurs before vortex cavitation inception [15.131]

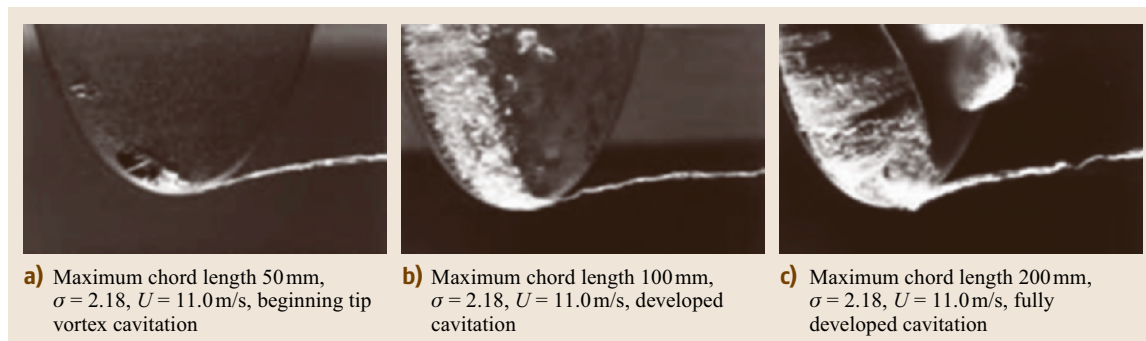


**Fig. 15.34a–c** Size scale effect on a [NACA 16-020](#) hydrofoil [15.104]. **(a)** Maximum chord length 50 mm,  $\sigma = 2.18$ ,  $U = 11.0$  m/s, beginning tip vortex cavitation **(b)** Maximum chord length 100 mm,  $\sigma = 2.18$ ,  $U = 11.0$  m/s, developed cavitation **(c)** Maximum chord length 200 mm,  $\sigma = 2.18$ ,  $U = 11.0$  m/s, fully developed cavitation

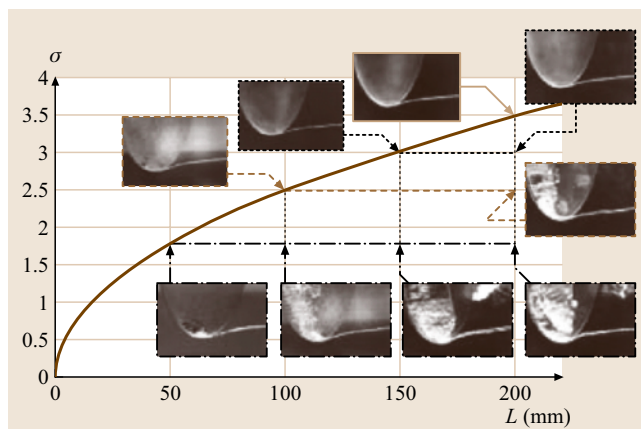


**Fig. 15.35** Size effect on inception for tip vortex cavitation on a [NACA 16-020](#) hydrofoil [15.104]

with high-speed video. They found that the acoustic counting technique overestimated the number of inception events by as much as seven times compared with the number seen using high-speed video. It may be for similar reasons that *Schiebe's* [15.120] method was unsuccessful.

Visual detection of inception is an accurate method when the necessary tools are available. As previously mentioned, *Oldenziel* [15.123] used a light source and

a photodiode to measure inception in a Venturi device. An example of an optical detection scheme is shown in [Fig. 15.32](#). This method is based on the determination of scattered light that has been focused in the minimum-pressure region of a test body. With the use of a laser setup, several investigators have successfully used this technique. *Arndt and Keller* [15.131] used high-speed video tripped by a laser to compare vortex inception for a three-dimensional (3-D) hydrofoil in strong and weak water. By positioning a laser in the center of a trailing vortex, a high-speed digital video camera was set to record the instance a vapor bubble crossed the laser path. Using this technique, *Arndt and Keller* [15.131] found that inception occurs near the foil tip under weak water conditions, while inception occurs far downstream under strong water conditions ([Fig. 15.33](#)).

The basic detection schemes are all subjective to some extent and can lead to discrepancies between data collected in different facilities. Unfortunately, there is no clear distinction between observed variations in  $\sigma_i$  due to the detection scheme used and variations in  $\sigma_i$  due to a fundamental difference in environmental factors. It should be emphasized at this point that cavitation inception as defined by a measurable reduction in the performance of a hydraulic machine has no relevance to this discussion since a state of fully devel-



oped cavitation is associated with measurable changes in performance.

### Scale Effects

Keller [15.104], in an extensive review of the subject, pointed out that the first step in analyzing scale effects, defined as variations in  $\sigma_i$  with size and velocity, is to remove the ambiguity concerning the critical pressure,  $p_c$  in (15.1). As a historical note, Parsons used hot water in his 1895 water tunnel as a means of lowering the cavitation index, thereby allowing inception studies at relatively low velocity [15.132]. This is not recommended because of thermal effects [15.1]. He adjusted the tensile strength of the water to zero and methodically determined that there are other scaling factors for a variety of body shapes that vary as

$$\sigma_i = \sigma_0 \left( \frac{L}{L_0} \right)^{1/2} \left( \frac{v_0}{v} \right)^{1/4} \left[ 1 + \left( \frac{U_\infty}{U_0} \right)^2 \right], \quad (15.25)$$

where  $L$ ,  $v$ ,  $U_\infty$  are characteristic length of the body, the viscosity and velocity, respectively.  $L_0$ ,  $v_0$  and  $U_0$  are reference values and  $\sigma_0$  is a constant. According to Keller, knowing  $\sigma_0$  for a given body contour and type of cavitation the cavitation index can be predicted for every size, flow velocity and viscosity of the fluid. Keller also had a correlation for turbulence level, but it is felt by the authors that there is insufficient data to support this correlation fully. Although this correlation is supported by a very extensive set of experimental data, there is no theoretical underpinning to these results. A size scale effect is illustrated in Fig. 15.34.

This illustrates the appearance of cavitation with increasing size when cavitation number and velocity are held constant. A further indication of this effect is given in Fig. 15.35. Note the increase in  $\sigma_i$  with increasing size, in accordance with (15.25). Note also the increasing development of cavitation with size if  $\sigma$  is held constant.

### Gas Content Effects

Care must be exercised in adjusting water quality to a low value of tensile strength. A relatively high gas content can obscure the basic physics that are being investigated. This is illustrated with some data originally presented and discussed by Holl [15.31], plotted in Fig. 15.37. These data illustrate the occurrence of two different types of cavitation on a NACA 16012 hydrofoil section. The lower set of data corresponds to band-type cavitation, which disappears uniformly across

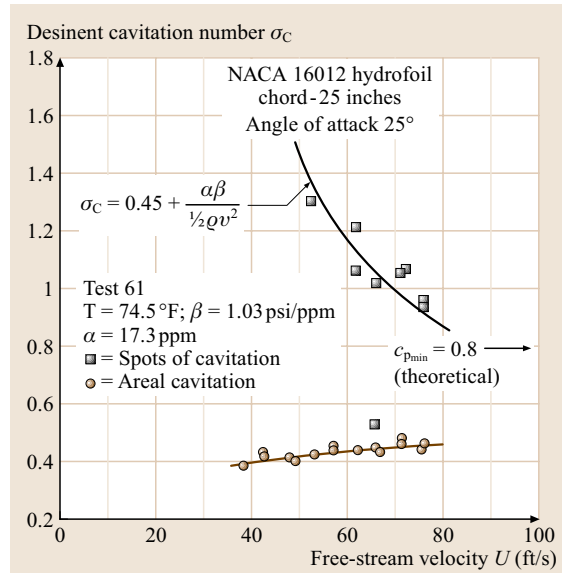


Fig. 15.36 Example of two types of cavitation on a NACA 16012 hydrofoil [15.31]

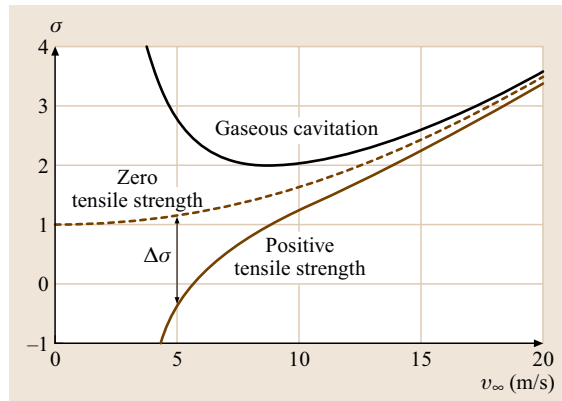
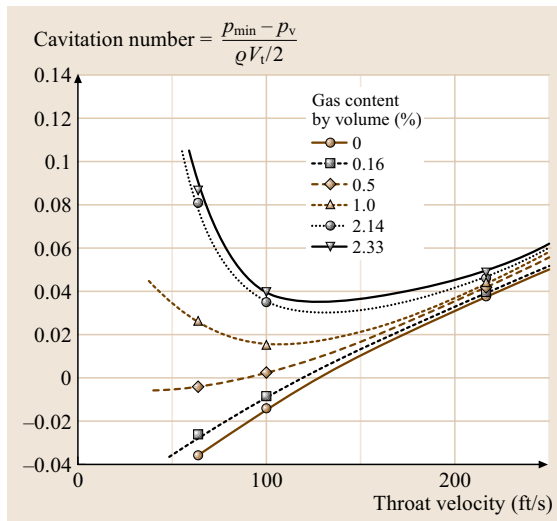


Fig. 15.37 Schematic representation of the gas content effect [15.104]

the span at the desinent value of the cavitation index. A second type, consisting of random spots, was also noted, having a much higher desinent cavitation index. The critical cavitation index for the former increases with velocity while it decreases for the latter type. Holl theorized that the former type was vaporous cavitation whereas the latter type was not vaporous cavitation at all, but instead a different type of bubble growth due to gaseous diffusion, very similar to the bubble formation occurring when the ambient pressure in a bottle of soda water is suddenly reduced upon opening. This so-called



**Fig. 15.38** Cavitation inception number for a Venturi device for several values of gas content [15.104]

gaseous cavitation follows a different scaling law, as given by (15.7). Sometimes the gas content effect is more difficult to distinguish, especially when vaporous cavitation is strongly dependent on velocity. This is shown schematically in Figs. 15.36, 37.

In summary, a review of previous laboratory experiments indicates that the details of the cavitation inception process are not adequately described by a single physical parameter such as the cavitation index. Previously overlooked details of the flow field can play a major role in the inception process and cavitation can occur when the local pressure is higher or lower than the vapor pressure. Ordinary liquids can sustain tension and more than one type of inception mechanism is pos-

sible on a given class of body. Thus, care must be taken to distinguish between the different forms of cavitation when attempting to arrive at scaling relationships.

### 15.1.7 Measurements in Cavitating Flows

In addition to classical measurements of flow necessary for understanding the inception process, it is necessary to make measurements in cavitating flows.

#### High-Speed Photography and Video

Due to the complexity of cavitating flows (essentially three-dimensional, nonstationary, turbulent two-phase flows with phase change) photography and cinematography are very important tools when studying cavitation phenomena. One look at any text on cavitation, e.g., Knapp et al. [15.19], makes it clear how much insight can be gained this way. As with all experimental techniques, *spatial and temporal resolution* are key. Time-resolved photography or cinematography can be achieved by very short illumination times while working in a totally dark environment. Good results have been obtained by letting the duration of a stroboscopic flash (typical strobe illumination time: 3  $\mu$ s) determine the exposure time, examples are shown in Figs. 15.7, 10, 12, 13, 40, 46, 47. Another option is to use cameras capable of extremely short shutter times, either mechanically or electronically, such as high-speed complementary metal-oxide-semiconductor (CMOS)-based cameras and continuous illumination. Commercially available video equipment is capable of frame rates as high as 250 000 frames/s. Some laboratories are equipped with special cameras that are capable of frame rates as high as 2 000 000 frames/s. On the other hand, when combining long exposures (i.e., non-time-resolving shutter times) with continuous illumination, *time-averaged* pictures of cavitation can be taken. Spatial resolution is a function of the recording medium and the optical setup. It should be adjusted so that the smallest events of interest are sufficiently resolved.

#### Simultaneous Imaging of Different Views

Using mirrors in test sections with optical access from at least two sides, two (or more) views of cavitating flows can be imaged simultaneously. It is important that mirrors are placed so that the optical paths for each view are of equal length, allowing focusing on both at the same time. Figure 15.39 shows a configuration used in the SAFL high-speed water tunnel, Figures 15.40 and 15.41 show sample frames taken with a high-speed

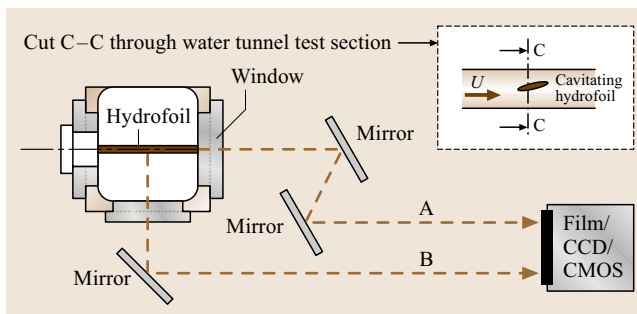


**Fig. 15.39** Simultaneous imaging of different views, optical arrangement for photography/video of cavitating hydrofoils in SAFL high-speed water tunnel. Optical paths for side view (A) and bottom view (B) are of equal length

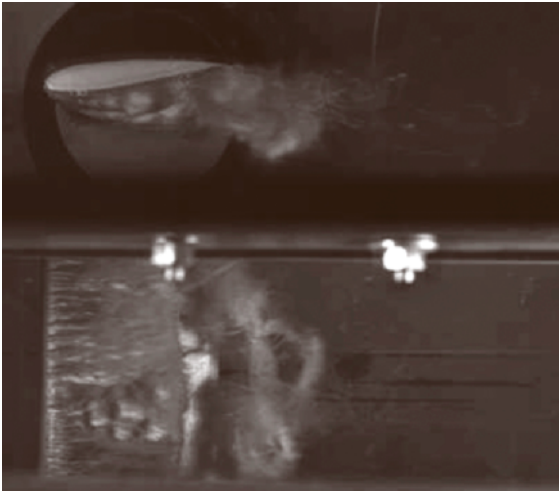


**Fig. 15.40** Sample frame from high-speed video of cavitating NACA 0015 hydrofoil, simultaneous imaging of side and bottom view (2000 frames/s, shutter time  $\approx 500 \mu\text{s}$ ,  $U = 8 \text{ m/s}$ ,  $\sigma = 1.00$ ,  $\alpha = 8^\circ$ )

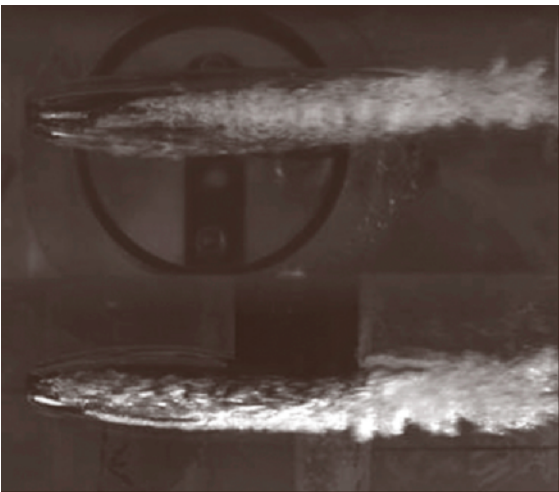


**Fig. 15.41** Sample frame from high-speed video of a ventilated supercavitating body, simultaneous imaging of side and bottom view (2000 frames/s, shutter time  $\approx 500 \mu\text{s}$ ,  $U = 7.8 \text{ m/s}$ )

camera [2000 frames/s, field of view (FoV)  $1024 \times 1024$  pixels].

### Pressure Measurements in Erosion Studies

In viewing the current state of knowledge in this field, it becomes clear that further advances in cavitation re-

search require a method for relating erosion rate to the amplitude of pressure transients striking the solid boundary during the collapse of cavitation bubbles. Methods have been developed for measuring in situ the impulsive pressures due to cavitation in both laboratory experiments and in the field. Various techniques have been explored in the past to measure the pressure transients both spatially and temporally. Most studies are made with conventional pressure transducers. However, the environment for pressure measurement equipment can be severe and it has been found that conventional pressure transducers often have unacceptably high failure rates. Recently, piezoelectric polyvinylidene fluoride (PVDF) polymer film has been used extensively in dynamic measurement and control. This film has been adopted for the measurement of impulse pressures in the study of cavitation erosion [15.40, 59].

Pressure transducers can be constructed in-house from piezoelectric film. The integral component of the film is a polarized PVDF polymer. This material is known for its high degree of piezoelectric activity. As outlined in Arndt et al. [15.59], the use of this technology for hydrofoil tests requires special development. One example of the basic measurement technique is shown in Fig. 15.42. In this example, a matrix of sensors was used to instrument an interchangeable plug on a hydrofoil for water tunnel tests. A grid of 14 piezoelectric pressure transducers was attached to a removable section of the suction side of the foil as shown in Fig. 15.43. Considerable effort was expended in developing the method

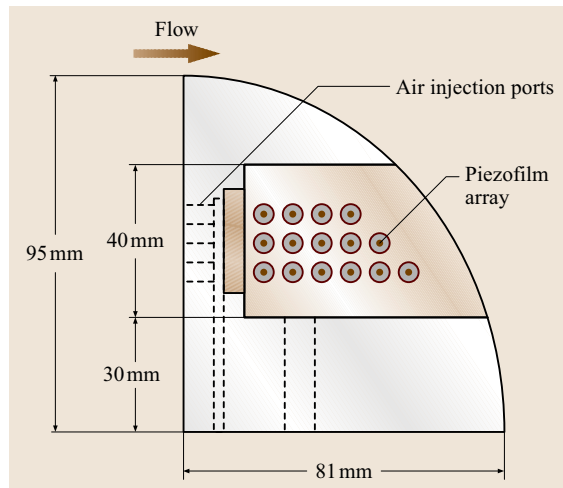


**Fig. 15.42** View of a pressure film instrumented NACA 0015 hydrofoil. This setup was used to study the effects of air injection on minimizing erosion

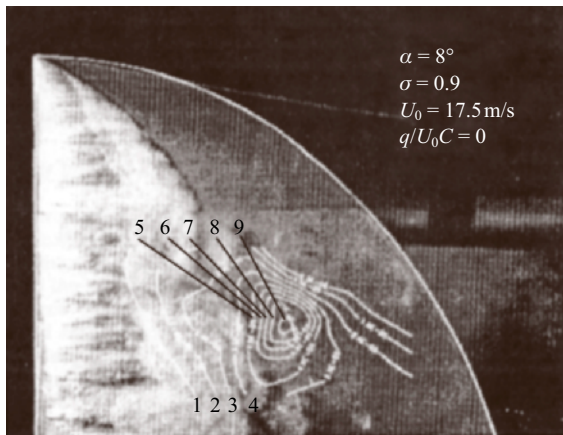


**Fig. 15.43** View of sheet/cloud cavitation on the NACA 0015 hydrofoil shown to the left. ( $U = 17.5 \text{ m/s}$ ,  $\sigma = 0.9$ ). Superimposed on the picture are isobars of mean square pressure measured with the piezometric film array

of layout, mounting, and architecture of the transducer matrix finally used.

Normally this technique is only suitable for transient response. Calibration can be achieved using a dropping ball technique or by sudden unloading of the film. The latter can be achieved with a special device whereby a pencil lead is gradually loaded until it breaks, suddenly releasing its pressure on the film. Inspection of the transient output from the transducer can be used to determine the frequency response, which can be quite high. Details concerning time and spatial resolution can be found in Arndt et al. [15.59].

A further example of using an array of piezoelectric film transducers is shown in Fig. 15.45. The test setup is shown in Fig. 15.19. Numerical simulations of cavitation cloud collapse indicate that cavity collapse occurs at approximately 75% of chord for the conditions tested. A plot of RMS pressure as a function of the composite parameter  $\sigma/2\alpha$  and relative position on the foil indicates that the most intense erosion will take place when  $\sigma/2\alpha = 3.0$  at a relative position of about  $x/c = 0.75$ , in agreement with the numerical simulations [15.39].

#### Conditionally Triggered Photography of Sheet Cavitation

As another application of pressure measurements, the transducer array cited above can be used to obtain phase-locked photos of the cavitation process. As already noted, sheet/cloud cavitation can be very periodic for a given set of operational parameters. Often it is desired to obtain a series of photographs to accompany data

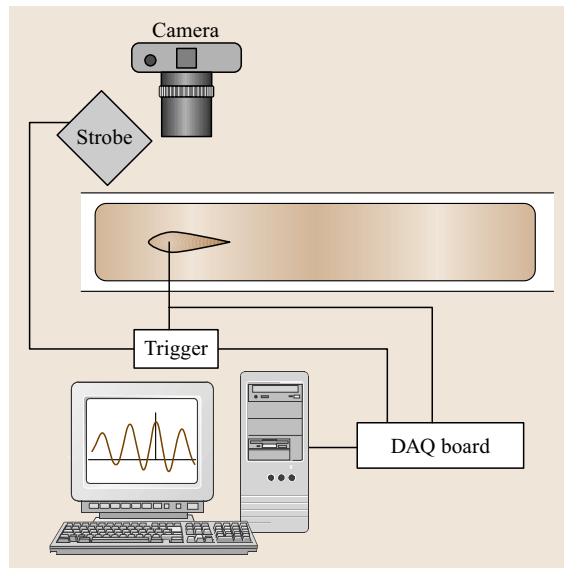


**Fig. 15.44** Schematic of a typical setup for conditionally sampled photos

from an array of piezoelectric film transducers. This technique can provide information about the relationship between cavity location and pressure distribution. The best method to accomplish this would be to use a high-speed video camera that is synchronized to the data-acquisition system. Budgetary constraints often preclude the use of such a system. However, the periodicity of the flow can be exploited. By obtaining a series of photos with different delay times relative to the pressure signal a montage of photos can be obtained that can be used to construct a virtual film of the process.

To sample a pressure signal whose period and phase are correlated with the flow, the beginning of a period, as defined by the maximum of a pressure signal, can be sensed. Using a delay circuit to trigger a stroboscope a series of photos at relative times within a period of oscillation can be obtained. In principle, several photographs can be taken at each phase and ensemble-averaged. However, photographs taken at equal time delays are found to be remarkably consistent. It is recommended that the photographs be taken in total darkness. Typically a photograph is taken by manually opening the shutter, using a computer program to trigger two strobe lights simultaneously, and then the shutter is manually closed. By performing the procedure in this manner, the exposure, as well as the time that each photograph is taken, is determined by the firing of the strobes.



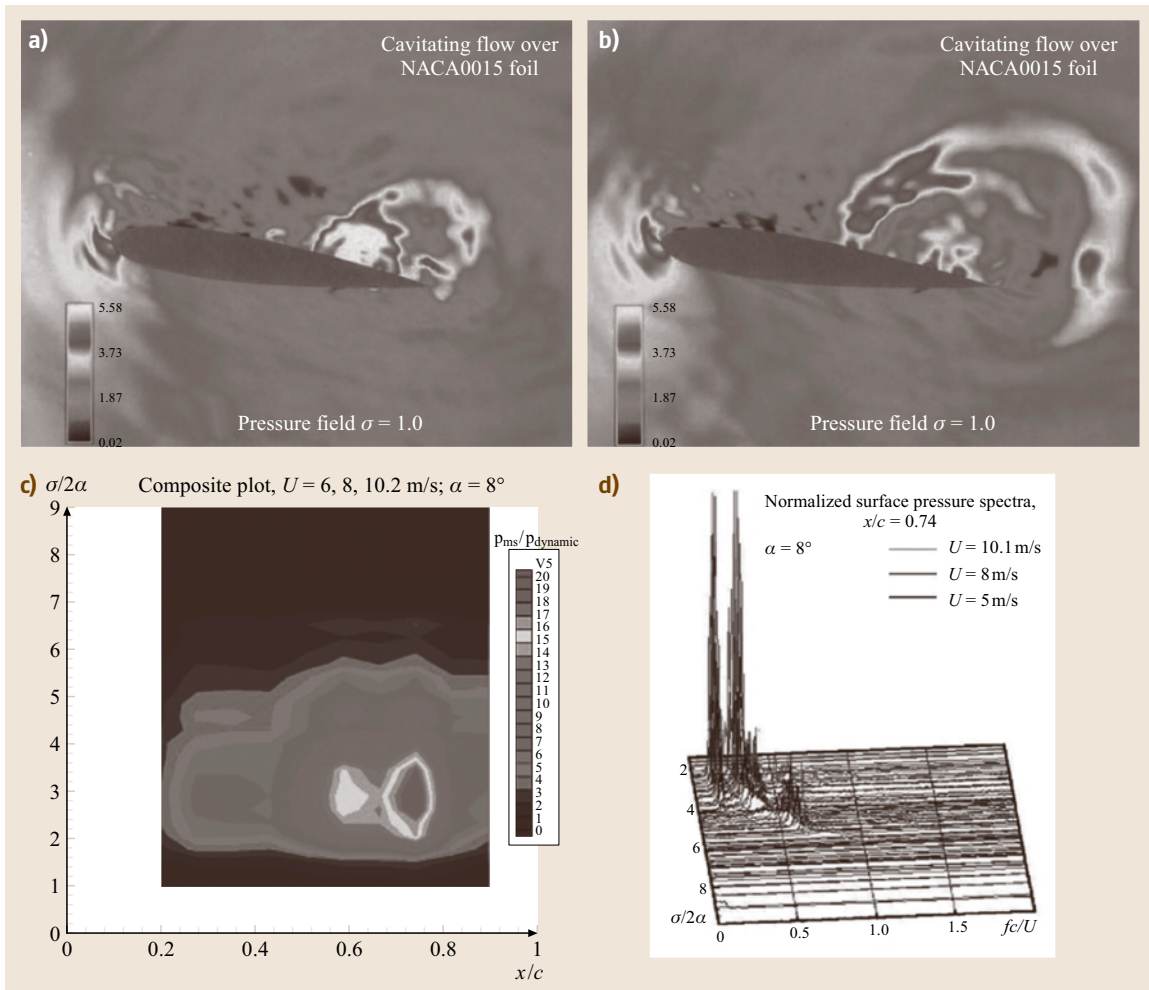


**Fig. 15.45a–d** Numerical simulations indicate intense cloud collapse at about  $x/c = 0.75$ . This is confirmed by measurements of pressure using an array of piezoelectric film transducers. Note the similarity of the pressure spectra to the lift spectra shown in Fig. 15.11 (a) Instant of cloud collapse (b) Radiation of pressure wave after collapse (c) **RMS** pressure versus  $\sigma/2\alpha$  and  $x/c$  (d) Pressure spectra

A programmable triggering system affords much greater flexibility than a hard-wired triggering circuit. A technique in use at the St. Anthony Falls Laboratory utilizes a computer code originally developed at the Arizona State University for use with Metra-byte DAS-16 compatible data-acquisition boards that were modified to suit the current needs. A typical setup is shown schematically in Fig. 15.44. To remove the effect of errors resulting from the time delay introduced by the amplifier and the trigger circuit internal to the strobe lights, the light intensity was measured with a photocell, and recorded simultane-

ously with the other data. Postprocessing shows directly when the strobes lights fired relative to the pressure signal, and hence the time that the photograph was taken.

Typical results are shown in Fig. 15.46. Photos taken at two instances of time one corresponding to a positive peak in pressure and the other to a negative peak in pressure are shown. In general this method requires a considerable amount of fine tuning depending on the physics of the flow. Finally a third example is a study of the physics of a bubbly wake produced by a cavitating hydrofoil is shown in Fig. 15.47. Numerical simula-

tions reveal that coherent vortex structures exist in the wake.

As a final note, other signals can be used to trigger stroboscopic lighting. *Arndt* and *Maines* [15.133] made measurements of nucleation in a tip vortex using a new system consisting of a laser beam as a *trip wire*, a threshold/delay circuit, strobe lighting and a standard 35 mm camera with an extension bellows for magnification. As a nucleus enters the vortex core and cavitates, it passes through a laser beam, scattering light that is picked up by photoamplifier, which in turn triggers the delay circuit. At the end of the delay strobe lighting is activated. By assembling a sequence of photos at several delay times, the equivalent of frame rates as high as 40 000 frames/s could be achieved. The same laser trip technique was used to trigger a high-speed video camera for observations at another laboratory with startling agreement between the data sets obtained in two different laboratories with two different visualization techniques [15.131] (Fig. 15.33).

### Lift and Drag

Lift and drag measurements in a water tunnel are difficult even in non-cavitating flow. Most lift balances in use in small water tunnels are designed for steady conditions. A typical balance design incorporates the use of cantilever beam elements and strain gages to sense deflection. The challenge in force balance design is the need to eliminate *crossstalk* between lift and drag. Many balances have been designed in-house and are constructed with custom-made components. An example of such a balance is shown in Fig. 15.48a. This balance was successfully used at the Saint Anthony Falls Laboratory for many years [15.32]. Recently a variety of load cells have become available at reasonable cost. These provide the opportunity for constructing reliable balances at reasonable cost (Fig. 15.48b).

Measurements in cavitating flows place additional requirements on balance design. Cavitation often induces unsteady oscillations in the lift and drag that are often in a frequency range that is beyond the natural frequency of a typical force balance. *Kjeldsen* et al. [15.32] attempted to circumvent this problem using two flush-mounted pressure transducers at the base of hydrofoil, one placed on the pressure side and the other on the suction side. This provided a method to measure the instantaneous values of the pressure difference between the suction and pressure side of the foil. The main motivation for using this transducer configuration is to obtain an independent metric for fluctuating lift since the frequency response of a typ-

ical force balance is not adequate for resolving lift and drag dynamics in cavitating flow. Individual needs will of course vary. *Kjeldsen* et al. were able to confirm that  $\Delta p$  is proportional to  $C_l$  as expected, although this technique is not in general use. *Arndt* et al. [15.39] utilized a new force balance configuration that utilizes piezoquartz force sensors (Fig. 15.49). Although the frequency response of this type of force balance is high, it is generally not suitable for steady force measurements. *Arndt* et al. [15.39] found that, for the case of lift oscillations on a cavitating hydrofoil, the pressure difference technique and force balance technique gave similar results (Fig. 15.50).

### Acoustic Measurements

Acoustic measurements in water tunnels are difficult because of reverberation. This is an acute problem in water tunnels because of the relatively long wavelengths of radiated sound. For example, a sound signal with a frequency of  $c/U$  would have a wavelength of  $ac/U$ , where  $a$  is the speed of sound and  $c$  is a typical length scale, e.g., the chord length. The long acoustic wavelengths relative to typical tunnel dimensions implies that the test environment is highly reverberant, necessitating very sophisticated acoustic calibration procedures. However, qualitative measurements can still be made effectively. An example is the use of an acoustic signal for inception detection (Fig. 15.31).

A limited number of examples of measurements of cavitation noise in water tunnels can be found in the literature [15.131, 134, 135]. For example, *Higuchi* et al. [15.135] were able to distinguish between tip vortex cavitation noise and surface cavitation noise by using two different hydrofoils designed such that surface cavitation occurred on one hydrofoil in the absence of tip vortex cavitation and tip vortex cavitation occurred in the absence of surface cavitation on the other. A special feature of this study was the use of an array of hydrophones to locate the inception location in a tip vortex. This is shown in Fig. 15.51. The experiment was made in a high-speed water tunnel. The acoustic signature was monitored by four Brüel and Kjær (B&K) model 8103 hydrophones (Fig. 15.52) positioned in a water-filled chamber separated from the test section by an almost acoustically transparent wall. A similar setup was used by *Barker* [15.136]. Both the pressure fluctuations due to the turbulent boundary layer on the test section wall and the water tunnel background noise were measured to be insignificantly low, compared to the cavitation noise. On the other hand, the test section was found to be highly reverberant.

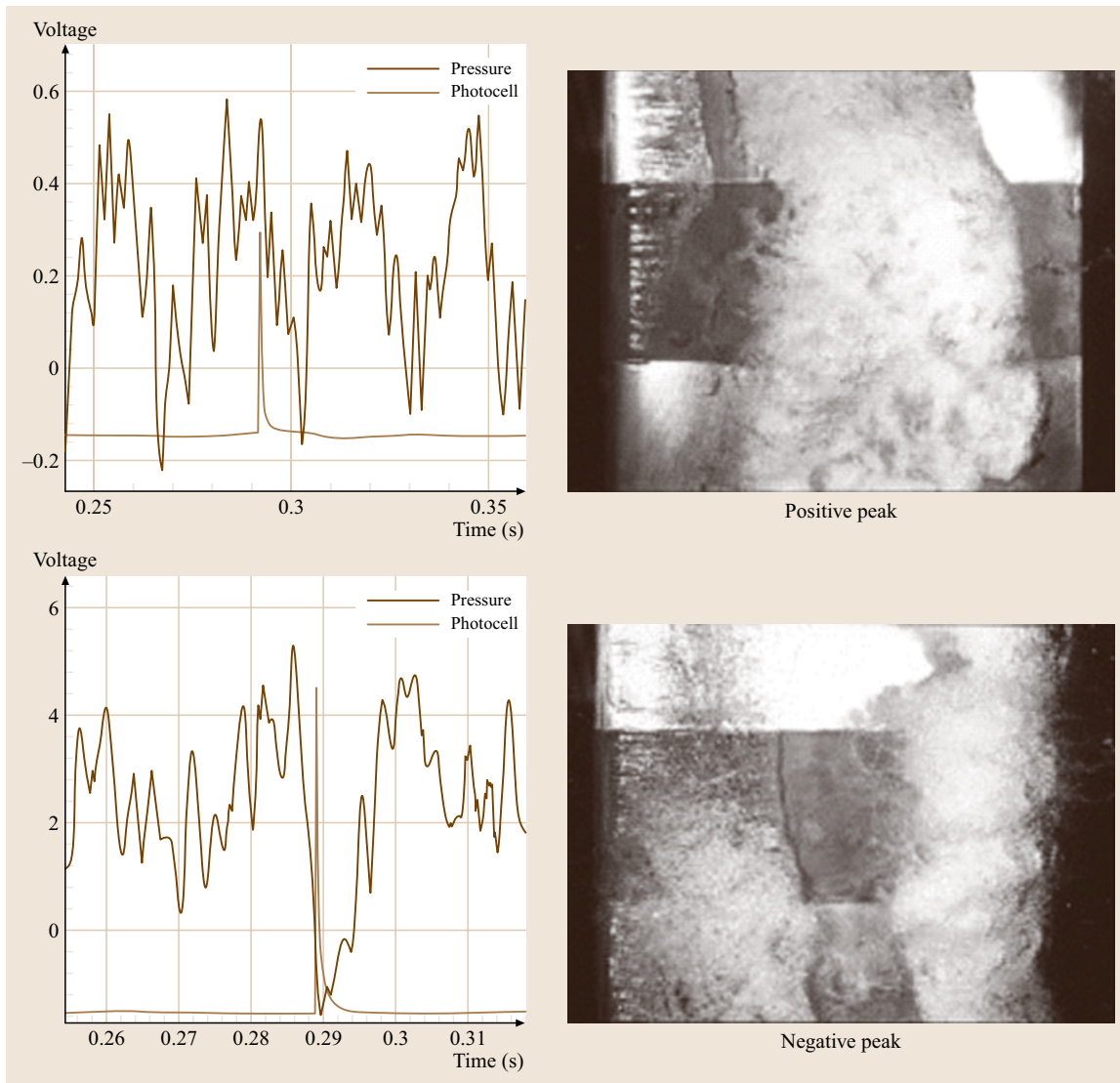


**Fig. 15.46** Conditionally sampled photos of sheet cloud cavitation

The hydrophones were first calibrated in a large water tank where an acoustic free field could be simulated. Using a spherical projector, high frequency (typically a 60 KHz sine wave) tone bursts were generated and measured with the hydrophone array. Each hydrophone in the array was placed in the same relative position as in the water tunnel. In order to calibrate both the hydrophone array and the acoustic characteristics of the water tunnel itself, the projector was next placed in the test section in place of the hydrofoil. By triggering the digital oscilloscope with the projector pulse, the

output from the individual hydrophones was simultaneously digitized. The initial pulses in these traces were the projector output itself via direct path, which had the same waveform as the near-field measurement of the projector signal. The subsequent pulses reflected by the tunnel walls could be clearly identified by this technique and were in qualitative agreement with a computer simulation of the reverberation in the tunnel.

Cavitation inception could be detected both visually and acoustically. Inception was marked by a distinct burst of noise in the flow field. By pre-triggering an

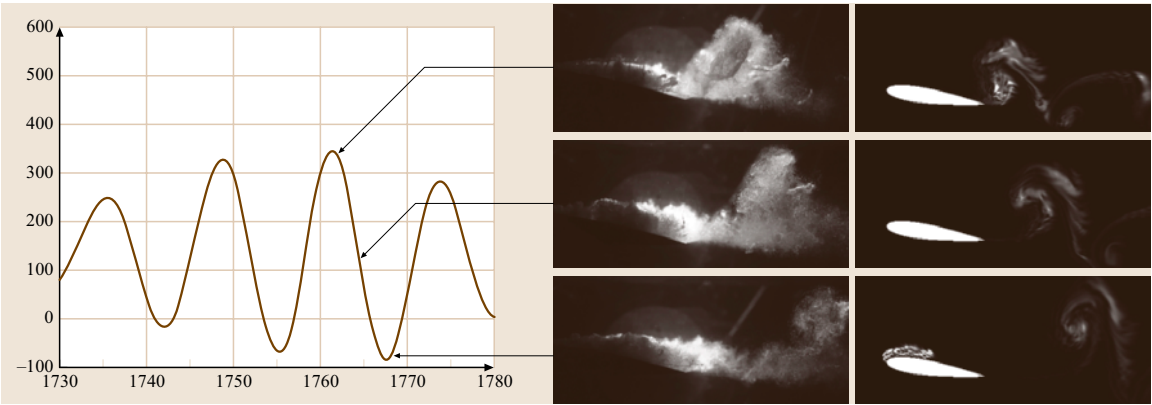


**Fig. 15.47** Comparison of phase locked photos of cavitation (*left column*) with numerical simulations of incondensable gas that has come out of solution as a result of the cavitation [15.137]

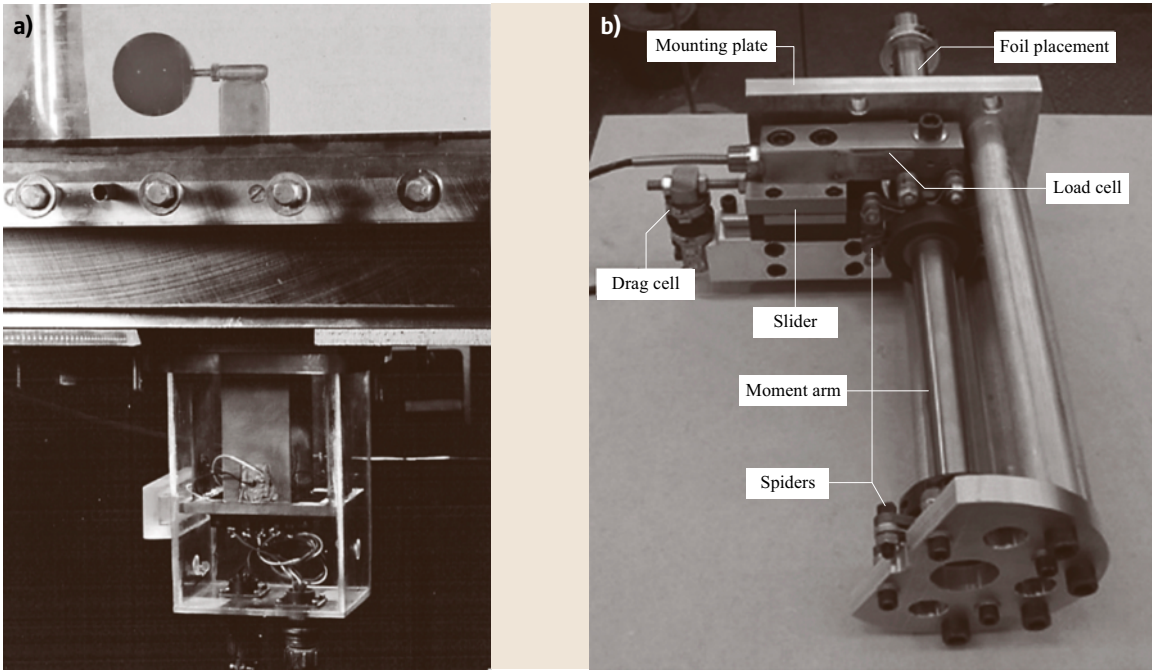


**Fig. 15.48a,b** Typical force balances (courtesy of Saint Anthony Falls Laboratory) (a) Force balance installed in the SAFL high-speed water tunnel. A sphere test for turbulence level is being performed. (b) New replacement balance for the one shown in (a). This balance utilizes off-the-shelf load cells

analog-to-digital (A/D) converter with the hydrophone signal itself, individual instantaneous pressure time traces at four different locations could be recorded. By measuring the time delay of arrival among the four hydrophones, the sound source location could be estimated by a triangulation method. The three time delays among the four time traces define three two-dimensional mani-

folds. The intersection of these manifolds is the location of the noise source. Given three time delays among four hydrophones as inputs, implicit simultaneous equations for the three coordinates of the sound source can be solved iteratively.

A technique for dealing with the effect of tunnel reverberation was studied for the case of surface cavitation



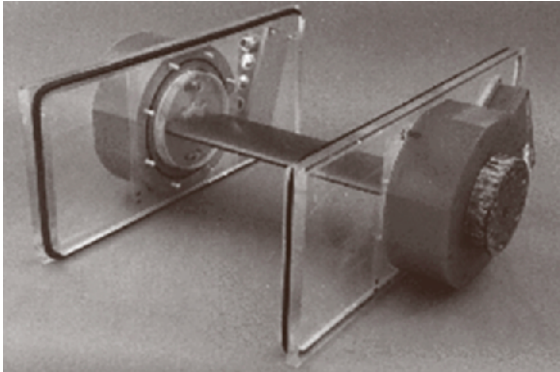


**Fig. 15.49** Piezoquartz force balance used to measure fluctuating lift on a cavitating hydrofoil [15.39]

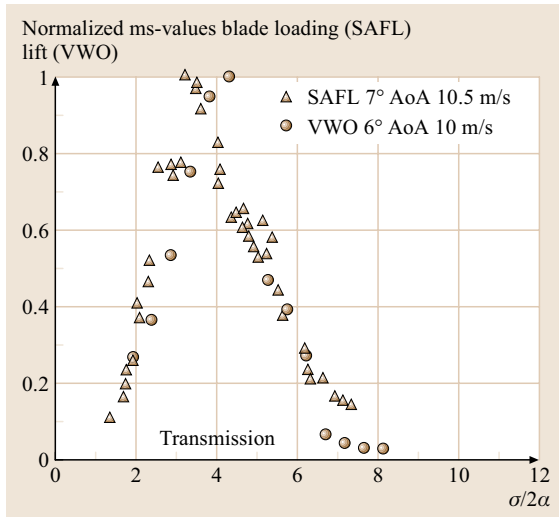


**Fig. 15.50** Comparison of lift oscillation data obtained with  $\Delta p$  measurements made at SAFL with force balance measurements made at Oberrach, Germany

inception. Since the individual pulses were recognizable in the signal, a Fourier analysis can be performed on the individual pulses. The waveform of a single bubble collapse in the free field was obtained by ensemble-averaging the acoustic cavitation inception data. Using this waveform, single-bubble noise in the presence of reflections from the tunnel walls could be simulated numerically. The computed effect of reverberation on the power spectrum was calculated by comparing the power spectrum of a simulated single-bubble collapse with the power spectrum of a simulated pulse with reflections. The spectrum of the reverberant signal was found to match very closely that of the original free-field pulse

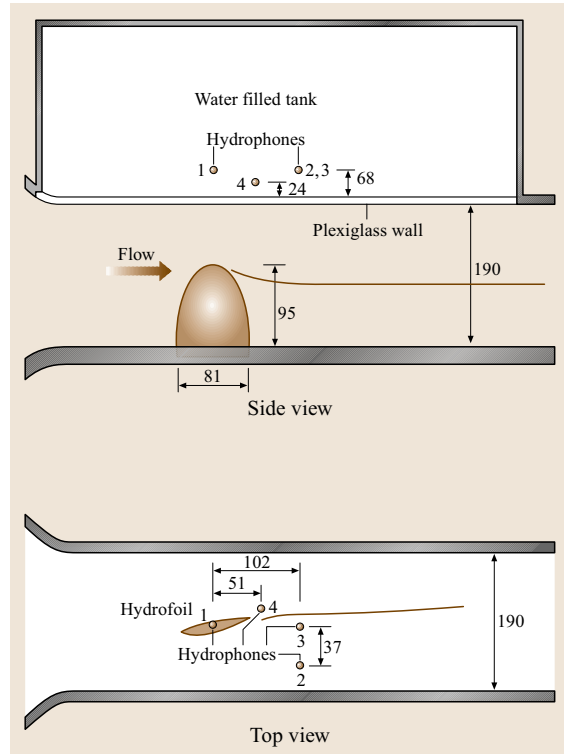


**Fig. 15.51** Experimental setup for detecting the location of inception in a tip vortex [15.135] (All dimensions in mm)



**Fig. 15.52** Typical commercially available hydrophones (courtesy of Brüel and Kjær)

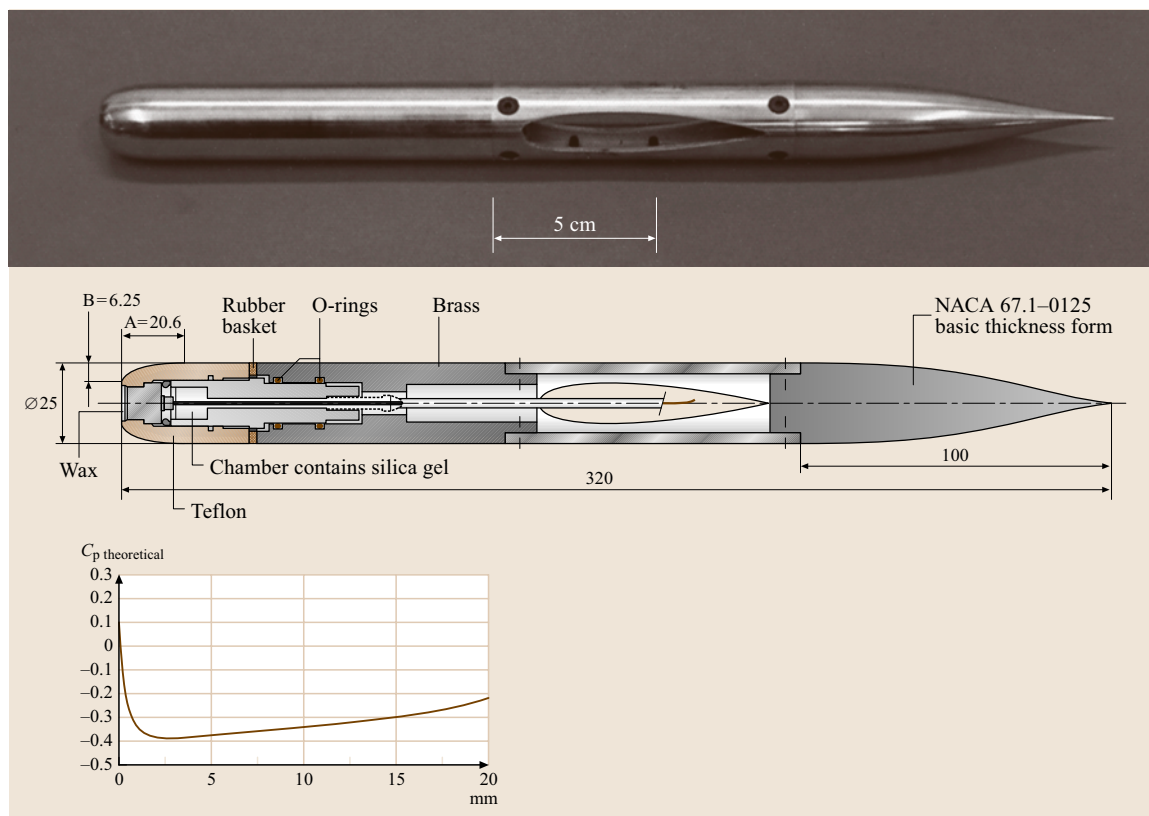


**Fig. 15.53** Specially designed hydrophone body for inflow acoustic measurements [15.131]

when the spectra were normalized to maximum amplitudes. In the study by Higuchi et al. [15.135] the amplitude of the reverberant spectrum was approximately 7 dB higher than that of the free field in this example, and appears to scale with the number of reflections from each individual pulse. The result will differ in each facility but the lack of distortion of the inception noise spectra due to reverberation is an encouraging result.

Another technique for measuring inception noise was reported by Arndt and Keller [15.131]. The effects of nuclei content were studied in a series of comparative tests in a water tunnel and the Vacutank at the Marine Institute, Netherlands (Fig. 15.21). This investigation required careful planning because of the required remote operation in the Vacutank due to the very low operating pressures. Only values of  $\sigma$  greater than 1 could be achieved in both facilities. With the desire to use a fixed body rather than a model propeller, a series of sharp-edged disks of 2, 4, 8 and 16 cm diameter were manufactured. The disk geometry was selected because of its relatively high cavitation number. The four differ-

ent sizes were selected not only to provide an overlap in Reynolds number in the two facilities, but also an overlap in time scales of the shear layer turbulence ( $\tau \approx d/U$ ). At the time this was thought to be an important factor in the inception process. The relative disk thickness, shaft diameter etc. were fixed at the same values used in the classic study of Kermeen and Parkin [15.138]. Pressure ports were located in the supporting shaft of each disk so that the time-averaged pressure could be measured at various positions in the wake. The three largest disks were also fitted with accelerometers to allow an independent check on the acoustically measured cavitation event rate.

Inception observations were carried out both visually and acoustically in the water tunnel. These tests served to verify the hydrophone design and mounting system that had to be developed to perform remotely monitored inception tests in the Vacutank. The sensing element is a special hydrophone, designed and manufactured by the Physical Laboratories, TNO, model ZP 84 (early research utilized an Atlantic Research

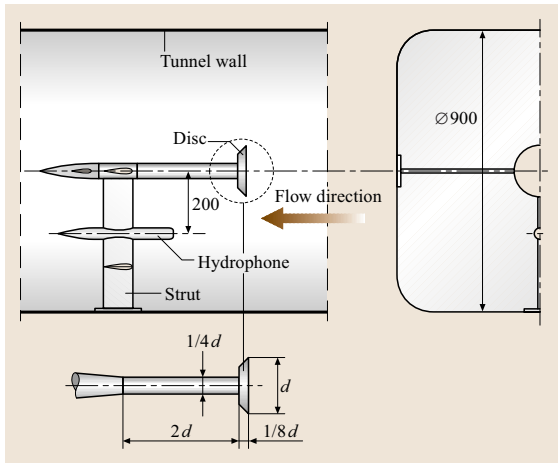


**Fig. 15.54** Water tunnel installation for measuring inception noise [15.131]

LC-60 hydrophone) that was housed in a specially designed streamlined body. Consideration had to be given to designing a housing that was free of cavitation and minimized non-cavitating flow noise. Several factors were taken into account in selecting the position of the hydrophone, including its location in the wake and minimization of the effects of reverberation in the water tunnel. The hydrophone and its position relative to the disks in both facilities are shown in Figs. 15.51, 53 and 15.54. Some of the results are given in Arndt [15.15].

As a final example, a similar setup to that used in Higuchi et al. [15.135] was used to measure acoustic radiation from sheet cloud cavitation by Arndt and Levy [15.139]. The results are shown in Fig. 15.56. Note the difference in the frequency content compared to the spectra of surface pressure fluctuations shown in Fig. 15.45.

### Quantitative Laser Techniques for Cavitating and Bubbly Flows

Soon after the creation of the first laser at the Hughes Research Laboratory in May 1960 [15.140], the special properties of coherent light were being explored for flow measurement purposes. *Laser Doppler velocimetry (LDV)*, which matured in the 1970s and 1980s, and *particle image velocimetry (PIV)*, which came of age in the 1990s, are quantitative optical flow measurement techniques utilizing lasers.

The *LDV* technique [15.141], also known as *laser Doppler anemometry (LDA)* uses a small ellipsoidal measuring volume formed by crossing laser beams (the measuring volume is typically on the order of

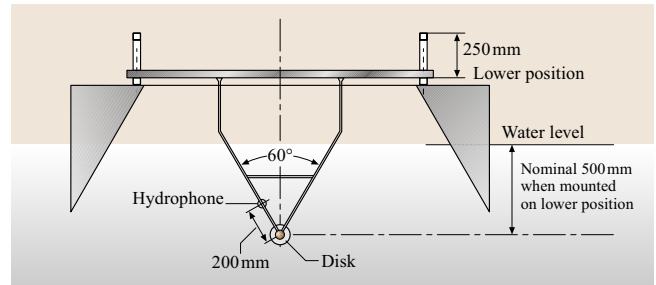


**Fig. 15.55** Vacutank installation for measuring inception noise [15.131]

$0.1 \times 0.1 \times 0.5$  mm, or smaller), in which the velocity of randomly arriving particles is measured at a point by the time (determined from Doppler burst frequency) it takes to travel a known distance (Doppler fringe spacing). A direct extension of *LDV* is *phase Doppler anemometry (PDA)*, which can be used to determine the bubble or particle size by measuring the phase shift of the illuminating beam with multiple receivers (initially two, now typically three, receivers), as well as bubble or particle velocity [15.142].

For the *PIV* technique [15.143, 144], a seeded flow field is illuminated (exposed) twice (or more) with a laser light sheet with a known separation time between laser pulses, and particle images are recorded [on film, a charge-coupled (*CCD*) or *CMOS* device]. If the recording medium is digital, the technique is referred to

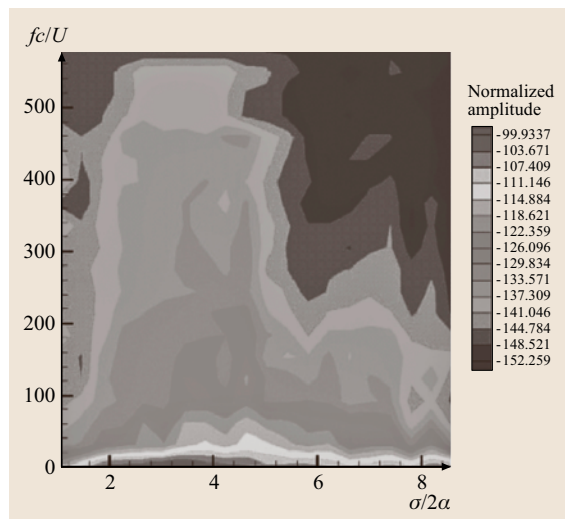


**Fig. 15.56** Acoustic spectra for the same hydrofoil shown in Fig. 15.19. Note the relatively high frequency content in the range  $2 \leq \sigma/2a \leq 6$

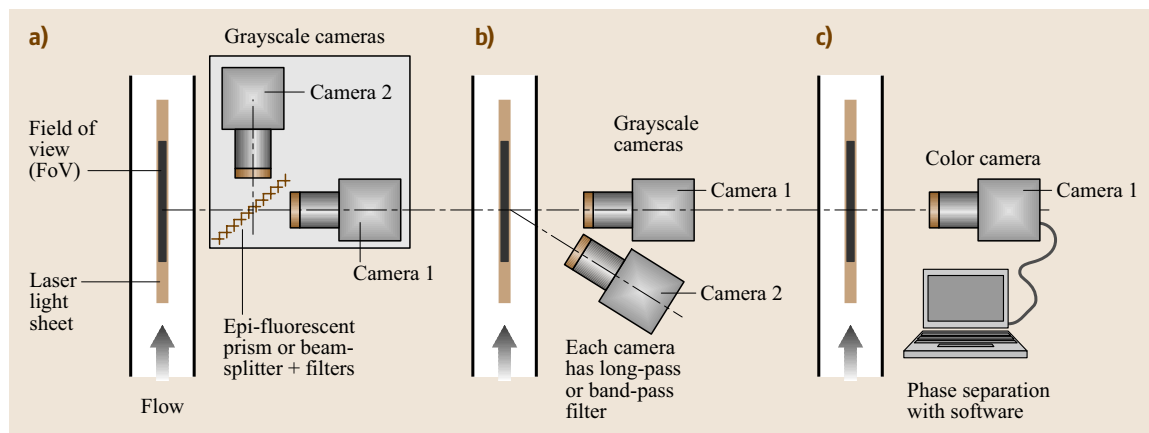


**Fig. 15.57** Typical PIV camera arrangements for phase separation by color

as digital PIV (DPIV)]. For intermediate particle concentrations statistical correlation-based methods can be used to determine the displacement in small interrogation areas, typically resulting in thousands of velocity vectors in a plane per captured image pair.

The fundamentals of these techniques, implementation details and recent advances (e.g., high-frame-rate PIV, holographic PIV, and micro-PIV, micro-LDV) are discussed in Chap. 5. Nowadays, complete LDV and PIV systems including software are commercially available from at least half a dozen vendors, and several free software packages for analysis exist. When used in cavitating or bubbly flows, these techniques face a special set of problems and challenges, which are addressed here.

### Particle Image Velocimetry

In a two-phase flow containing liquid and bubbles, the light from the laser sheet illuminating the object plane will be Mie-scattered by both the seeding particles and the bubbles. Typically the size of the seeding particles is one to tens of micrometers ( $\mu\text{m}$ ), whereas the bubbles caused either by vaporous/gaseous cavitation or artificial ventilation are much larger, typically tens to a few hundreds of micrometers. In order to measure velocity fields, the liquid and gas phase need to be effectively separated in the PIV images. Several methods to separate phases have been developed; they are summarized briefly below, and their applicability to cavitating flows is discussed.

**Phase Separation by Color through Laser-Induced Fluorescence.** In this technique the liquid phase is seeded with microscopic particles coated or imbedded with a fluorescent dye. The dye is chosen so that

the particles fluoresce at a wavelength (color) different from the incident light, e.g., in the yellow–orange range when illuminated with a green laser. Typical lasers currently used in PIV are frequency-doubled Nd:YAG (neodymium-doped yttrium aluminum garnet) lasers emitting light at 532 nm (green). Both phases will scatter the incident laser light, but only the liquid-phase seeding particles will fluoresce [laser-induced fluorescence (LIF)]. The liquid and gas (bubble) phases can now be separated in two ways: before image recording by using two synchronized grayscale cameras and color filters, or after image recording by using one color camera. If two grayscale PIV cameras are used, optical filters, e.g., long-pass filters (*long-pass* refers to the wavelength of the light; these filters are also called *low-pass* filters, referring to the frequency), and possibly a beam splitter or an epi-fluorescent prism are required. Some camera arrangements are shown in Fig. 15.57. In arrangement a,



**Fig. 15.58** Commercially available two-phase PIV camera mount (courtesy of Dantec Dynamics)



both grayscale cameras have the same field of view. An epi-fluorescent prism splits the beam, transmitting only the fluorescent wavelength to camera 2. Alternatively, a simple beam splitter in combination with a long-pass filter on camera 2 and an interference band-pass filter on camera 1 centered on the laser light wavelength can be used. In arrangement b, the two cameras have a different field of view, and a mapping function is required to *de-warp* the image of the off-axis camera 2. Long- and band-pass filters are also required to separate the phases. In arrangement c, a single color camera is used, and the phase separation is done after recording via software. Two-camera lens assemblies of this kind specifically designed for two-phase flow PIV/LIF have recently become commercially available (Fig. 15.58).

Phase separation by color was first successfully implemented by Sridhar et al. [15.145] in a cavitating jet facility while recording onto 35 mm color film. The experiment was conducted at very low, non-cavitating velocities (0.6 m/s) and 100  $\mu\text{m}$  bubbles were injected at very low gas void fractions for demonstration purposes.

A more complex version of phase separation by color was proposed by Towers et al. [15.146] for autocorrelation PIV (single frame, double pulse). Here one phase was also seeded with fluorescent particles, but multiwavelength illumination and recording was used to obtain separate, directionally resolved velocity vector fields for both phases of a two-phase flow via autocorrelation processing. Since most newer PIV cameras are capable of cross-correlation through frame-straddling (double frame, double pulse) one does not have to go to such complexity to avoid directional ambiguity anymore.

**Phase Separation by Particle Image Size.** Bubbles caused by vaporous/gaseous cavitation or artificial ventilation are typically one to two orders of magnitude larger than the seeding particles. For the photometric parameters of a typical PIV setup, the image size of a seeding particle with a diameter of one to tens of micrometers will be dominated by diffraction-limited imaging. When imaging bubbles with a diameter of hundreds of micrometers, the contribution of geometric optics to the effective particle diameter is one to two orders of magnitude larger than for the seeding particles, and the contribution of diffraction-limited imaging is also larger due to the smaller aperture (higher  $f\#$ ) required by high-intensity reflections from the bubbles. This will lead to different size diameters on the imaging medium, allowing phase separation by image size. For example, in the bubbly wake behind the closure region of a ventilated supercav-

ity, Fontecha [15.147] found the effective particle image diameters for 3  $\mu\text{m}$   $\text{TiO}_2$  seeding particles and 300  $\mu\text{m}$  bubbles to be one and six pixels, respectively.

The simplest way of separating the phases by particle image size is to threshold the grayscale PIV image, converting them to binary format: every pixel above a certain intensity value (the *threshold*) is set to 1, every pixel below is set to 0. Now regions of white (binary value 1) can be discriminated by size, identifying them as seeding particles or bubbles. This method was used by Hassan et al. [15.148, 149]. Hassan et al. [15.148] solved the problem of having a grey corona around bright bubbles by additional local thresholding. They determined that the optimal local thresholding function to properly outline bright bubbles was  $1/r^2$ , where  $r$  is the distance to the bubble center. Gui and Merzkirch [15.150] and Lindken et al. [15.151, 152] developed a digital masking technique to separate the differently sized particle images of the two phases. Determination of these masks also required pixel intensity thresholding and size discrimination.

**Phase Separation by Particle Image Intensity (Brightness).** Laser illumination and camera aperture (the photometric parameters) can be adjusted so that seeding particle images will not exceed a certain grayscale value. Pixels with higher grayscale values would then be associated with a bubble image. Sakakibara et al. [15.153] and Easson and Jakobsen [15.154] employed this difference in image brightness in two-phase flows where solids were the disperse phase and air was the carrier phase. This technique should in principle work well for bubbly liquid flows created by cavitation events, since the larger bubbles scatter (reflect) incident light at higher intensity than the seeding particles. A problem may arise if the intensities of the light scattered by the particles and by the bubbles are orders of magnitude apart, e.g., in sheet/cloud cavitation or ventilated flows, and cannot be simultaneously imaged onto a single camera (cf. discussion of practical aspects below).

**Other Phase-Separation Techniques.** Phase separation based on object image shape was used by Oakley et al. [15.155] for individual large bubbles, and for dispersed large, solid particles by Kiger and Pan [15.156]. Kiger and Pan [15.156] eliminated the seeding particles by using a spatial median filter (seeding particles are discarded as high-frequency noise; this only works for low concentrations of the dispersed phase). The seeding particle images can then be processed separately by subtracting the filtered images from the originals. Cor-

relation peak properties can be used for phase separation if there is a significant velocity difference between the two phases, as demonstrated in a bubble column by *Delnoij et al.* [15.157], albeit with prior knowledge of the liquid and gas velocities.

**Combined Techniques.** *Khalitov and Longmire* [15.158] developed a two-parameter phase discrimination by object image size and brightness. An object-weighted centroid vector (centroid position) is also determined and can later be used for particle tracking. A combination of phase separation by color and correlation peak widths applied to a bubbly jet in a box was reported by *Arnardottir* [15.159]. *Chaine and Nikitopoulos* [15.160] used a single color PIV camera in a dispersed, bubbly jet. Phases were separated after recording by evaluating the green and red channel separately, and additional filtering by intensity was used to eliminate interference from seeding particles and phantom bubbles.

Of all the techniques introduced above, it is expected that phase separation by color through laser-induced fluorescence using two grayscale cameras with filters will become the dominant PIV technique in cavitating flows in the intermediate term. The main advantage of this technique is that it allows the capture of bubbles of all sizes and that the PIV image for the carrier liquid phase is uncontaminated by the bubble phase. The main drawback is currently cost: two grayscale cameras are needed and suitable fluorescent particles can be very expensive.

**Practical Issues when Using PIV in Cavitating Flows.** All of the phase-separation techniques introduced above were developed in dilute bubbly liquid (or sometimes air/solid) flows. While they should in principle work for cavitating flows, additional difficulties arise, especially since bubbly flows resulting from cavitation can have much higher local void fractions, i. e., vapor pockets or bubble clustering. Some of the difficulties are:

- Cavitation bubbles are typically larger than seeding particles and will scatter light more effectively. Their images will appear much brighter (and larger) than seeding particles on the recording medium. This can cause a problem when using a single camera at higher void fractions, since the light scattered by the seeding particles may be too weak in comparison to the bubble reflections to produce a usable signal. The proper selection of seeding particles and the use of higher sensitivity (12-bit or higher) CCD cameras can somewhat compensate for this. For a primer on the scattering characteristics of particles, i. e.,

scattering cross-section and intensity of light scattered in the vicinity of 90° from the incident light sheet [15.161].

- Bubbles must be dispersed enough to provide usable particle images for cross-correlation. This may not be the case in the initial stages of cloud shedding in vaporous cavitation or in the vicinity of the closure region behind a ventilated cavity. If the void fraction is high, bubbles may cluster or coalesce.
- The illuminating laser light sheet may be attenuated if a large number of bubbles is present.
- A bubble illuminated with a laser light sheet may appear as two adjacent bright spots on the image plane [15.155, 160]. The brighter one is due to reflection, the dimmer one is due to refraction, then internal reflection, and refraction again. If the photometric parameters cannot be adjusted to avoid this, additional post-recording treatment becomes necessary.
- Seeding particles provide additional nucleation sites for cavitation inception. If water quality is critical to the cavitating flow being investigated, this may affect the results.

*Laberteaux and Ceccio* [15.162, 163] investigated partial cavities on two-dimensional wedges without and with spanwise variation and a NACA 0009 hydrofoil with PIV. The flow was seeded with fluorescent latex particles with an average diameter of 30 μm and individual double-pulsed images (with image shift to resolve directional ambiguity) were recorded onto single frames of 35 mm film through a filter blocking the laser light wavelength. Thus velocity vector fields of only the liquid phase around partial cavities were obtained. A high-speed, cinematographic multi-frame PIV system was also developed, which was able to record up to 10 000 frames/s, also filtered before recording. This system also employed double pulses onto a single frame, but with no image shifting for the second pulse, therefore it was only useful in situations where there was no flow reversal. The video PIV data was used to obtain phase-averaged velocity vector fields of only the liquid phase for flows with periodic cavitation cycles.

*Gopalan and Katz* [15.38] investigated the flow structure in the closure region of attached cavitation, and used phase discrimination by color, further developing the technique developed by *Sridhar et al.* [15.145]. One Kodak ES-4 four-megapixel digital camera was used and alternatively fitted with a long-pass or band-pass filter to measure the velocity in the water and bubble phases, respectively.

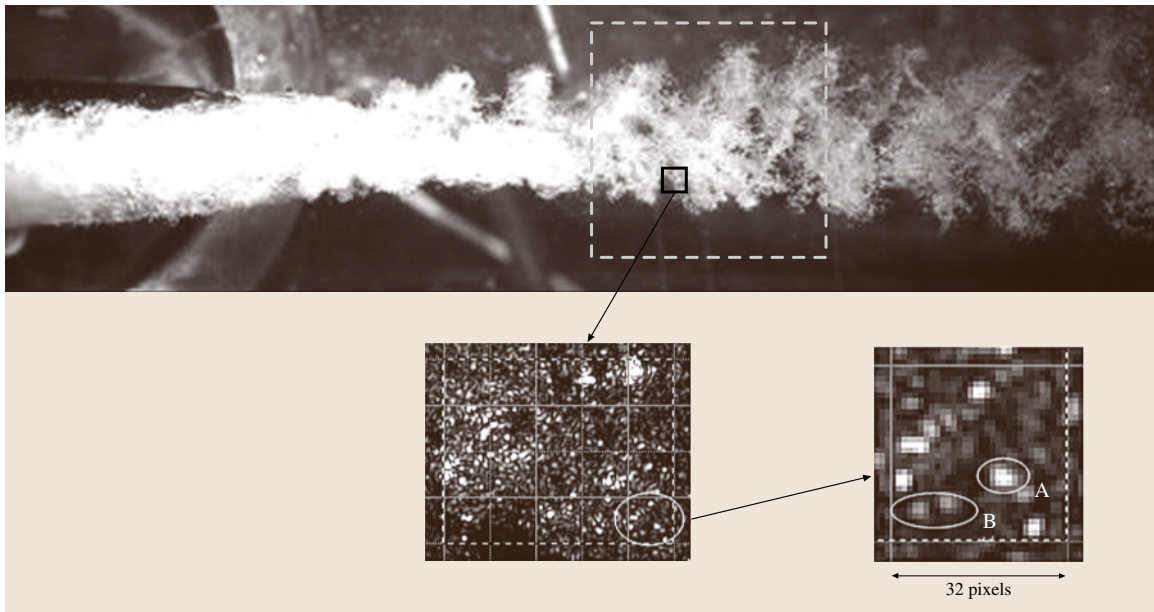


**Fig. 15.59** Bubbly wake resulting from the collapse of an axisymmetric, ventilated supercavity (Cavitator diameter  $d = 10$  mm,  $Re_d = 90\,000$ ,  $\sigma \approx 0.14$ , exposure time  $3\,\mu\text{s}$ ). The *dashed square* shows the approximate location of the **PIV** field of view. Bottom: Close-ups of a sample **PIV** image capture

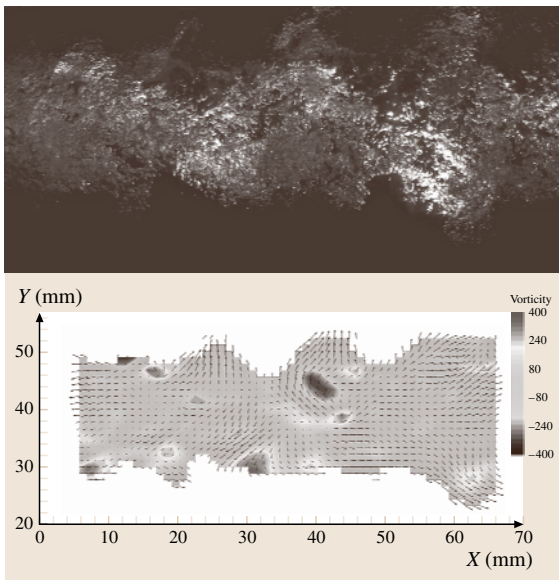


**Fig. 15.60** **PIV** in the bubbly wake resulting from collapse of axisymmetric, ventilated supercavity using a single camera ( $1024 \times 512$  pixel). *Top*: **PIV** image capture (one image of a pair). *Bottom*: bubble velocity vector field and vorticity contours computed from this image pair

Iyer and Ceccio [15.164] studied the influence of developed cavitation on the dynamics of a turbulent shear layer with planar **DPIV**. The flow was seeded with  $80\,\mu\text{m}$  fluorescent latex particles, and a long-pass filter was used to record onto a single four-megapixel digital camera. Thus vector fields for only the liquid phase were obtained, while also measuring the bubble void fraction.

When considering **PIV** measurements in larger research water tunnels, the large total water volume requiring seeding may make the use of expensive fluorescent particles impractical because of the high cost. In this case, other, inexpensive non-fluorescing seeding particles and photometric parameters should be chosen carefully to achieve simultaneous imaging of bubbly and liquid phases. Recent tests at SAFL have shown that hollow glass spheres (mean diameter  $11\,\mu\text{m}$ , density  $1100\,\text{kg/m}^3$ ), used as a non-conducting lightweight filler in the electronics industry or as paint additives, or silver-coated hollow glass spheres (mean diameter  $14\,\mu\text{m}$ , density  $400\text{--}900\,\text{kg/m}^3$ ), used as a conducting lightweight filler, may be used in vaporous cavitation. Discrimination by particle image size, particle image intensity or a combined technique can then be used to separate the phases. If the light scattered by the seeding particles is too weak compared to the bubble reflections

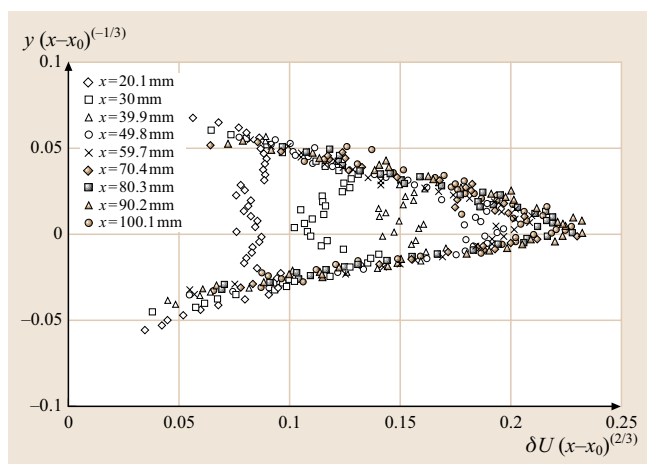


**Fig. 15.61** Bubble PIV velocity data in the closure region of an axisymmetric, ventilated supercavity (cavitator diameter  $d = 15$  mm,  $Re_d = 100\,000$ ,  $\sigma \approx 0.2$ ). Average of 800 captures

to register on the recording medium, the bubble velocity field itself can still be obtained with a standard PIV system, using the bubbles as *particles*.

This technique was used to obtain PIV velocity data in the bubbly wake of an axisymmetric, ventilated supercavity by Wosnik et al. [15.68, 165–167] and Fontecha [15.147]. A sample strobe-illuminated picture of this flow is shown in Fig. 15.59, including the approximate location of the PIV field of view and close-ups of a sample PIV image capture down to a  $32 \times 32$  pixel interrogation area. Standard PIV images were recorded from reflections of the air bubbles. The signal is usable for cross-correlation, as long as enough bubbles are present in the interrogation area. A sample PIV image capture and the corresponding velocity field from cross-correlation are shown in Fig. 15.60. Note that Figs. 15.59 and 15.60 show different realizations of this flow. Contrast and brightness of the PIV image were increased for reproduction purposes. The average percentage of validated velocity vectors pre-filtering will decrease significantly for the cavitating case (30–80% at the center of the bubbly wake) compared to the non-ventilated, non-cavitating single-phase case (> 95%) at the same Reynolds number, due to bubble reflection and refraction, varying bubble density, vapor pockets and bubble clusters. The number of validated vectors also drops off moving radially outward from the center of the wake. However, the bubble PIV data shows good quantitative results, Fig. 15.61 shows velocity data in the region immediately following cavity collapse. The bubble velocity data are seen to scale well with length and

velocity scales for the axisymmetric turbulent single-phase wake [15.168]. After cavity closure, the turbulent bubbly wake quickly rearranges itself into a similarity state, which in this case is achieved about four cavitator diameters downstream of the cavity closure (here the virtual origin was chosen at the point of cavity closure).

When computing velocity vector fields by cross-correlating bubble images, Fontecha [15.147] found the Hart algorithm to be more accurate and produce a larger number of valid vectors than the standard fast Fourier transform (FFT) algorithm. The Hart correlation method [15.169] identifies particles (bubbles) based on image intensity gradients, not just absolute intensity. It is thus well suited for varying intensity, relatively poor-quality PIV images of cavitation bubbles. PIV images that are slightly overexposed are often better suited for intensity gradient compression, since the saturated particle image centers have low gradients and will be discarded. Only the image regions with high intensity gradients are retained, and the remaining compressed, or *sparse*, image data results in a more efficient correlation algorithm. The Hart correlator also avoids the *intensity weighting* of the FFT correlation, where high-intensity pixels (particles) will contribute more to the cross-correlation than low-intensity pixels (particles). The compression rate must be chosen carefully to not lose correlation information.

### Phase-Locked PIV

For quantitative measurements in quasiperiodic cavitation processes it is often advantageous to obtain phase-locked or phase-averaged data. These data are especially useful for comparison with numerical results, where typically time-resolved information about cyclic events is available. When attempting to trigger a standard PIV system to obtain data phase-locked with cavitation events, the following problem can be encountered: pulsed Nd:YAG lasers tend to flash at a constant frequency, when triggered externally at unevenly spaced intervals the energy delivered per laser pulse may fluctuate significantly between flashes. A common work-around for this problem is to both record the signal documenting the quasiperiodic flow event (e.g., a pressure transducer on the suction side of a hydrofoil) and the TTL signal for PIV laser 1 and acquire a large number of image captures (typically thousands) at a constant laser pulsing frequency. The time stamp of each image capture can then be compared to the transducer signal, and the image captures can be binned according to their phase in the cyclic cavitation event. Obtaining phase-locked PIV data of cavitating flows is



further complicated by the fact that cavitation processes that may look quasiperiodic in two dimensions, e.g., sheet/cloud cavitation under certain conditions on certain foil shapes, are inherently three-dimensional and affected by the experimental configuration, e.g., the presence of walls. Preliminary studies with high-speed video and/or (phase-locked) photography to determine the feasibility of phase-locked or phase-averaged PIV are strongly suggested.

### High-Frame-Rate PIV

Most of the experimental work to date on cavitating flows has either been whole-field observational and qualitative, i.e., it consists of high-speed photography and/or video, or single-point quantitative, e.g., velocity measurements with a laser Doppler velocimeter (LDV) and/or bubble size measurements with a phase Doppler anemometer (PDA). More recently, whole-field, quantitative measurements have been made using particle image velocimetry (PIV) [15.67, 147, 165]. Unfortunately, standard PIV systems, while providing high-resolution, are limited to low repetition rates (on the order of several Hz). This is due on one hand to the low repetition rates of their components (typically, Nd:YAG lasers: 10–20 Hz, digital cameras: 15–30 frames/s), and on the other hand to dataflow bottlenecks inherent to the system design [cameras have no *onboard* memory, particle images have to be acquired through, e.g., the peripheral component interface (PCI) bus]. Standard PIV systems are therefore limited to instantaneous *snapshots* and statistical information, but can shed little light on the evolution of flow structures (occurring at inverse time scales up to several hundred Hz).

The first application of time-resolved particle image velocimetry in cavitation research was by Vogel and Lauterborn [15.170], who combined PIV and high-speed photography to investigate the flow around cavitation bubbles during their collapse near a solid boundary. With a drum camera designed for use in high-speed photography and an argon laser pulsed by an acousto-optical deflector, they were able to achieve a limited number of frames at a temporal resolution of 10 kHz.

In contrast, recently commercialized, high-repetition rate (*time-resolved*) PIV systems are capable of recording particle images at up to 2000 frames/s at full  $1024 \times 1024$  pixel resolution (or at higher framing rate and a reduced field of view: 4000 frames/s at  $1024 \times 512$  resolution, 8000 frames/s at  $1024 \times 256$ , etc.). Since two frames are necessary to obtain a velocity vector field by cross-correlation, the actual PIV recording frequency would be 1 kHz (2 kHz, 4 kHz, etc.). This is sufficient

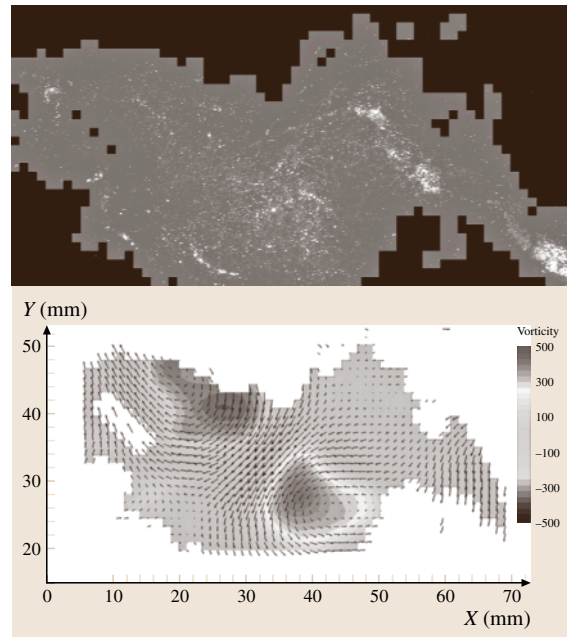


**Fig. 15.62** PIV in the wake of a cavitating NACA 0015 hydrofoil, angle of attack =  $-8^\circ$ , cavitation number = 1.1. *Top*: Adaptive processing mask obtained from sliding intensity thresholding overlaid on original image. *Bottom*: Velocity vectors and vorticity contours, from cross-correlation of bubbles

to temporally resolve cavitation events in most laboratory experiments. Typically, high-speed diode-pumped Nd:YLF lasers are used, which have dual heads and can achieve repetition rates of up to 10 kHz. The energy per pulse decreases with increasing frequency for these lasers, therefore a practical limit for most applications is set at about 5 kHz. An example of a currently commercially available high-speed Nd:YLF laser is the NewWave Research Pegasus, which delivers 10 mJ/pulse at its energy maximum near 2 kHz.

Figure 15.62 shows a sample frame from an experiment that quantitatively recorded the large-scale cavitating structures in the wake of a hydrofoil using high-speed, temporally resolved PIV [15.167]. With the given optical setup, flow speed and recording rate of 2000 Hz the mean flow traveled less than 5% of the field of view between captures, giving sufficient spatio-temporal resolution to track the large-scale cavitating vortices. The gas phase (cavitation) was separated with a simple, but effective adaptive masking algorithm based on a sliding intensity thresholding filter matched to the PIV interrogation spot size (left). Using bubbles as tracer particles,

the velocity vector field for the gas phase in the cavitation cloud is obtained from cross-correlation (right).

Time-resolved **PIV** experiments will provide researchers with a wealth of information typically only obtained from model-free, direct numerical simulation (**DNS**), but at Reynolds numbers not attainable by **DNS** in the near to intermediate future. Comparison with synchronized high-speed video will bridge the gap between the vast body of qualitative observations and quantitative methods. High-repetition-rate **PIV** will enable researchers to fully correlate numerical models with observed cavitation. This has tremendous potential for integrated experimental/numerical research on cavitating flows, since it can provide the crucial time-resolved quantitative information needed for numerical modeling efforts.

Laser Doppler Velocimetry

Even though the **LDV** technique has been used in fluid mechanics for more than 30 years, its applicability to bubbly gas–liquid flow is the subject of ongoing discussion. Several studies have shown what can be measured under certain, well-defined conditions, but the applica-

bility of **LDV** to real, practical two-phase flow situations is still being questioned. Generally speaking, the effect bubbles have on **LDV** measurements depends on their size and the volume fraction of the gas phase, as well as **LDV** parameters such as working distance and laser beam diameter.

In a high-void-fraction flow with *larger bubbles* (diameters larger than a few tenths of a millimeter) the **LDV** data rate will decrease compared to a single-phase liquid case. This is due to the lower probability of simultaneous beam penetration through the two-phase medium and the gaps in the signal when a bubble passes through the measurement volume itself [15.171, 172]. Distinguishing between the signal from the seeding particles in the liquid phase and the bubbles can be accomplished in certain cases for bubbly flow with larger bubbles. Methods include, phase discrimination on burst amplitude [15.173], phase discrimination on pedestal amplitude [15.174], controlling trigger level of signal intensity, liquid-phase seeding concentration [15.175], or a power-spectrum curve-fit procedure [15.176, 177]. In general, **LDV** in bubbly flow is feasible as long as the distances between the transmitting and receiving optics and the measuring volume are small enough to obtain useable Doppler signals from the liquid.

Bubbles resulting from cavitation events or remnants thereof, e.g., in the wake of sheet/cloud cavitation

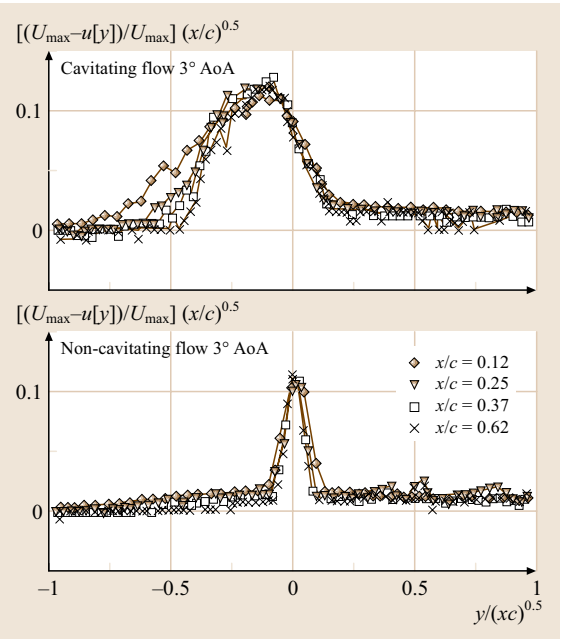


**Fig. 15.63** Mean velocity in wake of a 2-D **NACA** 0015 hydrofoil, **LDV** measurements with and without cavitation. Data are scaled in similarity variables for turbulent plane wakes. Coordinate  $x$  is the distance from the trailing edge,  $c$  is chord length [15.32]

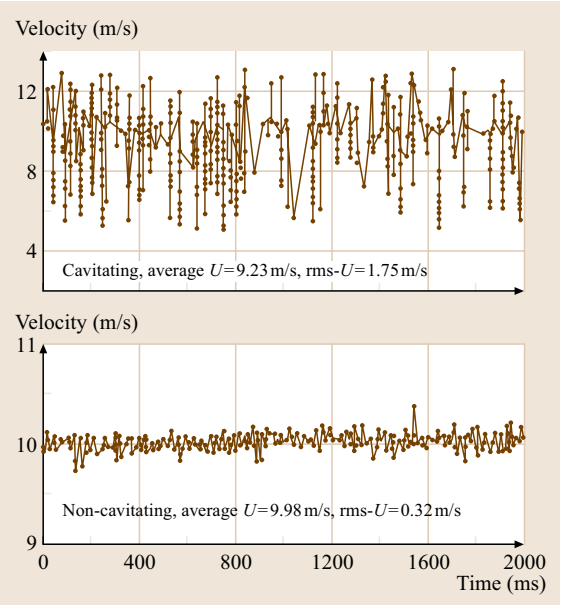


**Fig. 15.64** Velocity time series for cavitating and non-cavitating wakes (**LDV**)

(Fig. 15.12) typically have diameters on the order of a hundred micrometers or smaller and will act as additional seeding. As a result the LDV data rate of valid signals can increase significantly, especially compared to just using water impurities for *natural* seeding.

Kjeldsen et al. [15.32] found the LDV data rate for cavitating conditions in the wake of hydrofoils at small angle of attack to be more than 10 times higher than for non-cavitating conditions. The mean velocity data from LDV measurements with and without cavitation in the wake of a two-dimensional (2-D) NACA 0015 hydrofoil are shown in Fig. 15.63 [15.32]. The data are scaled in similarity variables for turbulent plane wakes. It is evident that the rate of spreading of the wake is much larger under cavitating conditions, which is consistent with visual observations and the results of other investigations [15.178]. Cloud cavitation sheds large vortical structures containing bubbles into the wake. These clouds of bubbles extend much further in the cross-stream direction than the viscous wake associated with non-cavitating flow. While the non-cavitating LDV signal resembles a typical turbulent wake signature, the cavitation signal is skewed towards lower velocities (Fig. 15.64). The bubbles are counted more efficiently than naturally occurring LDV seeds in the flow, therefore the average velocity will contain more weight from the shed bubbles. This effect on the LDV measurements still needs to be quantified. However, the observation that the wake spreading rate is much greater under cavitating conditions is still correct.

The strong negative fluctuations in velocity are due to the imprint left by the periodic passage of bubble clouds, and this cyclical increase in the data rate can be exploited further. The bubble shedding is rooted in a cyclic cavitation process on the foil surface, and is characteristic of the dynamics of the cavitating hydrofoil. Plotting LDV data rate versus time, where data rate is defined as the time elapsed between two acquired valid samples by the LDV system, fitting a curve that is spaced uniformly in time with the help of interpolation functions, and processing the result with an FFT algorithm, a power spectrum of the LDV data rate can be calculated. This LDV frequency-domain fingerprint is shown in Fig. 15.65. Note how closely it matches the power spectrum of close-to-simultaneous lift measurements. It should be emphasized that the LDV measurement is a quasi-point measurement, and will give important information of the cavitation shedding dynamics unmatched by a lift/drag balance and pressure transducers at the base of the foil, all of which will measure a global value. All these features also appear to be cap-

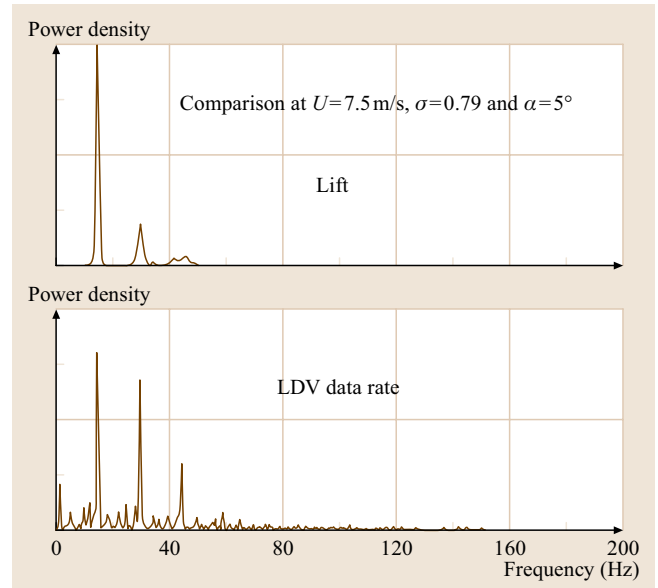


**Fig. 15.65** Comparison of lift dynamics with the FFT of the LDV data rate in the wake of a cavitating hydrofoil. The fundamental frequency corresponds to a Strouhal number of  $f_c/U = 0.15$

tured by numerical simulations [15.137]. By integrating numerical and experimental research, an approach toward calculating bubbly wakes of cavitating hydrofoils is emerging.

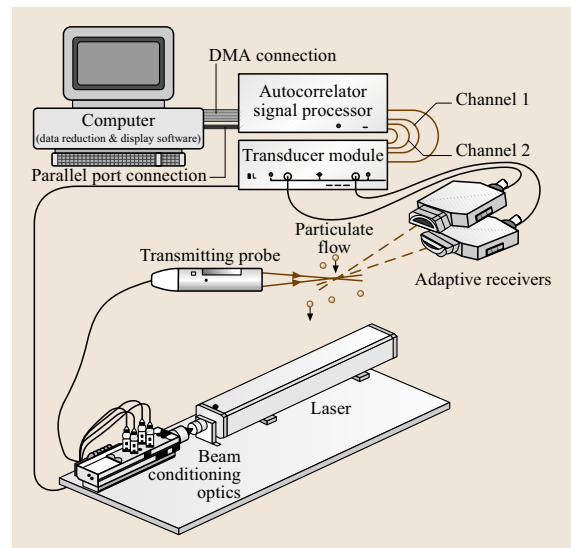


**Fig. 15.66** Typical setup of hardware of a commercial two-receiver PDA system

As previously mentioned, the phase Doppler anemometry (PDA) is an extension of the LDV measurement principle, and can be used to measure bubble velocity and size. As a bubble passes through the fringes of the probe volume, it scatters light. A receiving lens located at an off-axis collection angle projects a portion of the fringe pattern onto two or three detectors. Each detector produces a Doppler burst signal with a frequency proportional to the particle velocity. The phase shift between the Doppler burst signals from two different detectors is proportional to the size of the bubbles. For a sketch of the PDA principle and details of the PDA technique, see Chap. 21 or [15.142]. A typical two-receiver PDA setup is shown in Fig. 15.66 [15.179]. The size range of bubbles that can be measured is limited on one hand by the amount of light they scatter (a function of bubble size, available laser power, light collecting optics) and on the other hand by the Gaussian nature of the laser beam and the far-field condition. For a two-receiver system the measurable bubble diameter range is approximately 1–500  $\mu\text{m}$ , for a three-receiver system it is larger. Note that a two-receiver system is limited to measuring phase shifts of up to  $360^\circ$  without ambiguity. The bubble size range

can be extended by reducing the distance between the two receivers, however, this will also reduce the measurement resolution. A three-receiver system provides both a large measurable size range and high resolution. State-of-the-art PDA receivers have three prealigned receiving apertures integrated into a single fiber-optic probe. For a two-receiver PDA system the largest bubbles one is trying to measure should be smaller than the measuring volume, otherwise the two-receiver system cannot distinguish between reflection and refraction. The polarization vector of the illumination laser beam should be vertical ( $0^\circ$ ), since the main scattering mechanism for bubbles is reflection. Wang [15.118] reports PDA measurements in a high-speed water tunnel in the wake of a cavitating hydrofoil with a two-receiver system. Here the PDA receiver angle was set to  $90^\circ$  in order to avoid light path compensation due to the change of index of refraction in water, as shown in Fig. 15.67. Burdin et al. [15.180] used a three-receiver PDA to characterize the acoustic cavitation cloud caused by an ultrasonic horn at 20 kHz (vibratory apparatus, Sect. 15.1.4).

Several experimental studies aimed at understanding how bubbles modify the turbulence in the carrier

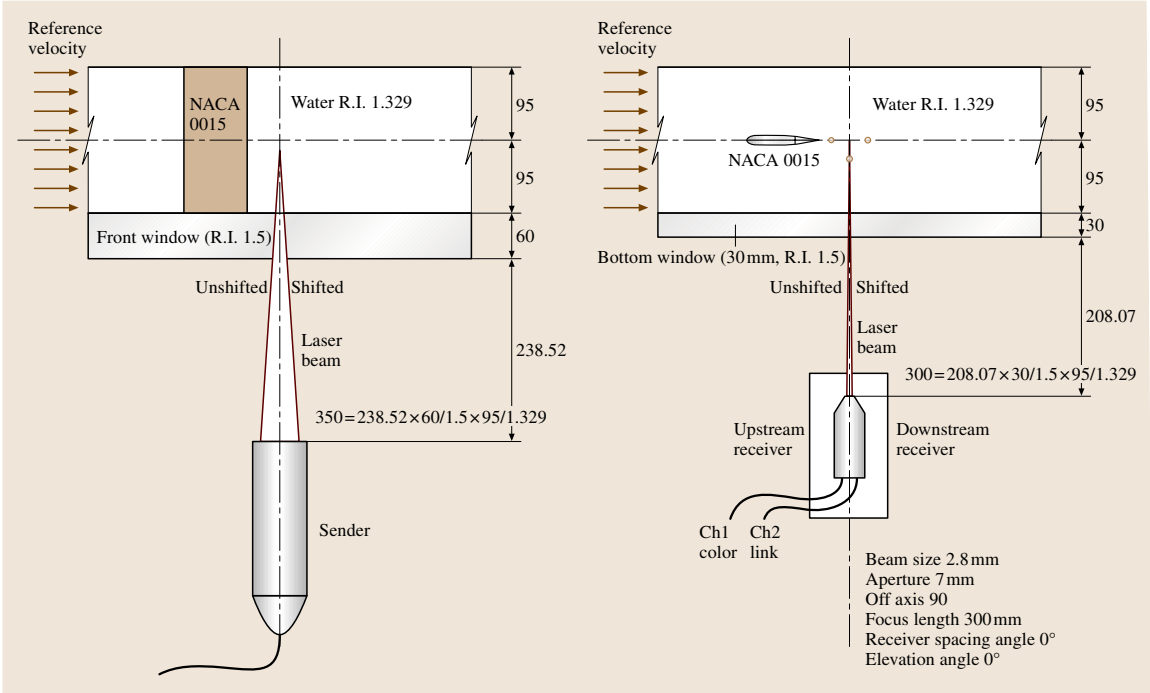


**Fig. 15.67** Cavitation bubble measurement in a hydrofoil wake with a two-receiver PDA in a water tunnel; the receiver angle is  $90^\circ$  [15.118]



phase in an axisymmetric liquid jet were carried out and provide good examples of **LDV/PDA** application to bubble–liquid two-phase flows. *Sun* [15.181–183] used **LDV** to measure mean and fluctuating velocity components in both the liquid and the gas phase in a bubbly jet ( $Re_{D,liquid} = 8500\text{--}9400$ ) with gas void fractions of up to 9%. For the continuous-phase measurements amplitude discrimination was used to discard signals from bubbles. Bubble sizes were approximately 1 mm, measured with a photographic technique. A surfactant was used to increase the surface tension and reduce bubble size and bubble coalescence. *Kumar et al.* [15.184] used **LDV** in a bubbly jet ( $Re_{D,liquid} = 4700\text{--}9100$ ) with gas void fractions as high as 20% at the lower Reynolds number. Bubble sizes were measured with a photographic technique and ranged from 0.6 to 2 mm. Only the liquid-phase velocities were measured. *Stanley* [15.185] and *Stanley and Nikitopoulos* [15.186] used a phase Doppler approach to measure liquid and bubble velocities and the bubble size distribution in the developing region of a bubbly jet.

### Void Fraction Measurements

Cavitating flows are two-phase flows, either single-fluid two-phase for vaporous cavitation or two-fluid two-phase for artificial, gas-ventilated cavitation or dissolved gas coming out of solution. An important quantity describing two-phase flows is the void fraction, usually defined as the gas volume to total volume. Similar to cavitation nuclei measurement, the instantaneous global void fraction can be determined in a very simple way with photography, by taking a picture of an illuminated

plane in the flow to determine bubble size and number. Multiple pictures can be used to obtain an estimate of average global void fraction. Advances in **CCD/CMOS** technology and image-processing techniques have recently created renewed interest in these non-intrusive photographic methods.

For cavitating flows, a continuous measurement of the local average void fraction is easily accessible by quasi-point-averaging or small-volume-averaging void fraction probes. Note that all sufficiently miniaturized local void fraction probes may be arranged in groups of two or more to give additional information on interface (bubble) velocity, and in certain cases bubble size in the previous section.

**Conductivity Probes.** All conductivity probes consist of two electrodes with a potential difference immersed in the two-phase mixture. Thus the current flow is a direct measurement of the conductivity of the fluid between the electrodes, which is determined by the relative amounts of liquid and vapor/gas. Current can then be calibrated as a function of void fraction. Since the conductivity probe is really a phase indicator and reacts to the passing of phase interfaces, void fraction is often more accurately referred to as *interfacial area concentration*. Conductivity probes were first proposed by *Neal and Bankoff* [15.188]. They have been used successfully for many years and a great variety of them exists, for a review of the many common ones see *Jones* [15.189]. A miniaturized four-sensor conductivity probe designed by *Kim et al.* [15.187] is shown in Fig. 15.68, note that the measurement area is less than  $0.2\text{ mm}^2$ .

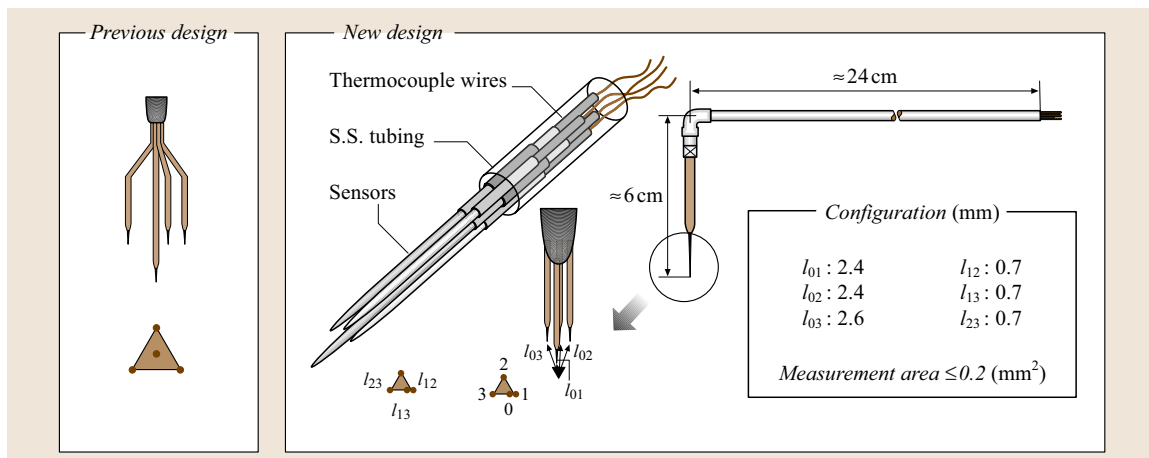


**Fig. 15.68** Schematics of an older and a new miniaturized four-sensor tubing conductivity probe for void fraction (interfacial area concentration) measurement [15.187]. (Note: S.S. = stainless steel)

**Optical Fiber Probes.** An optical probe is sensitive to the change in refractive index and thus also responds to the passage of a liquid–gas interface. If water is present at the tip of the probe most of the light will enter the water due to the relatively small difference in refractive index between the probe material (glass fiber) and water. If a gas bubble covers the probe tip most of the light is reflected back into the probe and can be detected on the other end using a photomultiplier. With a suitable sampling frequency and thresholding, the signal can be converted to a binary time series with binary states of liquid [ $b(t_i) = 0$ ] or bubble/gas [ $b(t_i) = 1$ ]. The local void fraction  $\eta$  is then simply the residence time of the gas state divided by total sampling time, or for equal sampling intervals  $\Delta t_s$ , the number of samples indicating gas state divided by total number of samples

$$\eta = \frac{\sum_{i=1}^N b(t_i)}{N} . \quad (15.26)$$

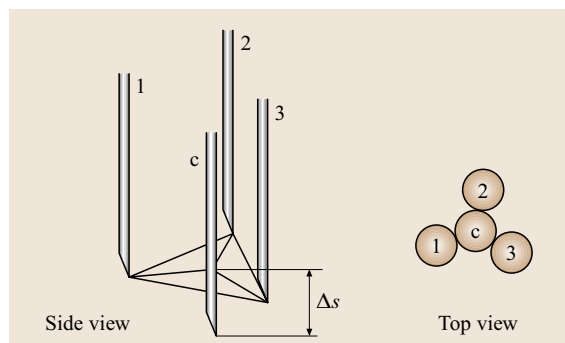


**Fig. 15.69** Schematic of an optical four-sensor probe [15.190]

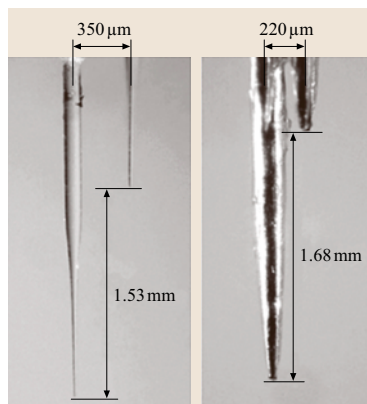


**Fig. 15.70**  
Dimensions  
of conductivity  
and optical  
void fraction  
probes [15.191]

*Mudde and Saito* [15.190] used an in-house fabricated optical glass fiber probe [15.192] to measure void fraction, bubble size and velocity in a bubble column and bubbly pipe flow. The design of the probe is shown in Fig. 15.69. The polymethyl meta acrylate fibers have a diameter of 0.2 mm and are the tips are cut at an angle of 30° to the fiber axis.

*Le Corre et al.* [15.191] compared a miniaturized four-sensor conductivity probe [15.187] and a miniaturized four-sensor optical probe (developed by the French Atomic Energy Commission – CEA, Grenoble) and showed that probe design greatly affects the accuracy of the measurements. To get an appreciation for the size of these probes, photographs are shown in Fig. 15.70. While probes miniaturized to this degree will work well in *conventional* two-phase flows, e.g., bubble columns, it is questionable how long a micrometer-sized fiber-optic probe would last under cavitating conditions with cavitation bubbles collapsing onto its tip.

**Grayscale Interpretation of PIV Images.** A new technique to determine void fraction from *PIV* measurements of a cavitating flow has recently been developed at SAFL [15.67, 165]. Regular *PIV* images were obtained in the wake of an axisymmetric, ventilated supercavity, using the ventilation gas bubbles as seeding *particles*. The average grayscale value for a series of raw *PIV* images was calculated, and the background noise was subtracted. Assuming that the intensity of the reflected light is proportional to the local void fraction, the general shape of the void fraction distribution versus radial position  $\eta^*(r)$  for any downstream location within the *PIV* field of view is known. However, the void fraction profiles are only qualitatively correct due to the fact that the light sheet was created by a Gaussian beam. The actual magnitude of the void fraction can be determined from the mass conservation integral for the gas phase

$$\dot{m} = \int_A k_1 \eta^*(r) \rho_{\text{gas}} U_{\text{gas}}(r) dA , \quad (15.27)$$

where  $\dot{m}$  is the ventilation gas injection rate measured with a flow meter (rotameter), and  $k_1$  is a correction factor for light sheet intensity variation due to the Gaussian beam. The ventilation gas density  $\rho_{\text{gas}}$  can be estimated from pressure measurements in the water tunnel and the ideal gas law. The velocity profiles of the gas phase  $U_{\text{gas}}(r)$  were determined from *PIV* cross-correlation algorithms using air bubbles as particles. The correction or *calibration* factor  $k_1$  can then be computed by numerically integrating equation (15.27), thus obtaining

the quantitatively correct average void fraction profiles from  $\eta = k_1 \eta^*$ .

An example of the void fraction obtained in this way is shown in Fig. 15.71. Note that the correction factor for the intensity variation of the light sheet,  $k_1$ , was assumed to be only a function of downstream position and independent of radial position  $r$ , i. e., the rays in the laser light sheet were approximated to be parallel.

**Other Void Fraction Techniques and Probes.** Several other techniques to determine void fraction exist. They include hot-film anemometry, which in principle has the advantage of also being able to measure phase-interface velocity. However, the fragility of hot-film probes limits their usefulness in cavitating flows. Gamma densitometers systems can be used to obtain line-averaged and cross-section-averaged void fraction. Both of these techniques were used successfully by Kirouac et al. [15.193] in a column filled with R-134a, simulating steam–water two-phase flow. Shamoun et al. [15.194] used a light extinction technique in bubbly flow. Analysis of how collimated, monochromatic light is scattered by a dispersion of gas bubbles provides direct measurement of the line average of the interfacial area density, which can be related to line-averaged void fraction by an image-processing algorithm. Note that the local average void fraction can also be determined from phase Doppler (PDA, laser diffraction) measurements described pre-

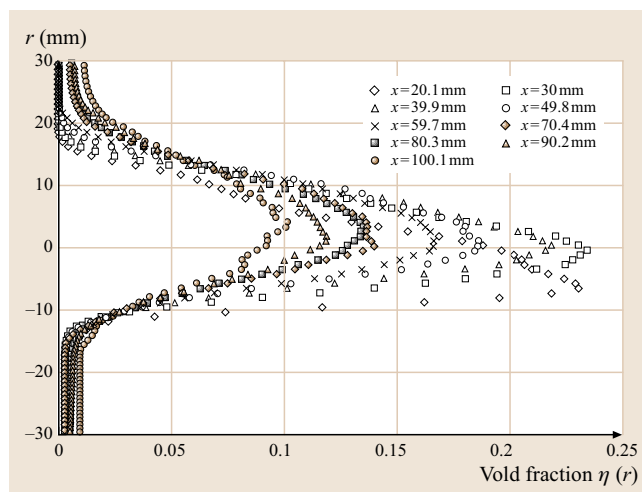


**Fig. 15.71** Void fraction calculated from PIV images, in a turbulent bubbly wake immediately behind the collapse of a ventilated supercavity.  $Re_d = 10^6$ ,  $\sigma \approx 0.2$ . Average of 800 vector fields

viously [15.195]. Three additional techniques for void fraction measurement (and bubble sizing) used primarily in oceanic environments are high-frequency backscatter measured with multiple- and single-frequency sonar, acoustical resonators and acoustic pulse propagation sensors. These have been compared to conductivity probes by Vagle and Farmer [15.196].

## 15.2 Wave Height and Slope

In this section surface elevation and slope measurements in time and space are discussed along with their complementary frequency-domain counterparts amplitude/energy and phase spectra. The discussion is divided into four subsections, each of which is subdivided into subtopics. The main subsections are: temporal point measurements at fixed geometric position; one-dimensional spatial measurements (measurements along a line); two-dimensional spatial measurements (measurements throughout an area); and special surface elevation measurements for large laboratory or field use. As several techniques described in each of the first three categories use similar physical principles, there will be some repetition in the discussion as the number of dimensions is increased.

This section is not a review paper in that it does not present all relevant references or give a complete histor-

ical perspective for each measurement method. Rather, it is written in the tradition of a handbook, as a guide for experimentalists. Therefore, general discussions of the appropriate measuring techniques are presented with sufficient references to clarify the basic principles of the methods. For more details on a particular topic, the reader should consult the entire open literature; the references cited herein can be used as a starting point for this process.

One last note, radar measurements have not been included in these discussions, although they are certainly valuable in the field. This decision was the result of the difficulty encountered in conducting radar measurements in the laboratory due to reflections, re-reflections, and such. For field measurements and large-scale experiments, these techniques afford endless possibilities and should not be discarded.

### 15.2.1 Temporal Point Measurements at Fixed Geometric Positions

If one could travel back in time, one would see that the first wave height measurements were made in the field eons ago by mariners and beach-goers who estimated this quantity for their logs as well as for fun. This first method for estimation of wave height is by direct physical observation and suffers from individual bias and the inability to estimate length (as well as time to determine wave period). To demonstrate the variability with which individuals estimate wave climate in the nearshore, one of the authors (MP) conducted an experiment at Duck, North Carolina while at the Coastal Engineering Research Center [15.197]. This report documents a confidence interval of  $\pm 0.23$  m on wave heights that varied roughly over 0.30–1.0 m during the experiment. One can easily see that estimating wave height is nontrivial, and this technique can be dismissed summarily.

Perhaps the simplest measurement that does not incorporate an electronic instrument is the wave staff, possibly coupled with an imaging system. Early systems used single-frame film cameras or film movie cameras that offered time series rather than single snapshots. More recently, of course, film cameras have been supplanted by video/digital imaging of various types. In this most basic technique, the wave staff was usually the equivalent of a survey rod – a straight, long rod with tick marks inscribed along its length. In the laboratory, where positioning of the rod is more straightforward (i.e., from the ceiling, walls, floors, etc.), this simple method provides reasonably good results. Problems include the disturbance due to the in situ nature of the staff, the resolution of the imaging device, which may be marginal especially if a large dynamic range is required, and the labor-intensive data-reduction process needed to determine the time series of surface elevations. (Sev-

eral other instruments that provide direct output of the surface elevation time series and that are still reasonably inexpensive will be discussed below.) One important advantage of the primitive wave staff used in conjunction with video is that, in the case of breaking waves, where other more-sophisticated instruments such as those discussed below give questionable results, one can observe the phenomenon directly and glean useful information not otherwise available [15.198]. Lastly, it is noted that in the laboratory one can utilize a grid along a channel wall, for example, to obtain spatial information in addition to temporal data.

In addition to the prosaic wave staff described above, many authors ascribe this name to more-advanced instruments such as the capacitance wave probe and the resistance wave probe, likely the most frequently used instruments for measuring liquid surface elevation at a prescribed location in a wave basin, flume, or tank. These instruments were first introduced in the late 1940s and 1950s [15.199–201]. In fact, their popularity is such that they are available commercially. Note that they are often used in arrays, linear or 2-D, to provide spatial information, as discussed in the following subsections. In the capacitance probe, an insulated single wire is oriented vertically through the liquid and extended into the air, thus forming one side of a capacitor, while the water comprises the other. For a fixed probe the capacitance varies with changes in water level. The insulation can be a glass tube in which a non-insulated wire is placed or it can be Teflon, for example. Some conductivity of the liquid (usually water) is required, and is generally present naturally due to impurities. Conversely, in the resistance probe, two non-insulated wires are mounted vertically, parallel and adjacent to one another, and the resistance between them varies as the liquid/water level changes. In principle, both of these instruments exhibit essentially linear electrical response.

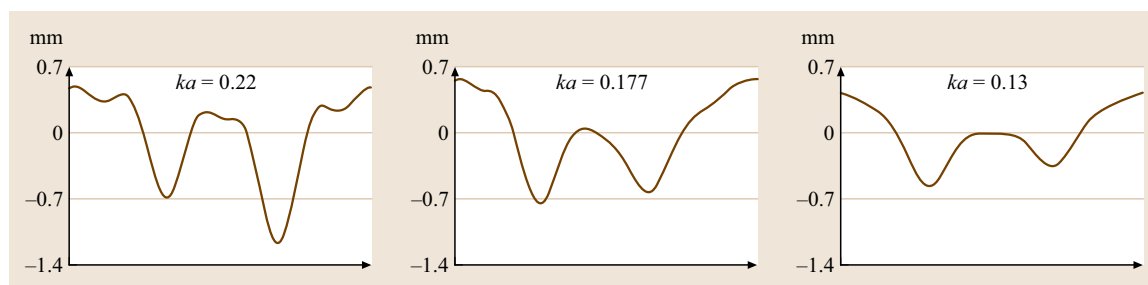


**Fig. 15.72** A 9.8 Hz wave time series (Wilton's first ripple) measured at three downstream locations from the wave generator with steepness (wavenumber times stroke) 0.146. The ordinate spans 2.1 mm while the abscissa represents one wave period, 0.102 s (courtesy of Phys. Fluids)



For a discussion of their use in physical models, see for example *Hughes* [15.202].

In practice, resistance and capacitance gages have some differences and many similarities. The resistance gage is more robust and hence is frequently used in oceanic applications while the capacitance probe is more fragile and hence is more often used in laboratory investigations. Capacitance gages require simpler circuitry and, for multiple spatial measurements, their crosstalk interference is lower than that of resistance gages [15.203]. In addition, capacitance gages typically offer less blockage of the flow, as a stiff insulator can be used, thus removing the need for a strut of some sort. Electronics that cover a sufficiently large frequency range are available commercially; however, it is apparent that liquid receding from the probe may limit the accuracy of the measurements especially, for low frequencies and larger amplitudes or for high-frequency and relatively small-amplitude conditions. For gravity–capillary and capillary waves where wave heights are small (i.e., on the order of millimeters) the meniscus effects on the intrusive wires can be significant [15.204], and these instruments should be avoided, or at least the smallest-diameter wire possible should be used, and again capacitance gages are the better choice. For an indication of the accuracy that can be achieved see Fig. 15.72 [15.205] where gravity–capillary waves in the internal resonance regime are shown; the capacitance wave probe diameter was 0.5 mm. Using either of these probe types is problematic in breaking waves where multivalued surface profiles and bubbly flows are found. In fact, this latter statement is true for any in situ probe, and more-advanced imaging techniques are required.

Pressure measurements via some type of transducer are another common method of measuring wave height indirectly as a function of time at a fixed spatial position. In this method, a pressure sensor mounted at a fixed depth below the mean free surface is used to measure the fluctuations in pressure induced by the passage of the wave, and theory is used to relate the pressure fluctuations to the surface elevations. Though highly accurate pressure measurement devices now exist, several related problems arise. First, the transducer sensing area in common with the fluid is of finite size and therefore yields spatially averaged readings that may be problematic for short wavelengths. Second, since the transducer's diaphragm/interface with the fluid necessarily displaces to provide the measurement, sensor–flow interactions occur that may affect the measurement. These two errors may not be a major problem for field measurements, but can hamper measurements on small scales in the lab-

oratory. Last, since the general surface/interfacial wave theory problem remains unsolved in closed form, there is a level of approximation that accompanies this method and significant errors may arise depending on the wave steepness and surface complexity. A primary advantage of this measurement is its less-intrusive nature – it does not pierce the water surface and so does not affect the flow there. The seminal work in this area appeared in the literature in the mid 1940s by researchers at the Scripps Institution of Oceanography [15.206] and the University of California [15.207]. Obviously, present-day pressure transducers (e.g., those using quartz or fiber optics) are much more accurate, but still suffer from most of the pitfalls mentioned.

Yet another class of point measurement techniques uses sound to probe the surface elevation, usually from below. Perhaps the simplest example is the echo sounder in which a short-duration sound pulse is emitted vertically from below and the measured time of flight for the wave to travel to the surface and return to the sensor, traveling at an estimated sound speed in water, yields the surface height once the factor of two is taken into account. One such commercially available sensor is the acoustic surface tracker (Nortek, USA). These types of gages have several positive features as well as some disadvantages. As with the pressure transducer, these techniques are remote, do not pierce the surface, and can yield reasonable measurements; however, when used from below, they may suffer from many shortcomings, including the relatively high power required to generate the highly attenuated high-frequency acoustic waves necessary to maintain a small-cone-angle interrogation beam and thus a small surface footprint; data-processing problems associated with the extraneous reflection and re-reflection from surfaces other than the one that is to be measured; and difficulties when measuring steep surface slopes. Individual echo sounders are not commonly used in practice to measure surface elevations. However, two present-day reincarnations of this technique are the upward-looking acoustic Doppler current profiler (ADCP), which is capable of measuring depth-varying currents and thus inferring surface elevation via water wave theory, possibly including propagation direction [15.208], and side-scan and upward-looking sonar, which can measure orbital velocities (from which one can again construct the surface via a wave theory) and the sea surface spectrum [15.209]. Both of these instruments emit sound bursts and measure the Doppler shift in the sound waves reflected from particles found naturally in the water. In *Strong et al.* [15.208], the authors discuss the use of the ADCP in obtaining wave

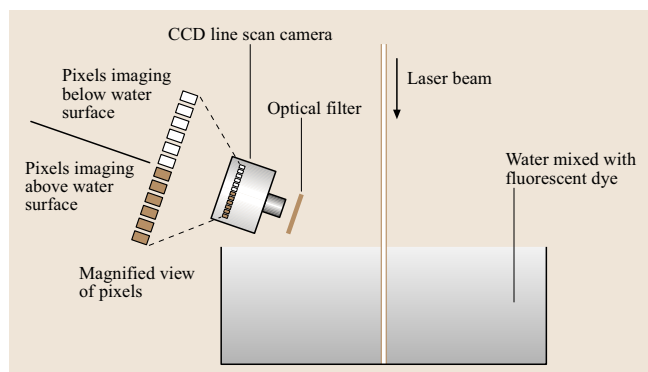


**Fig. 15.73** Laser wave height gage. The optical filter blocks specular reflections of the laser light but passes the light from the fluorescing dye. (After Liu and Lin [15.210])

height spectra, including directional information. The authors show reasonable agreement with both a gage that measures pressure and two components of horizontal current (PUV, discussed in Sect. 15.2.4 along with the ADCP) and a heave-pitch-roll (HPR) buoy (discussed below and in Sect. 15.2.4). These acoustic devices can be used in large laboratories, although they were developed primarily for use in the field. In the data analysis, cross-spectra are obtained that include amplitude and phase information as a function of direction; hence wave height is available for a complicated sea surface. These instru-

ments provide much more information than the others discussed thus far, but they are expensive, a wave theory must be invoked and an inversion performed, scatterers must be present over the water depth, and bubbles present due to strong winds or breaking in extreme seas may dominate the return and affect the results. For small-scale laboratory efforts, these instruments are probably not a good choice. The aforementioned side-scan sonar technique uses a somewhat comparable approach.

Major improvements in measuring surface elevations in the laboratory can be attributed directly to the advent of lasers. Using lasers to view and probe the surface, to obtain two-dimensional velocity fields, obtain three-component velocities over a small volume, and facilitate other research has increased steadily in popularity, and for good reason. These essentially non-intrusive devices in conjunction with viewing and forming optics are extremely effective and have proven to be the system of choice and the state of the art. Throughout this section on wave height measurement, the use of the laser is highlighted. The first laser-based device discussed herein is essentially a laser-based wave staff [15.210,211]. The laser beam is oriented vertically and originates from above the water surface. A camera, in this case one with as little as a single line of pixels, in an elevation view records the intersection of the laser beam and the water surface with a small look-down angle from the horizontal and with the line of pixels aligned with the laser beam (Fig. 15.73). The water is mixed with a fluorescent dye whose spectral excitation peak overlaps the wavelength of light produced by the laser. (Often fluorescein dye is chosen for green-blue laser lines over rhodamine dyes as the former affects surface tension less and is safer to use.) A long-wavelength-pass optical cutoff filter is placed in front of the camera lens to remove specular reflections/refractions of the laser beam from the water surface while passing the light from the fluorescing dye. Each line of pixel data captured by the camera is processed to determine the pixel closest to the transition from the low light levels above the water surface to the high light levels at and below the water surface. By recording an image of an object with known distance markings (i. e., a precise target), a calibration is determined and the pixel location of the transition from air to water is converted to elevation. Limits on accuracy concern the diameter of the laser beam and the angle of inclination of the camera relative to the horizontal, with smaller-diameter beams and shallower angles yielding more-accurate results, see the discussion of laser light sheet methods in Sect. 15.2.2. Though the measurement is more accurate at shallower viewing angles, the inter-

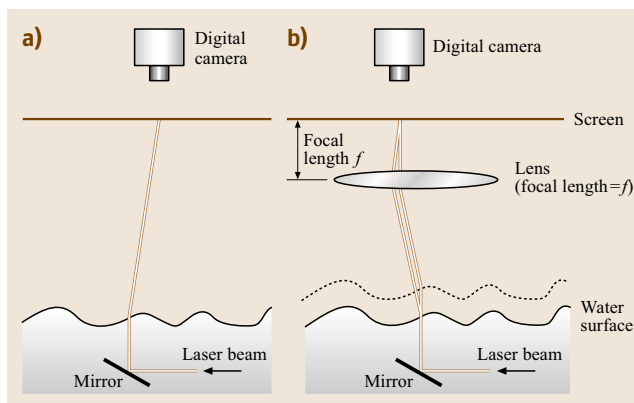


**Fig. 15.74a,b** Laser slope gage. (a) The height between the water surface and the screen must be large compared to the wave height so that the position of the beam on the screen can be converted directly to the water surface slope. (b) Because the screen is placed one focal length above the lens, the position of the refracted beam on the screen depends only on the angle of inclination of the laser beam relative to vertical. The trajectories of the beam with two water surface elevations are shown

section of the laser beam and the water surface may not be visible to the camera when the surface shape is highly three dimensional, as in breaking waves.

In another relatively simple method using a laser beam, the temporal variation of the free-surface slope is measured. Slope methods are particularly useful for measuring capillary waves where, though the amplitudes are quite small, the slopes may be large. In this method, the laser beam is oriented vertically from above (or below) and the direction of the beam after refraction through the interface is measured and related to the local surface slope in two directions. Perhaps the simplest method of measuring the direction of the refracted beam is to fix a translucent screen horizontally in the air with the laser beam directed vertically from below the water surface, and to view the beam position on the screen with a video imager from above the screen. A simple setup is shown in Fig. 15.74a. As can be seen in the figure, the position of the beam in the imager (once calibrated by imaging a target of known size or a precise grid) can be converted to the angle of the beam relative to the vertical if the height of the screen and the instantaneous height of the water surface are known. The difficulty of knowing the water elevation is overcome approximately if the vertical distance between the water surface and the screen is much larger than the wave height. Also, as shown in Fig. 15.74b, a lens can be placed between the screen and the water surface with the screen at the focal plane of the lens. In this case, all beams with the same slope relative to the vertical, regardless of the water surface height, will be focused at the same point on the screen. Likewise, the spot on an opaque screen can be viewed from below, though the correction may be more difficult. If one is interested in obtaining the surface height record from the measured surface slope, one can integrate the slope record if the surface height at some reference time and the wave phase speed are known. The phase speed is a theoretically well-known quantity in a linear monochromatic sea; however, in a physical experiment, problems arise computing this value accurately (even for monochromatic waves) because the phase speed is a function of the wave height for finite-amplitude waves and the wave height is, of course, not known. One of the first investigators to use this technique to measure surface slope was Cox [15.212], though at that time he used a pin-hole in a telescope to focus the light on a photocell, and an incandescent light source rather than a laser. Other problems Cox experienced included elevation effects on the light intensity. Sturm and Sorrell [15.204] presented findings using a similar approach. In their

work, they identified a limiting slope that can be measured due to total internal reflection of the laser light, and they avoided the problem of not knowing the surface elevation by requiring the distance of the screen (in their case a photo cell) to the water surface to be much larger than the wave height. In addition, they invoked linear wave theory and used monochromatic waves of low steepness to demonstrate the effectiveness of the method, and under those restrictions, the method works well. It is noted that this technique also has a footprint (the beam waist at the water surface) that for shorter wavelengths may affect the data significantly. Lastly, Saylor [15.213] is mentioned as an investigator who used total internal reflection to advantage for measuring the surface slope beneath capillary waves of large steepness.

The literature on surface slope measurement using lasers is voluminous, and as mentioned previously, it is not explored adequately here as this is not the purpose of this handbook. A discussion of several additional techniques is included in the two subsequent subsections, however. Extensions of these methods to obtain additional information are also possible. Using light reflection from the water surface, Wu et al. [15.214] developed a technique that enabled the measurement of surface curvature distribution concurrent with surface slope in one surface direction, and with it they measured laboratory-generated wind waves. Subsequently, Wu [15.215] further enhanced and generalized the technique to facilitate measurements in both surface directions. Barter et al. [15.216] discuss a method that measures surface slope and surface elevation simultaneously, the latter by measurements of the attenuation of the beam. This seems difficult to implement accurately due to water clarity issues. Lastly, we mention the contribution by Jahne et al. [15.217] that discusses the use of a telecentric imaging system to facilitate simultaneous measurements of the optical slope and surface elevation at the same geometric point on the surface. This novel technique greatly improves surface measurement capabilities at the expense of a more-complex system.

One additional point worth mentioning with regard to laser point measurements is whether the laser should be oriented propagating from liquid to gas, or gas to liquid. Jahne et al. [15.218] present an argument on the grounds of sensitivity and range that it is better to have the laser beam originating in the air and entering the water from above. We feel that the direction decision should be based on more-practical considerations; in particular the steepness of the waves to be measured plays an important role.

Buoy- or float-mounted accelerometers (or inclinometers) with onboard compasses represent yet another type of surface elevation measuring device. Typically, these are station-moored so that their degrees of freedom are limited. One popular version of this is the heave-pitch-roll buoy that measures the three degrees of freedom that comprise its name. (Two similar instruments that have been developed to obtain directional spectra and are discussed subsequently are the PUV gage and the differential pressure gage.) This method is a point measurement of surface elevation when heave acceleration only is recorded or available, and is known generally by the generic name *waverider* buoy. This instrument, of course, has several deficiencies that include motions other than heave due to imperfect mooring, and the fact that it is a floating body and thus exhibits its own dynamics. Although gyroscopic accelerometers can and are used, they have response times that affect the accuracy of these instruments, and waveriders are less accurate in very steep wave conditions where accelerations are large. These packages are very popular for nearshore measurement and are readily available commercially. Due to their deficiencies, they are not recommended for most laboratory uses.

One of the first to investigate a so-called proximity probe, in this case through the air to the liquid surface was *Killen* [15.220]. This instrument used sound; however, since then proximity probes that use other sources have been developed. Advantages include their essentially non-intrusive nature and hence their transportability; they can be moved easily along the surface (for example in towing tank experiments) or held stationary without affecting the liquid surface. Typically, their disadvantages are that the error increases as the slope increases, that standoff distance is an issue, and that they may have a large *footprint* on the surface so that the elevation obtained no longer approaches a point measurement. Though useful in measuring liquid surfaces, these instruments are extremely popular for use in measuring solid surfaces. In addition, several variations of these instruments are available commercially, and they can be used for longer wavelengths in the laboratory.

To conclude this subsection, a few simple ideas of other types of probes are mentioned. For example, if one uses fluorescing dyes dissolved in the liquid/water to make it nearly opaque (and one is not concerned with surface tension, perhaps due to longer wavelengths being investigated), a simple column of illuminated light-emitting diodes (LEDs) oriented vertically can be used as a wave staff by video recording the column over time and later counting the number of diodes that are

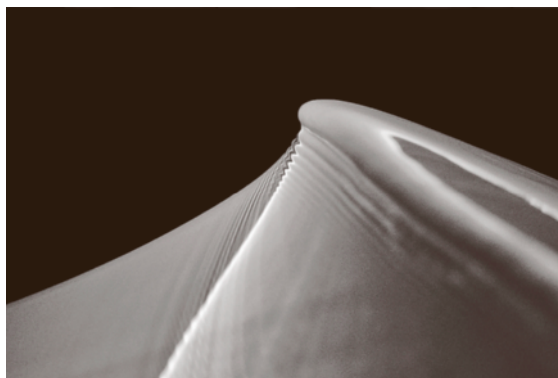


**Fig. 15.75** Laser-induced-fluorescence photograph of a gravity wave that is about to form a weak spilling breaker from *Liu and Duncan* [15.219]. The wavy line forming the boundary between the dark upper region and the lower, orange region is the intersection of the laser light sheet and the water surface. Light variations in the bright region of the image are due to refraction of the light sheet as it enters the water and due to refraction along the line of sight of the camera as it views the radiant nonuniform light sheet through the curved water surface between the camera and the light sheet

visible in the image. Also with this nearly opaque fluorescent dye-laden liquid, another possibility is to use laser light from above, and view the single spot with two imagers with known geometric position in space, and use stereo pairs to obtain the spot's location. This technique is discussed for an instrument with multiple laser beams in Sect. 15.2.3. Finally, another technique discussed below that can be used also for point measurements, is the laser line-scan imaging method.

### 15.2.2 One-Dimensional Spatial Measurements

In many instances, one is interested in knowing the wave/surface shape along a horizontal line. The temporal history of this shape can be used for a variety of purposes, including the determination of the wavelength, the dispersion relationship for water waves, and the spatiotemporal power spectrum. Perhaps the simplest method to obtain this height distribution is to arrange an array of wire gages in a straight line, see for example *Mitsuyasu* [15.221] and *Wang and Hwang* [15.222]. The method is, of course, limited by the length of the array, which determines the longest wavelength that can be measured, and the spacing of the wire gages within it, which determines the shortest wavelength that can



be measured. It is a useful and robust method that can be implemented especially in the field, as described in Wang and Huang [15.222].

Laser-based measurement methods are particularly well suited to one-dimensional spatial measurements. One obvious method is, of course, to use an array of laser wave staffs in the same manner as an array of wire gages. However, rather than employ the laser method as a discrete set of wave staffs, the laser beam is usually expanded optically into a light sheet and an area-based video camera views (from the side with a small angle from the horizontal) the fluorescence induced at the air–water interface by the light sheet. In a typical application, the laser beam is spread into a sheet either by using cylindrical lenses or by a rotating polygonal block with mirrored surfaces. The light source is usually mounted above the water surface to maximize the intensity of the laser light and thus the light emitted by the dye at the water surface. In the camera images, the region corresponding to the air is dark while the region corresponding to the water is bright (Fig. 15.75). The boundary between the dark upper region and the light lower region is the water surface profile formed by its intersection with the light sheet. At the time of this writing, most measurements of this type utilize digital still or movie imagers rather than film cameras. Temporal resolution is limited by the maximum frame rate of the camera and the brightness of the image incident on the camera’s sensor, which in turn is determined by the laser power, the width and thickness of the light sheet, the lens number  $f$ , and the concentration and light conversion efficiency of the dye. If the light sheet is created with a rotating mirror, the scan rate of the rotating mirror must be set to include several laser beam scans in each image exposure to insure uniform lighting. Spatial resolution is limited by the number of pixels imaging a given distance in the plane of the light sheet and several optical effects. One optical effect is the combination of the thickness of the light sheet and the viewing angle of the camera. As the light sheet becomes thicker or the camera look-down angle increases (with zero defined as horizontal) the thickness of the light sheet on the flat water surface as seen in the camera image increases and the change in image light intensity across the light sheet–water surface intersection is reduced. This weaker light-intensity gradient decreases the clarity of the apparent water surface in the image and thus reduces the accuracy of its measured location. Another limitation is blockage effects produced by wave features interrupting the line of sight from the camera to the light sheet–water surface intersection, or due to the shading of parts

of the water surface by other fractions of the water surface. As mentioned in the above discussion of laser wave staffs, these blockage effects only become unavoidable in highly three-dimensional surfaces such as during energetic wave breaking. Since the ratio of surface height to length rarely exceeds about  $1/7$ , typical imagers, which have about the same number of pixels vertically and horizontally, are poorly utilized with say a wavelength distributed over the full width of the image but the height distributed over only a seventh of the image height. *Perlin* et al. [15.223] used a system of cylindrical lenses to stretch the wave height in the image so that it extended over additional pixels, thus increasing the vertical resolution without modifying the horizontal resolution.

In principle, the single-point laser slope gage can be adapted to measure one-dimensional spatial distributions of slope by scanning the beam at a high rate in a plane perpendicular to the water surface and measuring the deflection of the beam by the methods described in the previous section. However, these scanning laser slope gage methods have been reserved primarily for two-dimensional spatial measurements of slope and are discussed in the following section.

### 15.2.3 Two-Dimensional Spatial Measurements

Techniques for measuring two-dimensional spatial distributions of water surface height suffer from limited accuracy in the vertical direction and/or limited resolution in the plane of the mean water surface. The most rudimentary of these methods is simply a two-dimensional array of point measurement devices and the most straightforward of these is an array of wire gages. Each gage has the accuracy of an individual wire gage, but only a limited number of gages can be placed in a given area of the water surface. A method using essentially an array of laser wave staff devices has been developed by *Carneal* et al. [15.224]. The device used a  $10 \times 10$  array of low-power laser diodes that point toward the surface from above with a small angle relative to the vertical. The intersection of these laser beams and the water surface (the water is mixed with a high concentration of fluorescent dye) was observed with a single digital camera that had a  $1000 \times 1000$  pixel array. The camera viewed the water surface from a relatively small angle from vertical, on the opposite side of the vertical from the direction of the laser beams. The image positions of the illuminated points at the intersection of the laser beams and the water surface are used (through calibration) to determine the three-dimensional positions of

these points on the water surface, thus providing a discrete representation of the water surface at each instant in time. This relatively new method has similarities to stereo methods discussed below. Its accuracy, particularly in height, is determined essentially by the number of pixels that the beam–water surface intersection points move due to the maximum change in surface height. Thus, its accuracy in the vertical is much lower than the single laser wave staff where the water surface varies over the entire column of pixels. Similar to the wire gage array, this method provides data at only a discrete set of points within the measurement area. In spite of these difficulties, this method is non-intrusive and thus well suited to a number of applications where the use of wire gages would be difficult or impossible.

Another interesting method for determining the spatial distribution of surface height is stereo photography. In this method, two cameras separated by a distance  $d$  (or a single camera with a split-screen stereo lens) view the water surface from above. The images from the two cameras are recorded simultaneously and the overlapping parts of the images are analyzed to obtain the surface height distribution. To maximize the region of image overlap, the cameras are typically pointed toward the same portion of the water surface. In stereo analysis, the position of a physical feature in three-dimensional space is determined from the relative change in position of that physical feature between the two images. The primary shortcoming of stereo measurements of water surfaces is that the image features used for analysis are typically reflections, say illuminated regions of high water surface slope or curvature, rather than physical objects. Thus, the three-dimensional position of the reflection point on the free surface may be different for each camera because of their different viewing angles. This introduces errors in the stereo analysis and the calculated distribution of surface height. This method has been used by *Banner et al.* [15.225] and is discussed by *Jahne et al.* [15.218]. Recently, *Wanek and Wu* [15.226] have developed a three-camera system oriented at an oblique angle to the water surface and performed a thorough evaluation of the method by comparison with simultaneous capacitance wire gage measurements. *Grant et al.* [15.227] also developed a stereo method; however, rather than use reflections from the water surface as points for stereo analysis, they marked points on the surface with a  $10 \times 10$  array of laser beams created with a holographic lenslet array acting on the beam of a single pulsed Nd:YAG frequency-doubled laser. The intersection of the beams with the water surface was viewed with a split-view stereo camera. No fluorescent dye was used; rather the

intersections of the beams and the water surface were made visible by scattering from naturally occurring solid particles in the water. The images were processed to obtain the three-dimensional (3-D) positions of the beam intersection points with the free surface. Of course, as in the multi-laser-beam single-camera method discussed in the previous paragraph, the spatial resolution is limited by the number of laser beams and the vertical resolution by the number of pixels of image displacement between the two images of the same physical feature.

Another optical wave-height method uses moiré fringes. A moiré projection method is described by *Grant et al.* [15.228]. In this method, light is projected on the water surface through a rectilinear grating. The water is mixed with fluorescent dye and the projected light pattern, which is distorted by the shape of the free surface, is viewed through a camera with an identical grating at the focal point of its lens. Fringes created by the interference of the two grids are then counted to find the surface height along each fringe contour. This method is not trivial to implement and its accuracy in height and resolution in the horizontal is limited by the number of fringes in the image. However, it too can be useful when non-intrusive methods are required.

Techniques for measurement of surface slope throughout an area of the free surface are used extensively in the laboratory and the field. The slope imaging methods described in the following paragraph are the current state of the art and provide highly accurate slope measurements with high spatial resolution in the measurement area. Before considering these slope imaging methods, the scanning laser slope gage is discussed. This instrument is capable of obtaining the spatiotemporal spectrum of the water surface slope over a small surface area and has been used by a number of researchers in both the laboratory and the field. The principles of these devices are essentially the same as the laser point slope gage described above; however, in the scanning devices the beam is traversed at a rapid rate over a rectangle or circle on the mean water surface. Typically the laser beam projects upward from below the water surface and a system of rotating or oscillating mirrors and lenses in a submersible housing is used to traverse the beam over the area of interest while keeping the beam trajectory vertical. The receiver optics are placed above the surface. As in the point slope gage, a lens with a diffuser screen placed above and at its focal plane results in a direct calibration of beam position to surface slope without knowing the instantaneous surface height at the point where the beam passes through the water surface. The position of the beam on the diffuser screen

is tracked with a photosensitive position sensor or even a high-speed digital camera. Such a device was developed by *Bock and Hara* [15.229]; it scanned a circle of diameter 154 mm every 14.4 ms with 237 slope readings per revolution (a spacing between readings of 2.04 mm). A similar device described by *Li et al.* [15.230] scanned an 81 mm × 81 mm square pattern with 36 × 36 measurement points every 146 ms. These scanning rates and distances between samples determine the frequency and wavenumber limits of the spectra produced. Another critical parameter, as in any laser slope gage, is the diameter of the beam at the water surface. As the surface wavelength approaches this diameter the instantaneous slope measurement becomes inaccurate.

Slope imaging methods based on reflection and refraction have become a common technique for laboratory measurements in recent years. These methods are capable of measuring time sequences of the surface slope distribution throughout an area of the surface. Unlike the scanning slope methods, slopes are measured simultaneously at each pixel in the image covering the measurement area allowing one to obtain the temporal evolution of the slope field with high spatial and

temporal resolution. The appropriate theory has been reviewed by *Jahne et al.* [15.218]. In the present article, only the refraction methods are described since they have been used most often and since the principles of the two types of devices are similar. In the refraction methods, a light source with spatially varying intensity or color is placed underwater at a depth such that its presence does not significantly affect the waves. A still or movie camera is placed above the water surface. The principles for this refraction method were first introduced by *Cox* [15.212], though he used an optical sensor to measure the slope at only one point. Lighting systems with spatially varying white-light intensity can be used to measure one component of surface slope over a two-dimensional patch of the surface. One such system was developed by *Jahne and Riemer* [15.231] in which the light source (a modification of the device developed by *Keller and Gotwols* [15.232]) consisted of a glass box filled with a suspension of latex particles in water (Fig. 15.76a). The light was provided by a row of lamps directed horizontally at one end of the box. The light scattering caused by the particles creates an exponentially decaying light intensity in the direction of the

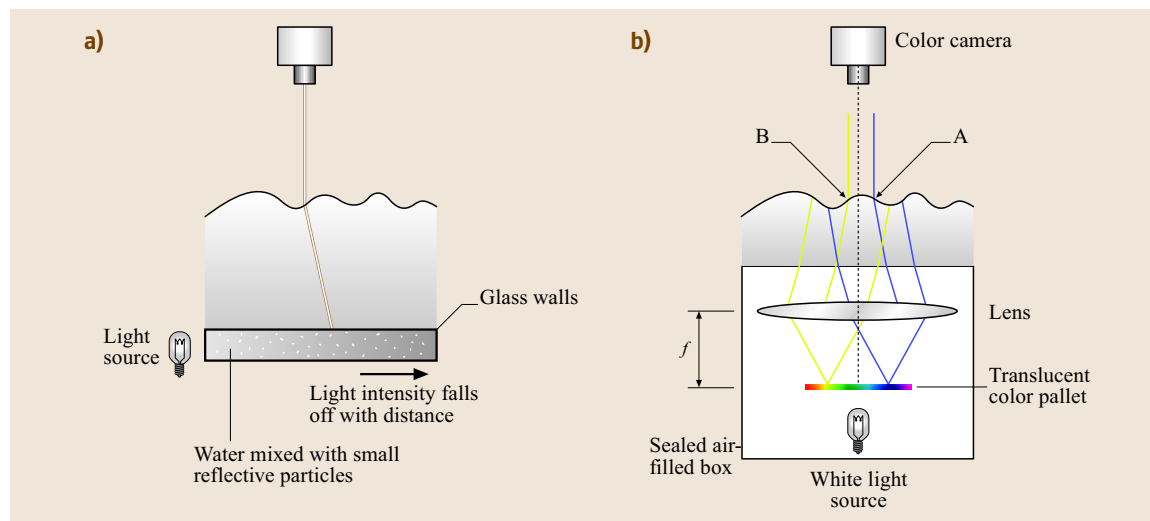


**Fig. 15.76a,b** Schematics of slope imaging devices. **(a)** System for measuring one component of slope (after the devices reported in *Jahne and Riemer* [15.231] and *Keller and Gotwols* [15.232]). The light box at the bottom of the schematic produces white light whose intensity varies with position in the plane of the page along the upper surface of the box. The light intensity is constant in the direction normal to the page. The camera is placed far above the water surface so that it receives only the vertical light rays. **(b)** System for measuring two components of slope (after the device reported in *Zhang and Cox* [15.233]). The lighting system produces beams of light that approach the water surface with continuously varying angle and a different color for each angle. The blue and yellow beams are shown in the figure. The point A (B) on the water surface has a slope such that it turns a light ray from the blue (yellow) beam to the vertical. The camera is placed far above the water surface so that it receives only the vertical light rays

light projection (say the downwind direction in a wind wave tank) and a uniform light intensity in the cross-wind direction. Each elemental area of the water surface receives light rays from a wide range of points from the light box, and as each of these light rays passes through the surface it is bent away from the local surface normal by refraction. Typically, the camera is placed a large distance above the tank (i. e., a distance many times the maximum wave height) so that it receives only the light rays that are nearly vertical. Thus, tracing the light ray backward from the camera, each pixel images a small area of the water surface. At the water surface, this light ray is turned toward the local surface normal and is directed to a specific point on the surface of the light box. The light intensity received at the pixel is determined by the intensity at the corresponding point on the light box, thus encoding surface slope by light intensity. With this white-light box, only the slope component in the direction of the light gradient can be determined. Of course, both components of slope can be determined in sequential experiments by rotating the direction of the light gradient  $90^\circ$  about a vertical axis. This can also be facilitated by using separate sets of lamps on two perpendicular sides of the box in separate experiments.

This slope imaging method can be extended to simultaneous measurement of both components of surface slope by using a light source with spatially varying color and a color-sensitive camera, *Zhang and Cox* [15.233] and *Zhang, Dabiri and Gharib* [15.234]. The system used by *Zhang and Cox* [15.233] is depicted in Fig. 15.76b. The light source apparatus consists of lamps creating an upward-projecting cone of white light, a horizontal translucent screen with a color pattern, and a large-diameter lens with its axis oriented vertically and the lens placed one focal length above the screen. It is essential that each point on the screen have a different color. Since the screen is at the focal point of the lens, all light rays from any point on the screen leave the lens in a parallel beam whose direction from the vertical is determined by the position of the point on the screen relative to the vertical optical axis of the lens. Each point on the water surface is illuminated by all the different beams with direction encoded by color. According to the local slope, only one of these beams is deflected vertically. The camera is then placed high above the water surface and the pixel corresponding to a given point on the water surface receives the vertical ray whose color is then an encoded measure of the local slope. Both the gray-level and color versions of these slope imaging devices produce a wealth of spatiotemporal information about the surface slope field and are being used primar-

ily to explore the physics of wind wave systems in both the laboratory and the field.

### 15.2.4 Special Surface Elevation Measurements for Large Laboratory or Field Use

In many cases, wave height records, particularly those measured in irregular or random seas, are expressed on a spatiotemporal frequency-by-frequency basis (i. e., in the temporal frequency and spatial frequency/wavenumber domain) via Fourier transform techniques. By Fourier transforming a time series and/or an instantaneous surface profile, one obtains a complex representation of the amplitude/energy and phase, or equivalently the real and imaginary parts of the wave frequency or wavenumber. These spectra are useful for the study of the physics of water waves for many practical scenarios (for example, the determination of a transfer function to convert sea-surface elevation spectra to roll spectra in a linear systems approach for an offshore platform design), and, most importantly for the discussion at hand. That is, to properly utilize and analyze the data recorded by PUV gages (which measure the pressure and two horizontal components of velocity, hence the acronym), ADCPs, and such, the amplitude and phase spectra (a frequency-by-frequency representation of the linear superposition of waves in the record) are required. As the topic of this handbook is experimental fluid mechanics, it is not our purpose to present these data analysis techniques here. Instead, the interested reader is referred to the many excellent texts that discuss the Fourier transformation process for surface waves as well as for any other temporal series and/or spatial information. As a starting point, the texts by *Bendat and Piersol* [15.235] and *Papoulis* [15.236] are recommended, though many other outstanding texts are available. Specific to the area of water waves, texts by *Ochi* [15.237, 238] are available, again among myriad others.

The focus of this subsection is to identify some of the instrumentation available to obtain data in large laboratory settings that more closely resemble the field. Instruments discussed include: those that provide a time series of pressure and the two horizontal components of velocity concurrently (i. e., PUV gages and variations thereof) which may be transformed to yield surface height frequency spectra with directional information; slope array buoys that can be used to determine surface height frequency spectra in time and space (i. e., wavenumber magnitude, wave frequency, and direction); ADCP devices; global positioning system (GPS) signals that may



be used to obtain surface height spectra; and multi-point/grid surface height measurements by wave staff that can be used to approximate the amplitude and phase as a function of wavenumber vector, wave frequency, and direction. The techniques and algorithms that determine the various types of spectra from temporal and spatial series are continuing to evolve, as are the methods used in the laboratory and field to obtain the data series.

The first class of instrumentation to be discussed measures several of the dependent variables of linear (inviscid) wave theory at one location; from these data reconstruction of the *directional* temporal frequency spectrum is possible. Of course all these methods have drawbacks regarding the approximations required and these drawback result in differences between the computed and actual spectra. Perhaps the most fundamental approximation, as mentioned above, is the use of linear wave theory to obtain the spectra. As an example of such a ubiquitous recorder, the **PUV** wave gage can be used to calculate the directional frequency spectrum, say  $S_{\eta\eta}(\omega, \theta)$  at a horizontal location (where  $\eta$  is the surface height,  $\omega$  is the angular frequency, and  $\theta$  is the wave propagation direction); here we neglect the phase spectrum, as is customary. **PUV** hardware units and their attendant analysis software are available commercially and may be used as standalone or shore-wired devices. Pressure is typically measured with a quartz pressure transducer while the two components of velocity are measured via an electromagnetic current sensor (e.g., those manufactured by Marsh–McBirney) or an acoustic current sensor (e.g., those manufactured by Falmouth Scientific). Both current sensors yield measurements averaged over a spatial volume on the order of  $1\text{ cm}^3$ . Knowing the mass density, the mean of the measured pressure yields the sensor depth required by the wave theory. These instruments provide the information required to obtain the first three components of a Fourier expansion in *direction* (i. e., with amplitude and phase). Variations of these instruments are the **UVW** (three components of velocity) gage, the heave–pitch–roll (**HPR**) buoy actually developed earlier, and the differential pressure gage [15.239]. A typical **PUV**-type gage utilizes an expansion to obtain the wave propagation direction based on the seminal work by *Longuet-Higgins*, *Cartwright*, and *Smith* [15.240] in which an **HPR** buoy was investigated. In their formulation, auto- and cross-spectra of surface elevation, and surface slope in each of the two directions were used to obtain expressions for the first five coefficients of the real-valued Fourier-expansion approximation to the directional spread (for a complex representation, amplitude and phase, the first

three coefficients are thus available). More recently differential global positioning system (**GPS**) technology has been used to measure buoy motions and shown to be equivalent [15.241]. Essentially the same expansion is used for the various gages mentioned, though different Fourier directional coefficients result. In fact if one measures pressures at other positions locally in space, additional terms in the expansion are available providing presumably improved estimates of the directional temporal frequency spectrum.

At the cost of a more-expensive instrument than those discussed hitherto, the acoustic Doppler current profiler (**ADCP**) is well suited for obtaining the directional surface elevation spectrum as well as the water-particle velocity spectra in discrete bins over the water depth. Typically these units include a pressure transducer to obtain mean depth and tidal information, and were originally developed to obtain the current profile as a function of depth. For a complete description of one such commercially available product see the information from RD Instruments [15.242]. As a current profiler the instrument works as follows: four acoustic beams are paired in orthogonal planes at fixed orientation with respect to the vertical (typically  $20^\circ$  or  $30^\circ$ ), known as a Janus configuration. The beam-axis component of velocity is measured and cell-averaged. The cell mean current is obtained by subtracting the measured velocities of the opposite beams. Using a cross-correlation under the assumption of stationary wave fields, the directional spectrum may be determined, though a larger computational effort is required than if simply using them for current profiling. One important advantage of the **ADCP** compared to the **PUV**-type devices discussed previously is its ability to determine velocity profiles to the surface. As the orbital velocities beneath waves decay exponentially in intermediate and deep water over vertical distances scaled with the wavelength and since the instrument is necessarily positioned below the main orbital motion, the ability to measure currents to the surface facilitates quantifying the higher-frequency part of the spectrum. Obviously these instruments along with the **PUV**-type are useful in field operations where hazardous ice flows exist, or perhaps seaway traffic is high. In the laboratory, for example in a large, deep basin where a model is to be used, these instruments may provide the additional advantage that they can be bottom-mounted and no longer represent a surface obstacle.

In concluding this subsection, one possible novel technique on the horizon is that of using **GPS** signal reflections, see *Zuffada* et al. [15.243]. They discuss the possibility of measuring sea height and surface rough-

ness with global positioning system reflections from the sea surface. A review of the literature at this juncture in-

dicates that this technique is still under development and that the associated difficulties remain largely unresolved.

## 15.3 Sediment Transport Measurements

### 15.3.1 A Brief Introduction to Sediment Transport

Sediment transport is a broad subject with many intricacies. Many books have been written about sediment transport [15.244, 245], and the reader is encouraged to explore these books for more detail on this complex subject. Nevertheless, a brief discussion about some of the basics of sediment transport is warranted herein to help clarify some of the issues surrounding measurements associated with sediment transport.

Sediment transport measurements are difficult for a number of reasons:

- Natural sediment is opaque, making optical penetration difficult.
- Sediment transport is strongly dependent on flow properties, and instrument intrusion can be a problem, especially near the bed.
- Most sediment transport occurs in complex physical environments, such as near bed forms and boundaries.

Sediment transport is extremely important in fluvial, oceanic, and Aeolian (wind-blown) geomorphology. For the sake of brevity, waterborne sediment transport will be the focus of discussion herein. Even so, many of the methods described can also be applied (perhaps in slightly different forms) to Aeolian sediments.

Traditionally, sediment transport has been subdivided into three components: bed load, suspended load, and wash load. Bed load is the mass flux of sediment particles that travel along the bed by rolling, bouncing, and sliding. Flow drag pushes the particles along the bed, and momentum exchange between the particles and the bed is often significant. Bed load is extremely difficult to measure accurately, and while new, innovative techniques have been proposed, none have proven effective. The primary problem is that bed load travels in a thin layer in the part of the flow with the strongest velocity gradient. Thus, it is difficult to accurately measure the velocity and number of all mobile particles that make up the bed load.

Suspended load consists of sediment that is entrained into the flow by turbulence. Sediment suspensions are not true suspensions, but consist of particles that settle

out of the flow in the absence of turbulence. Suspended particles have a finite fall velocity. What distinguishes bed load from suspended load is that suspended particles may travel many grain diameters from the bed, and do not come into contact with the bed as frequently as bed load particles. Like bed load, the suspended sediment concentration at the interface between the bed and the water is generally very important and also very difficult to measure accurately [15.246], but for the most part, suspended load is less difficult to measure than bed load.

Wash load consists of very fine sediment particles that do not easily settle once they are entrained into the flow, even in the absence of turbulence. The wash load is nearly a true suspension. Because of this, wash load particles are finer than particles found in the bed. Since wash load particles are fine, they are usually also cohesive. We will limit our discussion of the theory of suspended sediment primarily to noncohesive sediment because, while cohesive sediment is very important, it is also very complicated. Many of the suspended load measurement techniques described in this chapter can be applied to wash load sediment measurements. However, there are issues associated with particle breakdown and flocculation that must be considered, and in situ measurements of cohesive sediment are often preferable [15.247].

### Suspended Load Transport

The ultimate goal of sediment transport work is often to determine rates of erosion and/or deposition of sediment. In order to find either of these quantities mass flow rate of sediment must be measured. To demonstrate the importance of sediment mass flux for suspensions of fine sand, we begin with the mass conservation equation

$$\frac{\partial c}{\partial t} + \frac{\partial F_{si}}{\partial x_i} = 0, \quad (15.28)$$

in which  $c$  is sediment concentration,  $t$  is time,  $x_i$  represents the three principle coordinate directions, and  $F_{si}$  is the flux of suspended sediment in the  $i$ -th direction. For fine sediment with a terminal fall velocity  $v_s$  the flux can be written as:

$$F_{si} = (u_i - v_s \delta_{i3}) c, \quad (15.29)$$

where  $u_i$  is the flow velocity and the third principle direction is in the vertical. Essentially, (15.28) and (15.29)

state that suspended sediment follows the flow exactly except for in the vertical direction. In the vertical direction the velocity of the sediment is the difference between the flow velocity and the terminal fall velocity of the sediment.

If the velocities and concentrations are decomposed into time-averaged and fluctuating components and back-substituted into (15.28) and (15.29), subsequent Reynolds averaging produces the equation:

$$\frac{\partial \bar{c}}{\partial t} + \frac{\partial \bar{F}_{si}}{\partial x_i} = 0 \quad (15.30)$$

in which

$$\bar{F}_{si} = (\bar{u}_i - v_s \delta_{i3}) \bar{c} + \overline{u'_i c'} \quad (15.31)$$

The overbars in (15.30) and (15.31) indicate time-averaged quantities and the primes indicate fluctuations about the time average. The flux given by (15.31) has three components: advection by the mean velocity ( $\bar{u}_i \bar{c}$ ), fall velocity of sediment in the vertical direction ( $-v_s \delta_{i3} \bar{c}$ ), and the turbulent Reynolds flux of sediment ( $\overline{u'_i c'}$ ). Consider the vertical component of the flux given by (15.31). The fall velocity of the sediment always transports the sediment towards the bed. If the channel bed is flat and nearly horizontal,  $\bar{u}_3$  is zero near the bed. In this case, suspended sediment transport only occurs if the Reynolds flux term is nonzero (i. e., suspended sediment transport cannot be sustained in the absence of turbulence).

For closure, the Reynolds flux is often modeled following Prandtl's mixing-length hypothesis:

$$\overline{u'_i c'} = -D_d \frac{\partial \bar{c}}{\partial x_i} \quad (15.32)$$

Here  $D_d$  is the kinematic eddy diffusivity of the flow. For fine sediment, it is often assumed that the eddy diffusivity and the eddy viscosity are equal. Then, the eddy diffusivity can be obtained directly from knowledge of the flow field.

Solving (15.30) through (15.32) for any given flow requires a flow model and boundary conditions. For open channel flows, boundary conditions are applied at the free surface and near the bed. The free surface boundary condition is simply that the flux of sediment at the gas–fluid interface is zero. The boundary condition at the bed has historically taken on two forms: specifying the near-bed concentration, and specifying the entrainment (vertical Reynolds flux) of sediment from the bed. Entrainment is perhaps more difficult to measure than concentration, but for uniform flows, entrainment can be directly calculated from concentration measurements using (15.31). Near-bed concentration and entrainment

are usually correlated to the average bed shear stress (or shear velocity) by equations. Examples include *Smith and McLean* [15.248], *van Rijn* [15.249], and *García and Parker* [15.250]. For nonequilibrium flows, it is more appropriate to use entrainment as the boundary condition so that particle settling and particle entrainment can be simultaneously modeled in (15.31).

### Bed Load Transport

Bed load is sediment that is transported by saltation (rolling, bouncing, and sliding) adjacent to the bed. For bed load composed of fine sediment, the saltation layer is very thin. Unlike suspended load, bed load can be sustained in the absence of turbulence. In practice, bed load is usually calculated using equations that correlate bed load with the average dimensionless bed shear stress (Shields stress)

$$\tau^* = \frac{\tau}{\rho g R D} \quad (15.33)$$

where  $\tau$  is the bed shear stress,  $\rho$  is the density of the fluid,  $g$  is the gravitational acceleration,  $R$  is the submerged specific gravity of the sediment ( $\rho_s/\rho - 1$ ),  $\rho_s$  is the density of the sediment, and  $D$  is the median diameter of the sediment. The critical shear stress – the minimum dimensionless shear stress at which sediment resting on the bed will begin to move – is also important. Most bed load functions give the dimensionless bed load  $q^*$  as a function of shear stress raised to the power of 1.5. The dimensionless bed load, or Einstein number, is defined as

$$q^* = \frac{q_b}{D \sqrt{g R D}} \quad (15.34)$$

where  $q_b$  is the volume flux of bed load per unit width of bed. As an example, a frequently used bed load formula is the *Meyer-Peter and Muller* [15.251] formula

$$q^* = 8 (\tau^* - \tau_c^*)^{3/2} \quad (15.35)$$

where  $\tau_c^*$  is obtained by substituting the critical shear stress into (15.33). The reader should be aware that *Wong* [15.252] has found a discrepancy in this formula and provides a viable correction. Many others [15.253–256] have developed relations between bed load and bed shear stress; most equations rely on the critical shear stress as well.

### Shear Stress

As discussed, existing bed load and suspended load theories rely heavily on accurate measurement of bed shear stress. Average bed shear stress has long been the correlate of choice because it is easy to estimate for uniform channels and it occurs where sediment transport begins

and ends – at the interface between the fluid and the bed. In open channel flow, the momentum principle is often applied to determine average bed shear stress. For example, in steady, uniform flow the momentum equation can be used to show

$$\tau_b = \sqrt{\rho g R_h S}, \quad (15.36)$$

where  $\tau_b$  is the bed shear stress,  $\rho$  is the density of the water,  $g$  is the gravitational acceleration,  $R_h$  is the hydraulic radius of the channel, and  $S$  is the energy slope of the channel. For transport in an infinite fluid, velocity measurements can be used to get the time-averaged velocity profile, which can be used in conjunction with known velocity distributions to assess the average bed shear stress.

Determining average bed shear stress is relatively easy for uniform flows with flat beds, but determining instantaneous, local shear stress is not easy, especially if the bed is not flat. Sediment transport is strongly influenced by local variations of shear stress and turbulence bursts, and measuring spatial and temporal variations of shear stress is important. Current methods of measuring local shear stress (hot film sensors, chemical rate sensors, etc.) are impractical above movable beds. Several methods for estimating shear stress from related measurements have been suggested. *Dewey and Crawford* [15.257] suggest that bed shear stress can be indirectly estimated from near-bed measurements of the time-averaged velocity profile, the Reynolds stress, or the turbulent dissipation rate. However, in complex flows these estimates are often inaccurate [15.258]. Other measurements that have been introduced as a replacement for average bed shear stress include turbulent kinetic energy [15.259] and velocity [15.260] near the bed. Measurement of bed shear stress, and bed shear stress substitutes, above movable beds is the subject of ongoing research.

### Summary

In summary, important measurements in sediment transport include concentration, mean and instantaneous sediment flux, and bed shear stress. It is clear that the fluxes and concentrations of greatest importance are often located near the bed. In fact, this is the most difficult part of the flow in which to measure concentrations and fluxes because concentration gradients and velocity gradients are very high, requiring good spatial resolution. In addition, the presence of high concentrations of suspended sediment makes most techniques difficult to apply.

The fundamental measurement associated with sediment transport is sediment mass flux, or mass flow rate of sediment. Measuring the instantaneous mass flux re-

quires either a direct time-based measurement of mass or simultaneous measurement of sediment concentration and velocity. In addition, the sediment size distribution is often important. When measuring fluxes of suspended sediment, it is common practice to measure concentration only and to assume that the mean velocity of the sediment and the flow are equivalent. For bed load measurements, however, the only proven methods require timed collection of bed load samples. This is because the bed load layer is extremely thin, and simultaneous measurements of bed load sediment concentration and velocity are at this time impossible.

### 15.3.2 Methods of Measuring Suspended Sediment Transport

For useful concentration measurements, measuring devices must have good spatial resolution and a small

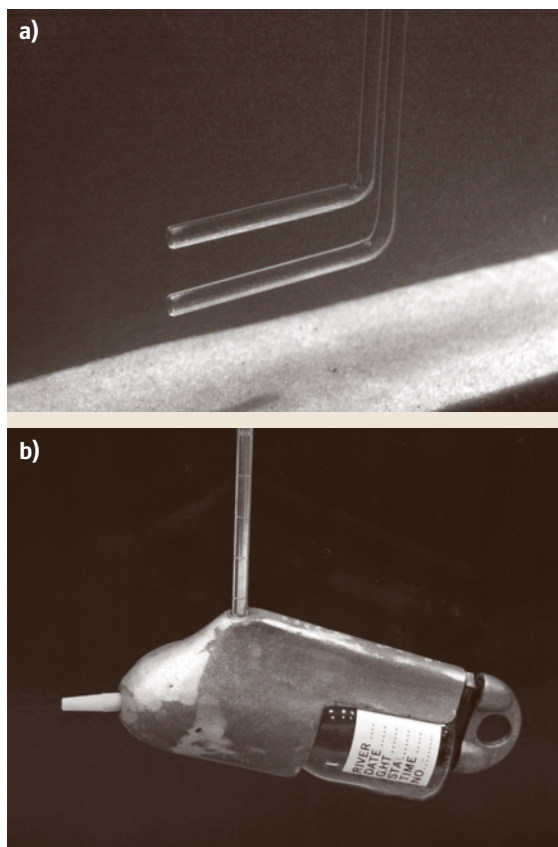


**Fig. 15.77a,b** Two common manual sampling devices: (a) a laboratory system with two manual sampling tubes, (b) a US DH-48 depth-integrating bottle sampler



**Table 15.3** Properties of suspended sediment samplers. Properties given in the table are estimates based on experience, published literature, and manufacturers specifications. Actual properties may vary with design and implementation

Characteristic	Manual samplers	Optical backscatter	Single-frequency acoustic backscatter (ABS)	LISST	FBRM
Typical maximum sampling rate	≈ 0.1 Hz or less	≈ 10 Hz	≈ 10 Hz	Up to 4 Hz – generally less. 1 Hz cited by Wren et al. [15.261]	≈ 0.1 Hz Concentration dependent
Typical estimated measuring volume dimensions	Circular inlet Diameter: 0.3 to 0.7 cm	Cone Half angle: 15° Cone length: ≈ 2.5 cm Cone volume: ≈ 1 to 3 cm <sup>3</sup>	Frustum of a cone Frustum height: ≈ 0.5 cm Frustum radius: ≈ 1 to 5 cm Frustum volume: ≈ 2 to 40 cm <sup>3</sup>	Small cylindrical volume Length 2.5 cm Volume: ≈ 1 cm <sup>3</sup>	Circular annulus Diameter: ≈ 1 cm Volume: ≈ 1 cm <sup>3</sup>
Intrusiveness	Intrusive	Moderately intrusive	Non-intrusive	Intrusive	Intrusive
Optimal/typical size range	Silts and sands	Clays and silts	Sands	2 to 400 μm	1 to 1000 μm
Maximum concentration (by volume)	Very large	≈ 2% (depends on sediment size/type)	≈ 2%	≈ 0.2%	≈ 2%
Sediment size distribution	Simultaneously measures size distribution and concentration	Sensor can only measure concentration of the sediment distribution used in its calibration	Sensor can only measure concentration of the sediment distribution used in its calibration	Measures size distribution and concentration	Measures size distribution – may take substantial time to gather enough data
Overall accuracy of concentration measurements	20 to 100% pump-type isokinetic samplers have highest accuracy	10 to 30%	10 to 30%	20%	Unknown
Ease of use	Easy to implement but time-consuming. Calibration unnecessary but isokinetic requirement adds a level of complexity	Easy to use with proper data logging. Calibration is required and may be time consuming	Moderately difficult to use with proper data logging. Calibration is required and may be time-consuming	Relatively complex	Relatively complex
Relative initial cost	Inexpensive	Moderately inexpensive	Moderately expensive	Expensive	Expensive

measuring volume. For two-dimensional flows the spanwise and lengthwise dimensions of the measuring volume are not critical, but height of the volume should be small relative to the thickness of the boundary layer. A small measuring volume height is necessary since most vertical distributions of suspended sediment are nonlinear. In unsteady flows and in flows in which the response of sediment to turbulence is to be measured, a good time response may also be required.

The most widely used methods of measuring suspended sediment transport are relatively old because they are inexpensive and do not require extensive calibration. In fact, traditional methods of sediment measurement are generally the standard by which new techniques are calibrated. Recent reviews of technology available to measure suspended sediment concentrations include those of White [15.246] and Wren et al. [15.261]. Another useful review, albeit somewhat older, is provided by van Rijn and Schaafsma [15.262].

Typical characteristics of three of the more widely used methods of measuring sediment concentration and size distribution – manual sampling, optical backscatter (OBS), and acoustic backscatter (ABS) – are given in Table 15.3. Two relatively new technologies that allow rapid measurement of nonuniform sediment size distributions, laser in situ scattering and transmissometry (LISST) and focused beam reflectance measurement (FBRM), are also shown in the table. These newer technologies are costly, flow intrusive, and difficult to implement. Nevertheless, their ability to measure both concentration and size distribution makes them worthy of discussion. Note that specifications given in Table 15.3 are estimates and vary somewhat with instrument design and implementation.

Manual Sampling

Of the three most widely used sampling techniques, only manual sampling provides direct, simultaneous measurements of concentration and sediment size range. Unfortunately, manual sampling is flow intrusive, requires sample processing (samples must be dried and weighed), and has poor temporal resolution; optical and

acoustic techniques offer some advantage over manual sampling in these areas.

Manual sampling has been utilized extensively for measuring sediment concentration in sediment transport research [15.264–269]. There are many different types of manual samplers [15.262, 270], two of which are shown in Fig. 15.77. Although there is variation in ease of use, efficiency, and accuracy, most samplers operate similarly. Manual samplers generally consist of a small tube through which sediment/water mixtures are pumped, siphoned, or forced by the flow. The suspensions are carried into a container where they are deposited until sediment concentrations and size ranges can be determined by sieving and weighing the samples. Usually, the sampler nozzle is aligned with the flow, and samples are pumped at the same velocity as the unobstructed flow velocity – a process referred to as isokinetic sampling. Sampling tube diameters are typically 3–7 mm. Since volumetric sediment concentrations are measured directly, results gathered with the sampler are relatively accurate, but maintaining isokinetic sampling is not always easy. Errors result if the sampling velocity is not the same as the flow velocity because the sediment has a higher density than the fluid, and any redirection of streamlines leads to a change in sampled concentration. Winterstein and Stefan [15.269] and Bosman et al. [15.263] demonstrated that the accuracy of manual samplers varies with sampling rate, sediment size, and the angle of the sampler relative to the flow velocity. On the other hand, correction factors, such as those shown in Fig. 15.78 [15.263], can be used to adjust concentration measurements as long as the unobstructed flow velocity is known. In Fig. 15.78,  $\alpha$  is the trapping efficiency (the ratio of the sampled to the true concentration),  $u_s$  is the sampling velocity, and  $u_c$  is the unobstructed flow velocity. If the unobstructed flow velocity is unknown, it is generally best to sample at a high rate. Figure 15.78 demonstrates that sampling at a velocity that is higher than the flow velocity may result in acceptable error. For example, the accuracy is reduced by less than 25% for 0.45 mm sand when intake velocities are two to three times the flow velocity. Reductions in accuracy are even smaller for fine sand. Hay [15.271] and others have suggested that sampling at velocities of as much as four times the flow velocity results in acceptable concentration measurements.

For most flows of interest, manual samplers have good spatial resolution. Furthermore, manual samplers can be used to measure suspensions of nonuniformly sized sediment distributions. Although the samplers do obstruct the flow, they are often small in comparison to

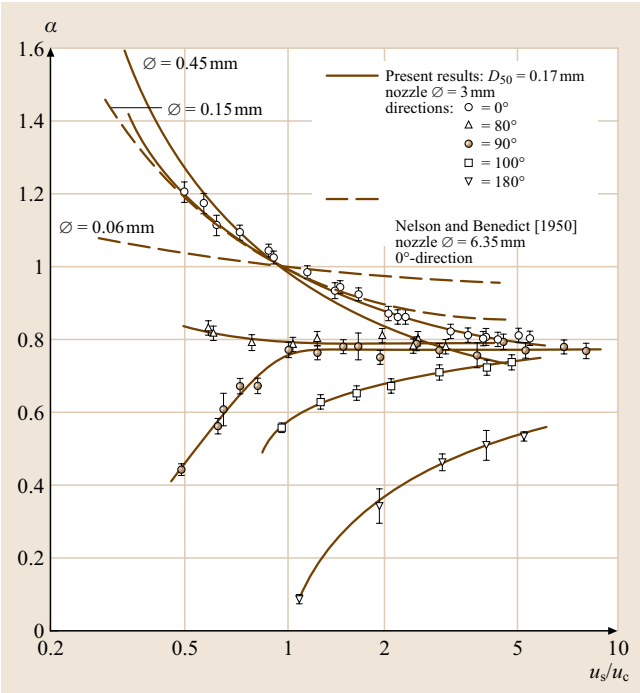


Fig. 15.78 Sampling efficiency of a manual sampler as a function of sampler orientation, sediment size, and sampling velocity (after [15.263])

the scales of interest. However, of the most widely used methods, manual sampling is one of the most intrusive. Manual samplers have three main drawbacks. First, it has already been mentioned that the unobstructed flow velocity must be known in order to sample the flow accurately. In most cases, measurements of suspended sediment concentration are most important near the bed, but this is also the very region where it is most difficult to gather an isokinetic sample or to determine the unobstructed flow velocity. Second, manual samplers have poor temporal resolution. It typically takes a minute or more to gather a manual sample [15.265]. Thus, manual sampling is not suitable for finding correlations between instantaneous concentration and velocity (e.g., measurement of the Reynolds flux) or shear stress. Finally, measurements are inconvenient and require postprocessing to assess size ranges and sediment concentrations.

Aligning manual samplers with the flow is important but not critical. *Nelson and Benedict* [15.272] suggested that a 20° misalignment of the intake has negligible influence on the accuracy of concentration measurements. Figure 15.78 further demonstrates this. For isokinetic samples, a measurement error of only 20% is expected for a 90° misalignment when 0.17 mm sand suspensions are sampled.

A depth-integrating bottle sampler, a field version of the manual sampler, is shown in Fig. 15.77. The depth-integrating sampler is intended to be drawn through the water column at a constant rate in order to determine the total suspended load in a river. Bottle samplers are widely used and have the same characteristics as laboratory samplers, except that they have a larger profile. The fill rate of most bottle samplers is dependent on depth (because of hydrostatic pressure variation) and flow velocity. To accommodate isokinetic sampling, some bottle samplers have a variety of nozzle sizes. Nozzle sizes are selected to achieve the appropriate sampling velocity [15.270].

### Optical Techniques

A number of optical techniques have been utilized to measure suspended sediment concentrations. The majority of optical samplers can be divided into two categories: optical transmission [15.273–275] and optical backscatter [15.276]. Optical transmission devices consist of one or more transmitter/detector pairs. The transmitter is typically an infrared light-emitting diode (LED) and the detector is a photoresistor or photodiode. High concentrations of suspended material reduce the amount of light that travels between the transmitter and the detector.

Optical backscatter (OBS) is a more widely used method for measuring suspended sediment concentrations. In the case of OBS sensors, an emitter transmits light into a small measuring volume, and light reflected from sediment suspended within the sampling volume is measured by a photodetector. The device is a point measurement device, and is relatively easy to implement. The output of the sensors increases linearly with concentration. A typical calibrated sensor can be used to detect sand concentrations of up to 50 g/l and is accurate to  $\pm 0.1$  g/l according to the D&A Instrument Company [15.277]. Errors associated with calibration and implementation reduce the accuracy significantly.

Compared to other electrical devices, transmissometers and OBS sensors are relatively cheap and have high temporal response of about 10 Hz [15.278,279]. Optical sensors have two shortcomings. First, they are somewhat intrusive for small-scale flows. A typical OBS sensor is approximately 3 cm in diameter and 20 cm in length, and has a measuring volume on the order of 3 cm<sup>3</sup>, which is located a small distance from the sensor. Orientation of the sensor can be easily altered, reducing sensor intrusion, but the sensors are point measurement devices, and if an entire vertical profile is desired, multiple sensors are required. Second, although *Green and Boon* [15.280] propose a method of deciphering size distribution from OBS measurements, standard OBS sensors can only measure concentrations of homogeneous suspensions [15.246]. The sensors are calibrated by assuming that increasing reflection intensity is associated with increasing concentration. Variations in grain size cause a breakdown in this assumption. Furthermore, even if concentration measurements were unaffected by particle size, it would be desirable to be able to determine the size gradation of any given sample. *Sutherland et al.* [15.281] also reports some sensitivity of OBS sensors to sediment darkness or hue, such that even if sediment size is constant, a change in the sediment color may lead to a change in sensor calibration.

*White* [15.246] suggests that OBS sensors do not work as well near the bed because they interfere with the flow, and near the water surface, natural light can interfere with OBS measurements. Using OBS sensors is relatively simple as long as they are properly calibrated. In situ calibration is best (using isokinetic samplers), and the sensors must be calibrated with the same sediment that they will be measuring. OBS sensors are particularly susceptible to biofouling (becoming covered with algal slime) if used for more than a few days [15.282]. The effects of biofouling can be avoided by periodi-

cally cleaning the OBS lens. It is possible to automate cleaning [15.283] but this adds cost to the system.

Beach et al. [15.278] tested a fiber-optic backscatter (FOBS) sensor. The FOBS sensor is less intrusive than a standard OBS sensor, with a tip diameter of only 4 mm. Its small size reduces instrument flow interference near the bed. Apart from their size, FOBS sensors have characteristics that are similar to those of standard OBS sensors. Beach et al. [15.278] reported a concentration measurement range of 0–200 g/l for the FOBS sensor that they used. Figure 15.79 shows the approximate dimensions and measuring volume of a FOBS sensor. The extent of the measuring volume varies somewhat with concentration, but it is estimated to be about 3 cm<sup>3</sup> in size. Puleo et al. [15.284] used an array of FOBS sensors to measure vertical concentration profiles of 0.44 mm sand in the swash zone of a beach. Near the bed, the sensors were spaced at 1 cm intervals; sensors that were below bed level had saturated output and were used to identify bed elevation. Recently, fiber-optic backscatter (FOBS) sensors have also been used to measure sediment deposition rates Ridd et al. [15.283]. Ridd et al. were able to measure sediment deposition rates with a resolution of 0.01 mg cm<sup>-2</sup> at an estimated accuracy of 5% in still water.

Laser-based devices can be used to measure size, concentration and particle velocity [15.246]. Two relatively new laser based techniques, focused beam reflectance measurement (FBRM) and laser in situ scattering and transmissometry (LISST) can be used to determine the size distribution of suspensions of nonuniform particles in situ. The FBRM uses a focused, rotating laser to measure particle size range [15.285–287]. When the focused laser intercepts a particle, light is reflected to a photosensor. Since laser rotation speed is known and the time of light reflection is measured, the chord length of the intercepted particle can be determined. Assuming all of the particles are spherical, sediment size distribution can be statistically determined. After integrating over a period of time, the entire size range in the vicinity of the sensor can be determined.

LISST devices rely on transmission and refraction of light by suspended particles to determine both sediment concentration and size distribution [15.288, 289]. A collimated laser is focused through the sampling volume towards a group of concentric photo-optic sensor rings. The laser and the central sensor can be used as a transmissometer, detecting concentration. The outer sensor rings sense light diffraction – a particle-size-dependent property. The maximum measurable concentration is

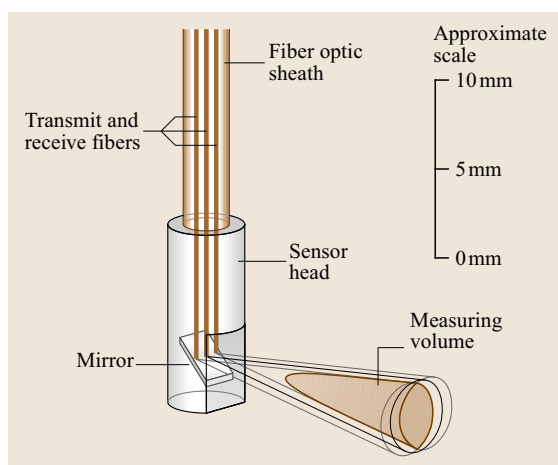


**Fig. 15.79** Illustration of a fiber-optic backscatter (FOBS) sensor and measuring volume (shown as the shaded region). Volumes illuminated by the single transmit fiber and sensed by the dual receive fibers are also depicted. (After [15.278])

limited to about 0.2% by volume, although this limit can be adjusted with design changes. Typical accuracy of concentration measurements is on the order of 20% over the range of sediment sizes that the LISST is designed for [15.290]. Drawbacks of the FBRM and LISST are flow intrusiveness (both are significantly larger than OBS sensors) and cost. Furthermore, the response time of these devices, though in general better than manual sampling, is still slow compared to OBS and acoustic devices. Nevertheless, many field researchers choose to use a single LISST or FBRM device in conjunction with OBS sensor arrays or acoustic sensors, simply to determine the size ranges of suspended sediments [15.291]. Both FBRM and LISST require some degree of calibration, and like all optical sensors, both devices are susceptible to biofouling.

In laboratory studies, velocity and concentration fields have been simultaneously determined for suspended sediment transport of uniform sediment using particle tracking velocimetry techniques. This requires discrimination of flow tracers and sediment particles. There are two methods of discriminating between flow tracers and suspended sediment. The first method is to seed the flow with fluorescent tracers, and to use a filter to eliminate all but the light emitted from the tracers [15.292]. The second method is to discriminate based on particle size [15.293], something that can only be done if the sediment and the flow tracers are significantly different in size. Size distributions of suspended



sediment can also be determined using photographic techniques [15.294]

### Acoustic Techniques

Over the last two decades, there have been significant advances in the use of acoustics to measure suspended sediment. Acoustic sensors have been successfully applied both in the field [15.295, 296] and in the laboratory [15.297, 298]. Like optical transducers, acoustical transducers have been developed that are based on transmission [15.262, 299], but backscatter devices have been favored because of their ability to measure entire concentration profiles. *Thorne and Hanes* [15.300] provide a review of acoustic backscatter devices (ABS), which have the potential to simultaneously measure concentration profiles, velocity profiles, and bed topography. ABS devices have some distinct advantages over manual sampling and optical methods: first, they measure entire concentration profiles nearly non-intrusively; second, data collection is very rapid; and third, once calibrated, an ABS device can be operated without significant sample processing.

Figure 15.80 depicts how ABS devices measure concentration. ABS operation is initiated when the device transmits a pressure pulse into the water column. The pressure pulse travels through the water column at the speed of sound ( $\approx 1500\text{ m/s}$  in water). As it travels through the water column, a fraction of each pulse is reflected back to the transducer by particles suspended in the water. The strength of the return signal is directly related to the sediment concentration. It takes more time for reflections to return from scatterers that are more distant from the transducer. Thus, an entire profile of the sediment concentration can be resolved by measuring the strength of the return signal as a function of time. The amount of time required to gather an entire profile equals the time that it takes for the acoustic pulse to travel from the transducer to the most remote measuring volume and back. Since the speed of sound in water is so high, gathering one concentration profile only takes a fraction of a second. However, pressure waves backscattered from sediment particles are Rayleigh distributed, and multiple profiles must be averaged to measure concentration with any degree of accuracy [15.279, 300]. Typical ABS devices gather profiles at 100 Hz. Averaging enough profiles to reduce concentration uncertainty to about 25% reduces temporal response to 5–10 Hz, depending on the ABS device configuration (short profiling ranges allow higher sampling rates).

ABS sampling volumes are shaped like the frustum of a cone. The radius of the sampling volume increases

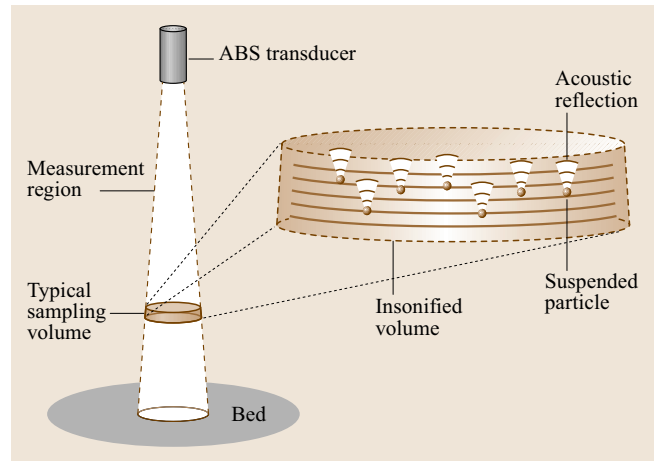


**Fig. 15.80** Depiction of ABS operation. One of the sampling volumes is enlarged to illustrate acoustic reflections from individual particles. The measurement region is composed of many such sampling volumes which become active as the acoustic pulse travels through them

with distance from the transducer because the acoustic pulse spreads as it propagates through the water. The radius of the sampling volume of a typical device may vary between 1 and 5 cm over a 1 m profile. If small sampling volumes are desired, the device should be installed close to the region of interest [15.298]. The height of the sampling volume is dependent on the duration of the transmitted pulse. An estimate of the shortest reliable pulse is about five transducer cycles. For a 2 MHz ABS transducer this translates to a minimum sampling volume height of about 0.2 cm; so fairly good spatial resolution can be achieved with ABS devices. More often, sampling volume heights are on the order of 0.5 cm. The height of the sampling volume also affects the ability of the ABS device to measure near-bed concentrations. The bed produces a very strong acoustic reflection, making it impossible to measure bed load concentrations.

For the same concentration, different sizes of suspended sediment will return different signal strengths to the ABS transducer. Consequently, if nonuniform distributions of sediment are present, a strong signal could indicate low concentrations of coarse sediment, high concentrations of fine sediment, or some combination of the two. Multifrequency ABS systems have been used to simultaneously determine concentration and sediment size [15.296, 301]. However, it has only been possible to simultaneously discern the concentration and mean sediment size of unimodal sediment distributions. Nonuniform size distributions still cannot be resolved

with multifrequency ABS Systems [15.246]. Furthermore, Lynch et al. [15.302] state that acoustic devices are limited to measuring particle sizes of greater than 25  $\mu\text{m}$ . Incidentally, acoustical and optical backscatter devices can also be used in combination to simultaneously estimate suspended sediment particle size and concentration with reasonable accuracy [15.302].

ABS systems consist of a transducer/amplifier combination and a high-speed data-acquisition system. The data acquisition system must be able to capture the amplitude of acoustic return signals with frequencies of up to 5 MHz. For instance, *Admiraal* and *García* [15.298] used a 20 MHz data acquisition board with a 2.25 MHz transducer. One alternative is to use an envelope detector to detect only the peaks of the acoustic return pulse. Using this approach, the transducer output can be sampled at a lower rate. However, in some cases, filtering the transducer output can reduce spatial resolution.

Equations describing acoustic backscattering by suspended sediment have been given by *Hay* [15.271], *Thorne* and *Campbell* [15.303], and *Thorne* et al. [15.304]. According to *Admiraal* and *García* [15.298], the voltage output  $v$  of a typical ABS for measurements in the far field is

$$\langle v^2 \rangle = C \frac{M}{r^2} e^{-4\alpha_t r}, \quad (15.37)$$

where  $M$  is the mass of scatterers per unit volume of fluid,  $r$  is the distance from the transducer to the measuring volume, and  $C$  is a constant determined by calibration. According to *Thorne* et al. [15.304], measurements are in the far field as long as

$$r > \frac{\varepsilon \pi a_t^2}{\lambda}, \quad (15.38)$$

where  $\varepsilon$  is approximately 2,  $a_t$  is the radius of the transducer, and  $\lambda$  is the acoustic wavelength. The acoustic signal is attenuated as it travels through the water, both by particles in the water and by the water itself. The total attenuation coefficient  $\alpha_t$  is given by

$$\alpha_t = \alpha_w + \frac{1}{r} \int_0^r \alpha_s dr, \quad (15.39)$$

where  $\alpha_w$  is the attenuation of the acoustic pulse by the water and  $\alpha_s$  is the attenuation of the acoustic pulse by sediment suspended in the water. Attenuation of sound

by water is given by *Fisher* and *Simmons* [15.305] as:

$$\begin{aligned} \alpha_w &= (55.9 - 2.37T + 4.77 \times 10^{-2}T^2 - 3.48 \times 10^{-4}T^3) \\ &\quad \times 10^{-15} f^2 (1 - 3.84 \times 10^{-4}p + 7.57 \times 10^{-8}p^2), \end{aligned} \quad (15.40)$$

where  $f$  is the frequency of the transmitted signal in Hz,  $T$  is the water temperature in  $^{\circ}\text{C}$ , and  $p$  is the absolute pressure in atm. According to *Hay* [15.271], the attenuation due to particles in the water is negligible when concentrations are less than 1% by volume. For high concentrations of suspended sediment, attenuation due to the sediment is dependent on the concentration, making concentration profiles more difficult to determine. The attenuation can be corrected for by first computing the concentration closest to the sensor, then calculating the corresponding attenuation, then calculating the concentration slightly further from the sensor (using the previously calculated attenuation correction), and so on until the entire concentration profile is resolved. The attenuation due to the suspended sediment has been shown to follow the relation [15.271, 306]:

$$\alpha_s = \zeta M, \quad (15.41)$$

where  $\zeta$  is a constant dependent on the sediment characteristics.

To find the constants  $C$  and  $\zeta$  in (15.37) and (15.41) the ABS device must be calibrated. Once  $C$  and  $\zeta$  are known, an acoustic pulse can be transmitted, the return signal can be measured as a function of time, and (15.37) through (15.41) can be solved to get the mass concentration as a function of distance from the transducer.

While acoustic sensors have been primarily used to measure suspended sediment concentration, it is also possible to use the Doppler shift of the return signal to measure the sediment velocity or flux [15.297, 307, 308]. Likewise, acoustic devices designed for measuring flow velocities can also be used to measure sediment concentration. Examples include acoustic Doppler current profilers [15.291] and cross-correlation velocity profilers [15.309]. *Gartner* [15.291] compared suspended sediment concentration measurements made with acoustic Doppler current profilers (ADCP) and OBS devices. Measurements from the two instruments were well correlated in some locations, but near the bed, measurements did not agree. Nevertheless, the ADCPs did provide useful information about the suspended sediment concentration profile. *Holdaway* et al. [15.310] had some success using an ADCP to measure suspended

sediment concentrations. In their study, they compared concentrations measured using the signal strength of an ADCP with transmissometer measurements. *Holdaway et al.* [15.310] demonstrated that the ADCP provides useful concentration information, but requires in situ calibration and independent information about the local particle size distribution.

Acoustic devices are very sensitive to coarse sediment, while optical sensors are more sensitive to fine sediment [15.262, 279]. Even so, the presence of fine air bubbles or particles other than the sediment particles can result in erroneous acoustic concentration measurements, particularly for low concentrations of suspended sediment [15.246, 279, 298]. The possibility that particulates or air bubbles are contaminating the output can be eliminated by verifying that the output of the device is zero when no suspended sediment is present. *Osborne et al.* [15.279] did a side-by-side comparison of OBS and ABS devices and found that agreement between the two devices was quite good. Concentration measurements using the two devices were within 10% of each other for time scales of several minutes – in their experiments it was not practical to compare instantaneous measurements.

#### Calibration of Acoustical and Optical Sensors

In order to use acoustical and optical measuring devices, the devices must first be calibrated. All parts of the sensor must be underwater, and temperature is important. It is best if these devices are calibrated in situ, most likely using manual samplers. If it is not possible to calibrate the device in situ, it can also be calibrated in a laboratory facility. The facility in which the device is calibrated should have a known or measurable suspended sediment distribution. *Hay* [15.271] lists a number of calibration methods, including the sediment-laden jet that he used to calibrate his acoustic sensor. *Thorne and Hanes* [15.300] give an example of another calibration facility – a calibration tower. *Thorne and Hanes* emphasize that the tower must be run for a long period of time prior to calibration to allow microbubbles to escape.

It is difficult to keep coarse sediment uniformly suspended so *Admiraal and García* [15.298] built a recirculating duct that maintained high velocities in all places where the sediment was present. High velocities kept the sediment in suspension at all times. A holding tank allowed microbubbles trapped in the water to be released, preventing the bubbles from causing erroneous measurements. The sediment in the duct bypassed the holding tank so that the concentration in the duct

remained nearly constant throughout each test. Measurements with the ABS device confirmed that the suspended sediment concentration was uniform for the entire cross section of the duct. A sediment sampler situated just downstream of the location where ABS profiles were gathered was used to calibrate the ABS device.

Appropriate calibration requires a similar range of concentrations in the calibration facility and the test facility. Furthermore, the sediment attenuation correction for concentration profiles is nonlinear, and *Hay* [15.271] points out that a time-averaged attenuation correction will erroneously overcorrect the acoustic output voltage if there are large concentration fluctuations. This can be particularly problematic if concentration fluctuations are substantially different in the calibration facility and the test facility. One way of overcoming this problem is to parametrically estimate instantaneous attenuation and to use it to correct measured voltages before averaging.

Optical sensors must also be calibrated. However, since most optical devices are for point measurements, calibrating them is less difficult. A typical field method for calibrating OBS sensors is to gather bed material at the field site, mix it with water in a bucket, and keep it in suspension while multiple readings are taken with the sensor. Samples of the suspension in the bucket are collected for later analysis (drying and weighing), and the process is repeated with samples that are increasingly dilute [15.291]. Since OBS sensors are likely to be used with fine sediment, keeping the sediment in suspension throughout the calibration process is not so difficult.

### 15.3.3 Bed Load Sediment Measurements

As noted previously, bed load is much more difficult to accurately measure than suspended load. The main reason for this is that bed load is transported as a thin layer near the bed in a region with strong velocity gradients. Most optical, acoustic, and electronic sensors cannot resolve at scales necessary to distinguish the thin layer of bed load from the stationary layer of sediment just below it. Furthermore, bed load concentrations are often high, and optical and acoustic devices have difficulty penetrating through the high concentrations of sediment. Consequently, accepted methods of measuring bed load are nontechnical and have been around for many years. Needless to say, there is a need to improve spatial and temporal resolution of bed load measurements before many of the most important sediment transport questions can be answered. So much of the sediment travels very near to the bed, that it is difficult to resolve some very elementary questions. For now, only time- and spatially

integrated bed load can be measured with a reasonable degree of accuracy. For the most part, this is done using sediment traps or pressure-difference samplers.

### Pressure-Difference Samplers

The most commonly used bed load sampling devices are pressure-difference samplers. The Arnhem sampler, which dates back to 1937, was one of the earliest and widely used devices of this type [15.244, 270]. A more contemporary pressure-difference sampler is the Helley–Smith bed load sampler [15.312]. The Helley–Smith sampler was designed for use with coarse sands and fine gravels (2–10 mm in diameter) but has been regularly used to measure bed load composed of finer sediments [15.313]. Boat-deployed and handheld versions of the Helley–Smith sampler are available and are shown in Fig. 15.81. The sampler nozzle has two square openings at the front and rear. The downstream opening is larger than the upstream opening, and when the sampler is placed on the bed of a stream or river, a pressure drop is created inside the nozzle between the inlet and outlet.

The pressure drop causes the flow to accelerate through the nozzle, and sediment that enters through the front of the nozzle is carried into a bag attached to the rear of the nozzle. Sediment that is not fine enough to escape through the mesh bag becomes trapped and can later be dried, sieved, and weighed. According to *Edwards and Glysson* [15.270], a newer version of the sampler has a nozzle outlet to inlet ratio of 1.40 instead of the traditional ratio of 3.22. Both area ratios are accepted by federal agencies, pending further investigation. The optimal area ratio likely depends on sediment size, as coarse sediment requires higher velocities to push it through the nozzle, and fine sediment will be over-sampled if nozzle velocities are too high. Each bed load sample is a time-integrated (non-instantaneous) measurement.

For bed load samplers, sampling efficiency is defined as the ratio of the measured bed load to the actual bed load [15.312]. Sampling efficiencies of between 100 and 160% have been reported for the Helley–Smith sampler [15.270]. Researchers have found that fine and medium sands are typically oversampled by the original Helley–Smith sampler because the sampler was designed for coarse sand and fine gravels. For example, *Emmett* [15.311] found sampling efficiencies of about 150% and 93% for sediment size ranges of 0.25–0.5 mm and 0.5–16 mm, respectively. Emmett hypothesized that the high efficiency of the finer sediment might have been caused by inadvertent trapping of suspended load by the device. The amount of suspended sediment trapped by the device can be substantial since suspended load concentrations are highest near the bed.

The measuring efficiency of pressure-difference samplers should be used to correct measurements – especially for fine sediment which may result in an efficiency of 150%. Ignoring the sampling efficiency will cause a bias error. In addition to trapping suspended sediment, there are other sources of error associated with pressure-difference samplers. A first source of error is due to placement of the sampler. The lower lip of the nozzle must be flush with the bed. The presence of bedforms may prevent the sampler from sitting flat on the bed, leading to local scour and an erroneous bed load measurement. Moreover, inadvertently pushing the nozzle into the bed will cause an overestimate of the local bed load. Second, misalignment of the sampler with the mean flow direction can cause greatly reduced trapping efficiencies. *Gaudet et al.* [15.313] found trapping efficiencies could be reduced by nearly 50% for misalignments of only 10°. These misalignments may be caused by carelessness, but also by channel geometry and bedform effects.

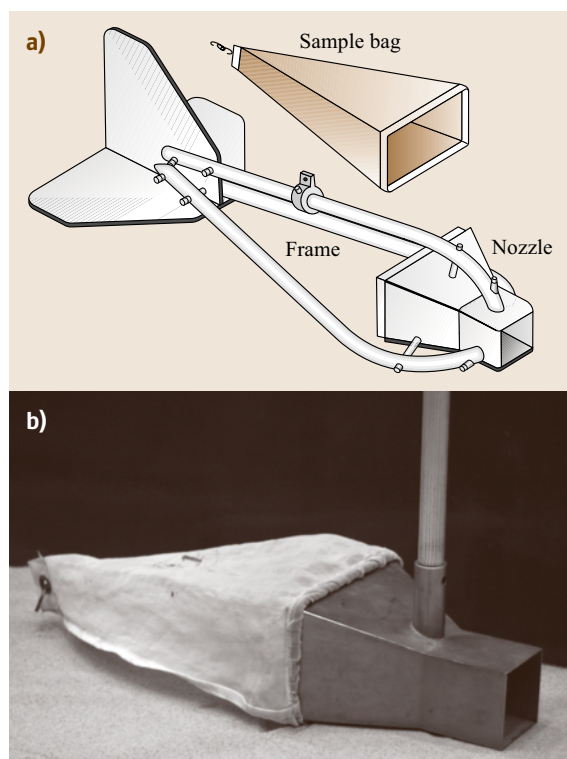


**Fig. 15.81a,b** The Helley–Smith pressure-difference sampler: (a) boat-deployed sampler (after [15.311]) and (b) handheld sampler



Bed load can vary significantly in the streamwise and transverse directions, so multiple measurements are necessary to measure the total bed load in a stream. For bed load composed of 1.15 mm sediment, *Helley and Smith* [15.312] found that the standard deviations of individual bed load measurements were extremely large – typically the same size as the measured bed load itself. It is difficult to assess the accuracy of the bed load sampler for individual measurements because even in uniform flow, bed load varies a great deal due to the presence of bedforms and other factors, both temporally and spatially. Thus, assessing how much of the standard deviation is due to natural variability of the bed load and how much is due to inaccuracy of the device is not entirely possible. *Hubbell et al.* [15.314] found that although relative uncertainty of bed load samplers could be high for low bed load rates, measurement uncertainty was generally small. However, they also demonstrated that actual bed load rates can vary significantly in the streamwise direction (for instance, in the presence of dunes), resulting in poor estimates of the time integrated total bed load if only one sample was gathered at each position along a transect. It has often been assumed that when the sampler is properly used the accuracy of individual samples is relatively good for coarse sand and fine gravel, but recent studies have even questioned this assumption [15.315, 316].

For field measurements, *Gaweesh and van Rijn* [15.317] demonstrated that individual pressure-difference sampler measurements may have an uncertainty of 50% in the presence of bedforms because the variation of bed load on the bedform is as high as 50% and the sampling location is often random. The uncertainty of the total bed load in a river can be reduced to less than 20% by gathering multiple bed load measurements across the river transect [15.299, 317]. The required number of samples varies with river characteristics and flow conditions; but *Gaweesh and van Rijn* [15.317] recommend dividing the river into seven subsections and gathering 25 samples per subsection. The samples gathered in each subsection should be gathered over the streamwise length of the bedforms in that subsection so that a representative measure of the average bed load is obtained [15.317]. This is clearly a very time-consuming process.

Measuring total bed load with a Helley–Smith sampler requires the following steps:

1. The sampler is lowered until it rests on the bed – the lower lip of the nozzle should be flush with the bed, but the sampler should not be pushed into the bed.

2. A sample is collected for a fixed amount of time. The collection time can be determined by collecting test samples at locations where the bed load is thought to be the highest. Choose the collection time such that the bag is never filled to more than 40% of its capacity [15.270] otherwise the pressure drop across the nozzle will be reduced. The collection time that is finally selected should be used for all samples. According to *Edwards and Glysson* [15.270], a collection time of less than 60 seconds is usually preferred.
3. *Emmett* [15.311] suggests that samples should be gathered at 20 equally spaced lateral locations to satisfactorily estimate the total bed load. For practicality, *Edwards and Glysson* [15.270] recommend collecting 40 bed load samples for each transverse (two at each lateral location). For accuracy, other researchers recommend more samples [15.299, 317]. Specific strategies for collecting the samples are given by *Edwards and Glysson* [15.270].
4. The bed load per unit width at a sampling location is determined by dividing the mass of the sample by the width of the sampler nozzle and the collection time. If multiple samples are gathered for a sampling location, the resulting bed load per unit width measurements must be averaged.
5. The total bed load is obtained by multiplying each bed load per unit width by the width of the river subsection that it represents and then summing all of the subsection bed loads.

Properly using a pressure-difference sampler is costly and time-consuming. The samples collected with the sampler must be postprocessed, making on-site data checks impractical.

### Sediment Trapping

In laboratory settings, although instantaneous and local bed load is difficult to measure, time-averaged bed load (or total load) can be accurately measured simply by capturing the sediment in a trap at the end of the test flume for weighing [15.314, 318]; in this case, the only concern is whether or not the trap affects the measurements being gathered.

In the field, pit- or slot-type samplers are simply pits or depressions made in the stream bed (Fig. 15.82). Bed load falls into the depressions where it is trapped. The trapped sediment must be weighed in situ [15.319, 320] or removed for weighing in some fashion, possibly by means of a conveyor or pump [15.311]. Well-designed pit- and slot-type bed load traps capture nearly 100% of

coarse bed load [15.244, 315] but may also catch some suspended load. Fine bed load material may be sampled at a lower efficiency because turbulence within the trap can resuspend some of the finer material, carrying it out of the trap [15.315]. Pit-type samplers are often permanent, as they are built into the stream bed. They can be used to accurately measure total bed load, but since they affect the bathymetry, they are not suitable for measuring spatial or temporal variations associated with bedforms or channel geometry. Permanent sediment traps are costly to install and operate.

### Acoustic Measurements

In the future, it may become possible to use acoustics to measure bed load non-intrusively with good spatial and temporal resolution. Acoustics could provide easier measurements in rivers that are deep and where traditional bed load measurements are difficult. Application of acoustics to measure bed load is only in its infancy, and acoustics have only been used to measure bed load velocities [15.321]. In fact, the bed load layer is quite thin, but covers a wide velocity range. It is difficult to say what velocity is actually being measured by acoustic pulses reflected from the bed, and bed load velocity measurements may be biased [15.322]. At this time, only the relative magnitude of bed load velocities at various locations on a river transect can be gathered with sufficient confidence. However, even this information is useful, as it can be used to appropriately plan bed load collection with pressure-difference samplers.

### 15.3.4 Total Load Measurements

Subdividing the sediment load into suspended load and bed load is not always necessary; sometimes it is sufficient to determine only the total sediment load in a river. For instance, the longevity of a large reservoir is based on the total sediment load into the reservoir because all of the sediment settles in the reservoir, regardless of the mode of transport in the river upstream of the reservoir. When a location can be identified that puts the entire sediment load into suspension, that location is a good place to measure the total load since it is easier to measure suspended load accurately than it is to measure bed load. According to *Graf* [15.244], all of the sediment load may be forced into suspension at rapids or constrictions (bridges), or a turbulence flume may be constructed to force all of the sediment into suspension [15.323]. Once in suspension, the sediment may be sampled using isokinetic samplers or other suspension measurement techniques.

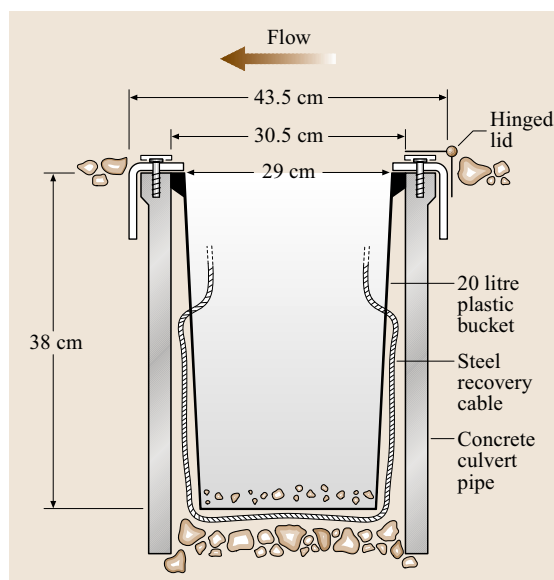


**Fig. 15.82** A pit-style trap. The trap is cylindrical to eliminate directional bias (after [15.315])

### 15.3.5 Other Measurement Techniques

As described by *White* [15.246] there are perhaps two primary areas of sediment transport measurement that need improvement: sampling sediment fluxes near the bed, and sampling ranges of particle sizes. Traditional techniques partially overcome these issues, but are flow intrusive, have low temporal resolution, and require difficult sample processing. Although suspended sediment concentration can in some cases be measured with relatively high temporal and spatial resolution, the same is not true of bed load.

Only the most widely used sediment transport measurement techniques have been discussed in this chapter. There are a number of less commonly used techniques available that the reader should be aware of. These techniques include: nuclear radiation backscatter or transmission; hydrostatic pressure-difference measurements; sediment impact measurements; spectral reflectance; and tracking natural or seeded tracer particles that have magnetic, radiation, or fluorescence properties. Most of these techniques are not widely used either because they are too costly, too difficult to implement (particularly the tracking and nuclear techniques), or too inaccurate. The reader is encouraged to explore the review articles written by *White* [15.246] and *Wren et al.* [15.261] to find out more about these techniques.

## References

- 15.1 M.S. Plesset: Physical effects on cavitation and boiling, Proc. 1st Symp. Naval Hydrodynamics, ed. by F.S. Sherman (Academic, Washington 1957) 297–323
- 15.2 R.E.A. Arndt, R. Voigt, J.P. Sinclair, P.R. Rodrigue: Cavitation erosion in hydroturbines, J. Hydraul. Eng. **115**, 1297–1315 (1989)
- 15.3 K.M. Kalumuck, G.L. Chahine: The use of cavitating jets to oxidize organic compounds in water, J. Fluids Eng. **122**, 465–470 (2000)
- 15.4 C. Gong, D.P. Hart: Ultrasound induced cavitation and sonochemical yields, J. Acoust. Soc. Am. **5**, 1–8 (1998)
- 15.5 L.C. Burrill: Sir Charles Parsons and cavitation – 1950 Parsons Memorial Lecture, Trans. Inst. Marine Eng. **63**, 149–167 (1951)
- 15.6 L. Rayleigh: On the pressure developed in a liquid during the collapse of a spherical cavity, Phil. Mag. **34**, 94–98 (1917)
- 15.7 M. Minnaert: On musical air-bubbles and sounds of running water, Phil. Mag. **16**, 235–248 (1933)
- 15.8 M.S. Plesset, S.A. Zwick: The growth of vapor bubbles in superheated liquids, J. Appl. Phys **25**(4), 493–500 (1954)
- 15.9 P.S. Epstein, M.S. Plesset: On the stability of gas bubbles in liquid–gas solutions, J. Chem. Phys. **18**(11), 1505–1509 (1950)
- 15.10 P. Eisenberg: Mechanics of cavitation. In: *Handbook of Fluid Dynamics*, ed. by V.L. Streeter (McGraw Hill, New York 1961) pp. 12.2–12.24, , Section 12
- 15.11 T.W. Wu: Cavity and wake flows, Annu. Rev. Fluid Mech. **4** (1972)
- 15.12 A.J. Acosta, B.R. Parkin: Cavitation inception – A selective review, J. Ship Res. **19**, 193–205 (1975)
- 15.13 M.S. Plesset, A. Prosperetti: Bubble dynamics and cavitation, Annu. Rev. Fluid Mech. **9**, 145–185 (1977)
- 15.14 R.E.A. Arndt: Cavitation in fluid machinery and hydraulic structures, Annu. Rev. Fluid Mech. **13**, 273–328 (1981)
- 15.15 R.E.A. Arndt: *Recent Advances in Cavitation Research*, Adv. Hydrosol., Vol. 12 (Academic, San Diego 1981) pp. 1–77
- 15.16 R.E.A. Arndt: Cavitation in vortical flows, Annu. Rev. Fluid Mech. **34**, 143–175 (2002)
- 15.17 J.R. Blake, D.C. Gibson: Cavitation bubbles near boundaries, Annu. Rev. Fluid Mech. **19**, 99–123 (1987)
- 15.18 E.P. Rood: Review – mechanisms of cavitation inception, J. Fluids Eng. **113**, 163–175 (1991)
- 15.19 R.T. Knapp, J.W. Daily, F.G. Hammit: *Cavitation* (McGraw-Hill, New York 1970)
- 15.20 F.R. Young: *Cavitation* (McGraw-Hill, London 1989)
- 15.21 C.E. Brennen: *Cavitation and Bubble Dynamics* (Oxford University Press, New York 1995)
- 15.22 J.P. Franc, J.M. Michel: *Fundamentals of Cavitation* (Kluwer Academic, Dordrecht 2004)
- 15.23 I. Anton: *Cavitatie*. Editura Academiei (Polytechnical Institute of Timisoara, Bucharest 1984), R-79717
- 15.24 W.H. Isay: *Kavitation* (Hansa Schroedter, 1981)
- 15.25 R. Taghavi: *Cavitation Inception in Axisymmetric Jets*. Ph.D. Thesis (University of Minnesota, Minneapolis 1985)
- 15.26 R.E.A. Arndt: *Vortex Cavitation, Fluid Vortices* (Kluwer Academic, Dordrecht 1995) pp. 731–782
- 15.27 R.W. Kermeen: Water tunnel tests of NACA 66<sub>1</sub>–012 hydrofoil in noncavitating and cavitating flows, Calif. Inst. Tech. Hydrodynamics Lab. Rep. **47-7** (1956)
- 15.28 M.L. Billet: Cavitation nuclei measurements – a review, Cavitation and Multiphase Flow Forum (ASME, New York 1985)
- 15.29 D.D. Joseph: Cavitation and the state of stress in a flowing liquid, J. Fluid Mech. **366**, 367–378 (1998)
- 15.30 B. Gindroz, M.L. Billet: Influence of the nuclei on the cavitation inception for different types of cavitation on ship propellers, J. Fluids Eng. **120**, 171–178 (1998)
- 15.31 J.W. Holl: An effect of air content on the occurrence of cavitation, J. Basic Eng. **82**, 941–946 (1960)
- 15.32 M. Kjeldsen, R.E.A. Arndt, M. Effertz: Spectral characteristics of sheet/cloud cavitation, J. Fluids Eng. **122**, 481–487 (2000)
- 15.33 W.M. Deeprose, N.W. King, P.J. McNulty, Pearsall: Cavitation noise, flow noise and erosion, Proc. Conf. Cavitation Inst. Mech. Eng., London (1974)
- 15.34 G.F. Wislicenus: *Fluid Mechanics of Turbomachinery*, Vol. 1 (Dover, New York 1965)
- 15.35 J.O. Young, J.W. Holl: Effects of cavitation on periodic wakes behind symmetric wedges, J. Basic Eng. **88**, 163–176 (1966)
- 15.36 B. Belahadji, J. Michel: Numerical and experimental study of cavitating vortices in the turbulent wake, Proc. Third Int. Symp. Cavitation, Grenoble, ed. by J.M. Michel, H. Kato (1998)
- 15.37 K.R. Laberteaux, S.L. Ceccio: Flow in the Closure Region of Closed Partial Attached Cavitation, Proc. Third Int. Symp. Cavitation, Grenoble, ed. by J.M. Michel, H. Kato (1998) 197–202
- 15.38 S. Gopalan, J. Katz: Flow structure and modeling issues in the closure region of attached cavitation, Phys. Fluids **12**, 895–911 (2000)
- 15.39 R.E.A. Arndt, C.C.S. Song, M. Kjeldsen, J. He, A. Keller: Instability of partial cavitation: A numerical/experimental approach. In: *Proc. 23rd Symp. Naval Hydrodynamics*, ed. by E. Rood (Academic, Washington 2000)
- 15.40 R.E.A. Arndt, C. Ellis, S. Paul: Preliminary investigation of the use of air injection to mitigate cavitation erosion, J. Fluids Eng. **117**, 498–592 (1995)

- 15.41 Y. Kawanami, H. Kato, H. Yamaguchi: Three-dimensional characteristics of the cavities formed on a two-dimensional hydrofoil, *Trans Int. Symp. on Cavitation*, ed. by J.M. Michel, H. Kato (1998) 191–196
- 15.42 D.R. Stinebring: *Scaling of Cavitation Damage*. MS Thesis (Pennsylvania State University, Pennsylvania 1976)
- 15.43 J.W. Daily, V.E. Johnson: Turbulence and boundary layer effects on cavitation inception from gas nuclei, *Trans ASME* **78**, 1695–1706 (1956)
- 15.44 R.E.A. Arndt, A.T. Ippen: Rough surface effects on cavitation inception, *J. Basic Eng.* **90**, 249–261 (1968)
- 15.45 R.E.A. Arndt, W.K. George: Pressure fields and cavitation in turbulent shear flows. In: *12th Symp. Naval Hydrodynamics*, ed. by R. Cooper (Academic, Washington 1978) pp. 327–339
- 15.46 A. Michalke: On spatially growing disturbances in an inviscid shear layer, *J. Fluid Mech.* **23**, 521–544 (1965)
- 15.47 Chahine, V.E. Johnson: Mechanics of self-resonating cavitating jets, *Jets and Cavities-Int. Symp.* **31**, 21–33 (1985)
- 15.48 C.S. Crowe, F.H. Champagne: Orderly structure in jet turbulence, *J. Fluid Mech.* **48**, 547 (1971)
- 15.49 M. Versluis, B. Schmitz, A. von der Heydt, D. Lohse: On the sound of snapping shrimp, 53rd Annu. Meeting Am. Phys. Soc. Div. Fluid Dynamics, Washington (2000), Video Presentation
- 15.50 B. Ran, J. Katz: Pressure fluctuations and their effect on cavitation inception within water jets, *J. Fluid Mech.* **262**, 223–263 (1994)
- 15.51 K.K. Ooi: Scale effects on cavitation inception in submerged water jets: A new look, *J. Fluid Mech.* **151**, 367–390 (1985)
- 15.52 J. Katz, T.J. O'Hern: Cavitation in large scale shear flows, *J. Fluids Eng.* **108**, 373–376 (1986)
- 15.53 T.J. O'Hern: *Cavitation Scale Effects: I. Nuclei Distributions in Natural Waters, II. Cavitation Inception in a Turbulent Shear Flow*. Ph.D. Thesis (California Institute of Technology, Pasadena 1987)
- 15.54 S. Gopalan, J. Katz, O. Knio: The flow structure in the near field of jets and its effect on cavitation inception, *J. Fluid Mech.* **398**, 1–43 (1999)
- 15.55 K.K. Ooi, A.J. Acosta: The utilization of specially tailored air bubbles as static pressure sensors in a jet, *J. Fluids Eng.* **106**, 459–465 (1983)
- 15.56 R. Taghavi, R.E.A. Arndt: *Cavitation in various types of shear flow, Cavitation in Hydraulic Structures and Turbomachinery*, ASME FED-25 (ASME, New York 1985) pp. 129–134
- 15.57 T. Leger, S.L. Ceccio: Examination of the flow near the leading edge of attached cavitation – Part 1. Detachment of two-dimensional and axisymmetric cavities, *J. Fluid Mech.* **376**, 61–90 (1998)
- 15.58 T. Leger, L.P. Bernal, S.L. Ceccio: Examination of the flow near the leading edge of attached cavitation – Part 2. Incipient breakdown of two-dimensional and axisymmetric cavities, *J. Fluid Mech.* **376**, 91–113 (1998)
- 15.59 R.E.A. Arndt, C. Ellis, S. Paul: Application of piezoelectric film in cavitation research, *J. Hydraul. Eng.* **123**, 539–548 (1997)
- 15.60 S. Watanabe, Y. Tsujimoto, J.-P. Franc, J.-M. Michel: Linear analyses of cavitating instabilities, *Proc. Third Int. Symp. Cavitation*, Grenoble, ed. by J.M. Michel, H. Kato (1998)
- 15.61 B. Svingen, M. Kjeldsen, R.E.A. Arndt: Dynamics of closed circuit hydraulic model loops, *Proc. ASME Fluids Eng. Summer Meeting*, Montreal (2002)
- 15.62 J.P. Franc: Partial cavity instabilities and re-entrant jet, CAV 2001: Fourth Int. Symp. Cavitation, ed. by C.E. Brennen, R.E.A. Arndt, L.S. Ceccio (California Institute of Technology, Pasadena 2001), <http://cav2001.library.caltech.edu/>
- 15.63 F. Avellan, P. Dupont, M. Farhat: Cavitation erosion power, *Proc. Cavitation* **91.116**, 135–140 (1991)
- 15.64 H. Yamaguchi, M. Tanaka, H. Kato: A numerical study on the mechanism of vortex generation downstream of a sheet cavity on a two dimensional hydrofoil, *Cavitation and Multiphase Flow Forum*, Vol. 109 (ASME, New York 1991)
- 15.65 M. Kjeldsen: Theoretical and experimental investigations of the instability of an attached cavity, *Proc. ASME Fluids Eng. Div. Summer Mtg.*, Vancouver (1997), Paper FEDSM97-3268
- 15.66 R.E.A. Arndt: *Cavitation Near Surfaces of Distributed Roughness*. Ph.D. Dissertation (Massachusetts Institute of Technology, Boston 1967)
- 15.67 T.J. Schauer: *An Experimental Study of a Ventilated Supercavitating Vehicle*. MS Thesis (University of Minnesota, Minnesota 2003)
- 15.68 M. Wosnik, T.J. Schauer, R.E.A. Arndt: Experimental investigation of the turbulent bubbly wake in a ventilated flow. In: *Advances in Turbulence X*, ed. by H.I. Andersson, P.-A. Krogstad (CIMNE, Barcelona 2004) pp. 657–660
- 15.69 E.A. Brujan, G.S. Keen, A. Vogel, J.R. Blake: The final stage of the collapse of a cavitation bubble close to a rigid boundary, *Phys. Fluids* **14**, 85–92 (2002)
- 15.70 W. Lauterborn, H. Bolle: Experimental investigations of cavitation-bubble collapse in the neighborhood of a solid boundary, *J. Fluid Mech.* **72**, 391–399 (1975)
- 15.71 Y. Tomita, A. Shima: Mechanisms of impulsive pressure generation and damage pit formation by bubble collapse, *J. Fluid Mech.* **169**, 535–564 (1986)
- 15.72 A. Vogel, W. Lauterborn, R. Timm: Optical and acoustic investigations of the dynamics of laser-produced cavitation bubbles near a solid boundary, *J. Fluid Mech.* **206**, 299–338 (1989)
- 15.73 D.R. Stinebring, R.E.A. Arndt, J.W. Holl: Scaling of cavitation damage, *J. Hydronautics* **111**(3), 67–73 (1977)



- 15.74 A. Thiruvengadam: *Scaling laws for cavitation erosion* (Hydronautics Inc., Laurel 1971)
- 15.75 R.E.A. Arndt: Hydraulic turbines. In: *Hydropower Engineering Handbook*, ed. by J. Gulliver, R.E.A. Arndt (McGraw-Hill, New York 1991) pp. 4.1–4.67
- 15.76 P. Bourdon, R. Simoneau, F. Avellan, M. Farhat: Vibratory Characteristics of Erosive Cavitation Vortices Downstream of a Fixed Leading Edge Cavity, Proc. 15th IAHR Symp., Belgrade (1990)
- 15.77 F. Avellan, P. Dupont, I. Ryhming: Generation mechanism and dynamics of cavitation vortices downstream of a fixed leading edge cavity, Proc. 17th Symp. on Naval Hydrodynamics, ed. by E. Rood (Academic, Washington 1988)
- 15.78 P.A. Abbot, R.E.A. Arndt, T.B. Shanahan: Modulation noise analysis of cavitating hydrofoils, ASME FED. 176. In: *Proc. Symp. Bubble Noise and Cavitation Erosion in Fluid Systems*, ed. by R.E.A. Arndt (ASME, New York 1993)
- 15.79 Q. Le, J.P. Franc, J.M. Michel: Partial cavities: Global behavior and mean pressure distribution, J. Fluids Eng. **115**, 253–248 (1993)
- 15.80 Q. Le, J.P. Franc, J.M. Michel: Partial cavities: Pressure pulse distribution around cavity closure, J. Fluids Eng. **115**, 249–254 (1993)
- 15.81 I. Hansson, K.A. Mørch: The dynamics of cavity clusters in ultrasonic (vibratory) cavitation erosion, J. Appl. Phys. **51**, 4651–4658 (1980)
- 15.82 A. Prosperetti, N.Q. Lu, H.S. Kim: Active and passive acoustic behavior of bubble clouds at the ocean's surface, J. Acoust. Soc. Am. **93**(6), 3117–3127 (1993)
- 15.83 T. Colonius, C.E. Brennen, A.T. Preston: A numerical investigation of unsteady bubbly cavitating nozzle flows, Phys. Fluids **14**, 300–311 (2002)
- 15.84 L. van Wijngaarden: On the collective collapse of a large number of cavitation bubbles in water, Proc. 11th Int. Cong. of Appl. Mech., ed. by H. Görtler (Springer, Berlin, Heidelberg 1964)
- 15.85 Y.C. Wang, C.E. Brennen: Shock development in the collapse of a cloud of bubbles, ASME Cavitation and Multiphase Flow Forum 153 (ASME, New York 1994)
- 15.86 P.A. Abbot, D.W. Morton, T.B. Shanahan: Hydroturbine cavitation detection using advanced acoustic emission techniques, Hydroacoustic Facilities and Experimentation Techniques, ASME Winter Annual Meeting, Atlanta (ASME, New York 1991)
- 15.87 J. Wetzel, R.E.A. Arndt: Hydrodynamic design considerations for hydroacoustic facilities: I flow quality, J. Fluids Eng. **116**(2), 324–331 (1994)
- 15.88 J. Wetzel, R.E.A. Arndt: Hydrodynamic design considerations for hydroacoustic facilities: II pump design factors, J. Fluids Eng. **116**(2), 332–337 (1994)
- 15.89 H. Durrer: Cavitation erosion and fluid mechanics, Sulzer Tech. Rev. **3**, 55–61 (1986)
- 15.90 H. Soyama, H. Kumano: The fundamental threshold level – a new parameter for predicting cavitation erosion resistance, J. Testing Evaluation **30**(5), 421–431 (2002)
- 15.91 B. Vyas, C.M. Preece: Stress produced in a solid by cavitation, J. Appl. Phys. **47**, 5133–5138 (1976)
- 15.92 R. Simoneau, A. Archer: *Transposition of Cavitation Marks on Different Hardness Metals*. ASME Fluids Engineering Division Summer Meeting, FEDSM97–3300 (ASME, New York 1997)
- 15.93 B. Belahadji, J.P. Franc, J.M. Michel: A statistical analysis of cavitation erosion pits, J. Fluid Eng. **113**, 700–706 (1991)
- 15.94 H. Soyama, T. Ikohagi, R. Oba: Observation of the cavitating jet in a narrow watercourse, ASME FED Cavitation Multiphase Flow **194**, 79–82 (1994)
- 15.95 J. Steller: International cavitation erosion test and qualitative assessment of material resistance to cavitation, Wear **233–235**, 51–64 (1999)
- 15.96 B.C. Syamala Rao, N.S. Lakshmana Rao, K. Seetharamiah: Cavitation erosion studies with venturi and rotating disk in water, J. Basic Eng. **92**, 563–579 (1970)
- 15.97 H. Kadoi, T. Sasajima: Cavitation erosion prediction using a “soft surface”, Int. Shipbuilding Prog. **25**, 141–150 (1978)
- 15.98 H. Lindgren, C.A. Johnsson: Cavitation inception on headforms, ITTC comparative experiments, Proc. 11th Towing Tank Conf., Tokyo (1966) 219–232
- 15.99 M.S. Plesset: *Cavitating Flows*, California Institute of Technology, Rep. 85–46 (California Institute of Technology, Pasadena 1969)
- 15.100 C.C. Church: A method to account for acoustic microstreaming when predicting bubble growth rates produced by rectified diffusion, J. Acoust. Soc. Am. **84**, 1758–1764 (1988)
- 15.101 H.B. Marschall, K.A. Mørch, A.P. Keller, M. Kjeldsen: Cavitation inception by almost spherical solid particles in water, 4th Int. Symp. on Cavitation, Pasadena, ed. by C.E. Brennen, R.E.A. Arndt, L.S. Ceccio (2001)
- 15.102 D. Ma: *Experimental Studies of Water Quality Effects on Tip Vortex Cavitation*. MS Thesis (University of Minnesota, Minnesota 1994)
- 15.103 J.H.J. van der Meulen: Incipient and desinent cavitation on hemispherical nosed bodies, Int. Shipbuilding Prog. **12**, 21–32 (1972)
- 15.104 A.P. Keller: Cavitation Scale Effects: Empirically Found Relations and the Correlation of Cavitation Number and Hydrodynamic Coefficients, 4th Int. Symp. on Cavitation, Pasadena, ed. by C.E. Brennen, R.E.A. Arndt, L.S. Ceccio (2001)
- 15.105 D.T. Kawakami, Q. Qin, R.E.A. Arndt: Can water quality affect the lift dynamics of cavitating hydrofoils?, 5th Int. Symp. on Cavitation, Osaka, ed. by Y. Tsujimoto (2003)
- 15.106 A.B. Hastings: *Biographical Memoirs: Donald Dexter van Slyke* (National Academy of Sciences, Washington 1976) pp. 308–361

- 15.107 F. Numachi: Über die Kavitationsentstehung mit besonderem Bezug auf der Luftgehalt des Wassers, Ing-Arch. **7**, 396–409 (1936)
- 15.108 W. Heller: *Hydrodynamische Effekte unter besonderer Berücksichtigung der Wasserqualität* (Technische Universität Dresden, Dresden 2004)
- 15.109 W. Heller: A new approach for determination of cavitation sensitivity of water, 4th ASME JSME Joint fluid Engineering Conference, Honolulu (2003)
- 15.110 F.B. Peterson: Hydrodynamic cavitation and some considerations of the influence of free gas content. In: *9th Symp. on Naval Hydrodynamics*, ed. by R. Cooper (Academic, Washington 1972)
- 15.111 R.E.A. Arndt, A.P. Keller: Free gas content effects on cavitation inception and noise in a free shear flow, Proc. IAHR Symp. Two Phase Flow and Cavitation in Power Generation Systems, Grenoble (1976) 3–16
- 15.112 R. Duraiswami, S. Prabhukumar, G.L. Chahine: Bubble size measurement using an inverse acoustic scattering method, J. Acoust. Soc. Am. **104**, 2699–2717 (1998)
- 15.113 G.L. Chahine, K.M. Kalumuck: Development of a near real-time instrument for nuclei measurement: The ABS acoustic bubble spectrometer, 4th ASME JSME Joint Fluid Eng. Conf., Honolulu (ASME, New York 2003)
- 15.114 T.M. Pham, J.M. Michel, Y. Lecoffre: Dynamical nuclei measurement: On the development and the performance evaluation of an optimized center-body meter, J. Fluids Eng. **119**, 744–750 (1997)
- 15.115 T.G. Leighton: *The Acoustic Bubble* (Academic, San Diego 1994)
- 15.116 D.M. Oldenzil: *Bubble Cavitation in Relation to Liquid Quality. Ph.D. Thesis* (Technical University Twente, Twente 1979)
- 15.117 A.P. Keller: Influence of the cavitation nucleus spectrum on cavitation inception, investigated with a scattered light counting method, J. Basic Eng. **94**, 917–925 (1972)
- 15.118 H. Wang: *Experimental Study of Water Bubbly Hydrofoil Wakes. MS Thesis* (University of Minnesota, Minnesota 2004)
- 15.119 H. Tanger, E.A. Weitendorf: Applicability tests for the phase Doppler anemometer for cavitation nuclei measurements, J. Fluids Eng. **114**, 443–449 (1992)
- 15.120 Schiebe F.R.: Measurement of the Cavitation Susceptibility of Water Using Standard Bodies. St. Anthony Falls Hydraulic Laboratory, Rep. 118 (1972)
- 15.121 A.P. Keller: A vortex-nozzle cavitation susceptibility meter in routine application in cavitation inception measurements, Proc. Euromech. Colloquium 222 – Unsteady Cavitation and Its Effects (1987)
- 15.122 Silberman E., Schiebe F.R., Mroska E.: The Use of Standard Bodies to Measure the Cavitation Strength of Water. St Anthony Falls Hydraulic Laboratory, Rep. 141 (1973)
- 15.123 D.M. Oldenzil: Measurements on the cavitation susceptibility of water, 5th Conf. on Fluid Machinery Budapest **2**, 737–748 (1975)
- 15.124 Y. Lecoffre, J. Bonnin: Cavitation Test and Nucleation Control. In: *International Symposium on Cavitation Inception, ASME Winter Annual Meeting, New York*, ed. by W.B. Morgan, B.R. Parkin (ASME, New York 1979) pp. 141–147
- 15.125 L. d'Agostino, A.J. Acosta: On the design of cavitation susceptibility meters, Proc. 20th Am. Towing Tank Conf. **1**, 307–350 (1983)
- 15.126 F.G. Blake: *The Onset of Cavitation in Liquids I*, Acoustics Res. Lab., Tech Memo No 12 (Harvard Univ., Cambridge 1949)
- 15.127 F.E. Fox, K.F. Herzfeld: Gas bubbles with organic skin as cavitation nuclei, Ac. Soc. Am. **26**, 984–989 (1954)
- 15.128 E.N. Harvey, W.D. McElroy, A.H. Whiteley: On cavitation formation in water, J. Appl. Phys. **18**, 162–172 (1947)
- 15.129 R.E.A. Arndt, A.P. Keller: Water quality effects on cavitation inception in a trailing vortex, J. Fluids Eng. **114**, 430–438 (1992)
- 15.130 J.W. Holl, A.L. Treaster: Cavitation hysteresis, J. Basic Eng. **88**, 199–212 (1966)
- 15.131 R.E.A. Arndt, A.P. Keller: A case study of international cooperation: 30 years of collaboration in cavitation research, Proc. 4th ASME-JSME Joint Fluids Eng. Conf., Honolulu (2003), Available on CD
- 15.132 A. Richardson: *The Evolution of the Parsons Steam Turbine* (Engineering, London 1911)
- 15.133 R.E.A. Arndt, B.H. Maines: Nucleation and bubble dynamics in vortical flows, J. Fluids Eng. **122**, 488–493 (2000)
- 15.134 W.K. Blake, M.J. Wolpert, F.E. Geib: Cavitation noise and inception as influenced by boundary layer development on a hydrofoil, J. Fluid Mech. **80**(4), 617–640 (1977)
- 15.135 H. Higuchi, R.E.A. Arndt, M.F. Rogers: Characteristics of tip vortex noise, J. Fluids Eng. **111**, 495–501 (1989)
- 15.136 S.J. Barker: Measurements of radiated noise in the Caltech high-speed water tunnel, Part II: Radiated noise from cavitating hydrofoils, GALCIT (1975), Final Report on ONR contract Hydrodynamic Radiated Noise
- 15.137 R.E.A. Arndt, C.C.S. Song, Q. Qin: Experimental and numerical investigations of cavitation, 22nd IAHR Symposium on Hydraulic Machinery and Systems, Stockholm (2004)
- 15.138 R.W. Kermeen, B.R. Parkin: Incipient cavitation and wake flow behind sharp edged disks, CIT Hydrodynamics Lab Rep. **84-5** (1957)

- 15.139 R.E.A. Arndt, M. Levy: Acoustic radiation from cavitating hydrofoils, Proc. 7th Int. Congress on Noise and Vibration, Garmisch (1999)
- 15.140 T.H. Maiman: Stimulated optical radiation in ruby, Nature **187**, 493–494 (1960)
- 15.141 F. Durst, A. Melling, J.H. Whitelaw: *Principles and Practice of Laser Doppler Anemometry* (Academic, London 1981)
- 15.142 H.E. Albrecht, M. Borys, N. Damaschke, C. Tropea: *Laser Doppler and Phase Doppler Measurement Techniques* (Springer, Berlin, Heidelberg 2003)
- 15.143 R.J. Adrian: Particle-imaging techniques for experimental fluid mechanics, Annu. Rev. Fluid Mech. **23**, 261–304 (1991)
- 15.144 J. Westerweel: Fundamentals of digital particle image velocimetry, Meas. Sci. Technol. **8**, 1379–1392 (1997)
- 15.145 G. Sridhar, B. Ran, J. Katz: Implementation of particle image velocimetry to multi-phase flow, Cavitation Multiphase Flow Forum **109**, 205–210 (1991)
- 15.146 D.P. Towers, C.E. Towers, C.H. Buckberry, M. Reeves: A colour PIV system employing fluorescent particles for two-phase flow measurements, Meas. Sci. Technol. **10**, 824–830 (1999)
- 15.147 L.G. Fontecha: *PIV measurements in the wake of a supercavitating body*. MS Thesis (Chalmers University of Technology, Gothenburg 2004)
- 15.148 Y.A. Hassan, T.K. Blanchat, C.H. Seeley, R.E. Canaan: Simultaneous velocity measurements of both components of a two-phase flow using particle image velocimetry, Int. J. Multiphase Flow **18**, 371–395 (1992)
- 15.149 Y.A. Hassan, W. Schmidl, J. Ortiz-Villafuerte: Investigation of three-dimensional two-phase flow structure in a bubbly pipe flow, Meas. Sci. Technol. **9**, 309–326 (1998)
- 15.150 L. Gui, W. Merzkirch: Phase separation of PIV measurements in two-phase flow by applying a digital mask technique, ERCOFTAC Bull. **30**, 45–48 (1996)
- 15.151 R. Lindken, L. Gui, W. Merzkirch: Velocity measurements in multiphase flow by means of particle image velocimetry, Chem. Eng. Tech. **22**, 202–206 (1999)
- 15.152 R. Lindken, W. Merzkirch: Velocity measurements of liquid and gaseous phase for a system of bubbles rising in water, Exp. Fluids **29**, S194–S201 (2000)
- 15.153 J. Sakakibara, R.B. Wicker, J.K. Eaton: Measurements of the particle-fluid velocity correlation and the extra dissipation in a round jet, Int. J. Multiphase Flow **22**, 863–881 (1996)
- 15.154 W.J. Easson, M.L. Jakobsen: Slippage measurements in two-phase flows using particle image velocimetry, Institute of Physics Optical Group Half Day Conference Optics and Optical Diagnostics in Combustion (1996)
- 15.155 T.R. Oakley, E. Loth, R.J. Adrian: A two-phase cinematic PIV method for bubbly flows, J. Fluids Eng. **119**, 707–712 (1997)
- 15.156 K.T. Kiger, C. Pan: PIV technique for the simultaneous measurement of dilute two-phase flow, J. Fluids Eng. **122**, 811–818 (2000)
- 15.157 E. Delnoij, J. Westerweel, N.G. Deen, J.A.M. Kuipers, W.P.M. van Swaaij: Ensemble correlation PIV applied to bubble plumes rising in a bubble column, Chem. Eng. Sci. **54**, 5159–5171 (1999)
- 15.158 D.A. Khalitov, E.K. Longmire: Simultaneous two-phase PIV by two-parameter phase discrimination, Simultaneous two-phase PIV by two-parameter phase discrimination, Exp. Fluids **32**(2), 252–268 (2002)
- 15.159 M. Arnardottir: *Fundamentals of PIV Applied to Two-Phase Water-Bubble Flow*. MS Thesis (Aalborg University, Aalborg 2001)
- 15.160 G. Chaine, D.E. Nikitopoulos: Multiphase digital particle image velocimetry in a dispersed, bubbly, axisymmetric jet, Proc. ASME 2002 FEDSM, FEDSM2002-31435, Montreal (ASME, New York 2002)
- 15.161 A. Melling: Tracer particles and seeding for particle image velocimetry, Meas. Sci. Technol. **8**, 1406–1416 (1997)
- 15.162 K.R. Laberteaux, S.L. Ceccio: Partial cavity flows – Part 1. Cavities forming on models without spanwise variation, J. Fluid Mech. **431**, 1–41 (2001)
- 15.163 K.R. Laberteaux, S.L. Ceccio: Partial cavity flows – Part 2. Cavities forming test objects with spanwise variation, J. Fluid Mech. **431**, 43–63 (2001)
- 15.164 C.O. Iyer, S.L. Ceccio: The influence of developed cavitation on the flow of a turbulent shear layer, Phys. Fluids **14**, 3414–3431 (2002)
- 15.165 M. Wosnik, T.J. Schauer, R.E.A. Arndt: Experimental Study of a Ventilated Supercavitating Vehicle, Conference paper for CAV 2003–Fifth International Symposium on Cavitation, Osaka, ed. by Y. Tsujimoto (2003)
- 15.166 M. Wosnik, L. Fontecha, R.E.A. Arndt: Measurements in high void-fraction bubbly wakes created by ventilated supercavitation, Proc. ASME-FEDSM2005, ASME Fluids Eng. Div. Summer Meeting, Houston (2005), paper FEDSM2005-77200
- 15.167 M. Wosnik, R.E.A. Arndt: Measurements in high void-fraction turbulent bubbly wakes created by axisymmetric ventilated supercavitation, Proc. Sixth Int. Symp. Cavitation CAV2006, Wageningen (2006)
- 15.168 P.B.V. Johansson, W.K. George, M.J. Gourlay: Equilibrium similarity, effects of initial conditions and local Reynolds number on the axisymmetric wake, Phys. Fluids **15**, 603–617 (2003)
- 15.169 D.P. Hart: High-speed PIV analysis using compressed image correlatoion, J. Fluids Eng. **120**, 463–470 (1998)

- 15.170 A. Vogel, W. Lauterborn: Time-resolved particle image velocimetry used in the investigation of cavitation bubble dynamics, *Appl. Opt.* **27**(9), 1869–1876 (1988)
- 15.171 R.F. Mudde, J.S. Groen, H.E.A. van den Akker: Application of LDA to bubbly flows, *Nucl. Eng. Des.* **184**, 329–338 (1998)
- 15.172 J.S. Groen, R.F. Mudde, H.E.A. van den Akker: On the application of LDA to bubbly flow in the wobbling regime, *Exp. Fluids* **27**, 435–449 (1999)
- 15.173 T. Börner, W.W. Martin, H.J. Leutheuser: Comparative measurements in bubbly two-phase flow using laser Doppler and hot-film anemometry, *Chem. Eng. Commun.* **28**, 29–43 (1984)
- 15.174 S.L. Lee, F. Durst: On the motion of particles in turbulent duct flow, *Int. J. Multiphase Flow* **8**, 125–146 (1982)
- 15.175 S. So, H. Morikita, S. Tagaki, Y. Matsumoto: Laser Doppler velocimetry measurement of turbulent bubbly channel flow, *Exp. Fluids* **33**, 135–142 (2002)
- 15.176 H.R.E. van Maanen: *Retrieval of Turbulence and Turbulence Properties Form Randomly Sampled Laser Doppler Anemometry Data with Noise*. Ph.D. Thesis (Delft University of Technology, Delft 1999)
- 15.177 S. Guet, H.R.E. van Maanen, R.F. Mudde: Feasibility of LDA measurements in high void fraction bubbly flow, 11th Int. Symp. on Applications of Laser Techniques to Fluid Mechanics, Lisbon (2002)
- 15.178 A. Kubota, H. Kato, H. Yamaguchi, M. Maeda: Unsteady structure measurement of cloud cavitation on a foil section using conditional sampling technique, *J. Fluids Eng.* **111**, 204–210 (1989)
- 15.179 A.A. Naqwi, R. Menon, L.M. Fingerson: An adaptive phase/Doppler system and its applications including particle sizing in submicron and nanometer ranges, *Exp. Fluids* **20**, 328–334 (1996)
- 15.180 F. Burdin, N.A. Tsochatzidis, P. Guiraud, A.M. Wilhelm, H. Delmas: Characterisation of the acoustic cavitation cloud by two laser techniques, *Ultrason. Sonochem.* **6**, 43–51 (1999)
- 15.181 T.J. Sun: *A Theoretical and Experimental Study of Non-Condensable Turbulent Bubbly Jets*. Ph.D. Thesis (Pennsylvania State University, Pennsylvania 1985)
- 15.182 T.Y. Sun, G.M. Faeth: Structure of turbulent bubbly jets – I. Methods and centerline properties, *Int. J. Multiphase Flow* **12**, 99–114 (1986)
- 15.183 T.Y. Sun, G.M. Faeth: Structure of turbulent bubbly jets – II. Phase property profiles, *Int. J. Multiphase Flow* **12**, 115–126 (1986)
- 15.184 S. Kumar, D.E. Nikitopoulos, E.E. Michaelides: Effect of bubbles on the turbulence near the exit of a liquid jet, *Exp. Fluids* **7**, 487–494 (1989)
- 15.185 K.N. Stanley: *Non-Intrusive Characterization of a Dispersed Bubbly Axisymmetric Jet*. Ph.D. Thesis (Louisiana State University, Baton Rouge 2001)
- 15.186 K.N. Stanley, D.E. Nikitopoulos: Dispersed bubbly axisymmetric jets, *Proc. of the 4th Int. Conference on Multiphase Flows*, New Orleans (2001)
- 15.187 S. Kim, X.Y. Fu, X. Wang, M. Ishii: Development of the miniaturized four-sensor conductivity probe and the signal processing scheme, *Int. J. Heat Mass Transfer* **43**, 4101–4118 (2000)
- 15.188 L.G. Neal, S.G. Bankoff: A high resolution resistivity probe for determination of local void properties in gas liquid flow, *AIChE J.* **9**, 490–494 (1963)
- 15.189 O.C. Jones: Two-phase flow measurement techniques in gas-liquid systems. In: *Fluid Mechanics Measurements*, ed. by R.J. Goldstein (Hemisphere, Washington 1983) pp. 479–558
- 15.190 R.F. Mudde, T. Saito: Hydrodynamical similarities between bubble column and bubbly pipe flow, *J. Fluid Mech.* **437**, 203–228 (2001)
- 15.191 J.-M. Le Corre, E. Hervieu, M. Ishii, J.-M. Delhay: Benchmarking and improvements of measurement techniques for local-time-averaged two-phase flow parameters, *Exp. Fluids* **35**, 448–458 (2003)
- 15.192 A. Cartellier: Simultaneous void fraction measurement, bubble velocity, and size estimate using a single optical probe in gas-liquid two-phase flows, *Rev. Sci. Instrum.* **63**, 5442–5453 (1992)
- 15.193 G.J. Kirouac, T.A. Trabold, P.F. Vassallo, W.E. Moore, R. Kumar: Instrumentation development in two-phase flow, *Exp. Thermal Fluid Sci.* **20**, 79–93 (1999)
- 15.194 B. Shamoun, M. El Beshbeeshy, R. Bonazza: Light extinction technique for void fraction measurements in bubbly flow, *Exp. Fluids* **26**, 16–26 (1999)
- 15.195 F. Burdin, P. Guiraud, A.M. Wilhelm, H. Delmas: Implementation of the laser diffraction technique for acoustic cavitation bubble investigations, *Part. Part. Syst. Charact.* **19**, 73–83 (2002)
- 15.196 S. Vagle, D.M. Farmer: A comparison of four methods for bubble size and void fraction measurements, *IEEE J. Oceanic Eng.* **23**, 211–222 (1998)
- 15.197 M. Perlin: *Statistical Analysis of Visual Wave Observations and Gage/Radar Measurements*, *Coastal Engr Res. Center, USACE, Misc Paper 84-6* (U.S. Army Corps of Engineers, Washington 1984)
- 15.198 A.V. Babanin, I.R. Young, M.L. Banner: Breaking probabilities for dominant surface waves on water of finite constant depth, *J. Geophys. Res.* **106**(C6), 11659–11676 (2001)
- 15.199 TM6: An Ocean Wave Measuring Instrument, *Tech. Memo 6*, Beach Erosion Board 1–52 (1948)
- 15.200 W.S. Campbell: *An Electronic Wave-Height Measuring Apparatus*, US Navy DW Taylor Model Basin, Rep. 859 (U.S. Dept. of the Navy, Washington 1953)
- 15.201 L.B. Wilner: Variable capacitance liquid level sensors, *Rev. Sci. Instr.* **31**(5), 501–507 (1960)
- 15.202 S.A. Hughes: *Physical Models and Laboratory Techniques in Coastal Engineering* (World Scientific, Singapore 1993)



- 15.203 F.T. Korsmeyer: *The Capacitance Wave Probe*, NA & ME Dept Rep (Univ. Michigan, Ann Arbor 1980)
- 15.204 G.V. Sturm, F.Y. Sorrell: Optical wave measurement technique and experimental comparison with conventional wave height probes, *Appl. Opt.* **12**(8), 1928–1933 (1973)
- 15.205 M. Perlin, C.-L. Ting: Steep gravity-capillary waves within the internal resonance regime, *Phys. Fluids A* **4**(11), 2466–2478 (1992)
- 15.206 W.H. Munk: *Measurement of Waves from Pressure Fluctuations at Ocean Bottom*, Scripps Inst. Ocean, Wave Proj Rep No. 5 (The Scripps Institution of Oceanography, La Jolla 1944)
- 15.207 R.G. Folsom, A.B. White, M.F. Killory: *Deep Water Wave Measurements, I, II, III, IV* (Univ. of Calif. Fluid Mech. Lab, Berkeley 1945, 1946)
- 15.208 B. Strong, B. Brumley, E.A. Terray, G.W. Stone: The Performance of ADCP-Derived Directional Wave Spectra and Comparison with other Independent Measurements, *Proc. MTS/IEEE Oceans Conf.*, Providence (Institute of Electronic and Electrical Engineers, Piscataway 2000)
- 15.209 M.V. Trevorrow: Measurement of ocean wave directional spectra using Doppler side-scan sonar arrays, *J. Atmos. Oceanic Technol.* **12**(3), 603–616 (1995)
- 15.210 H.-T. Liu, J.-T. Lin: On the spectra of high-frequency wind waves, *J. Fluid Mech.* **123**, 165–185 (1982)
- 15.211 J.H. Duncan, A.A. Dimas: Surface ripples due to steady breaking waves, *J. Fluid Mech.* **329**, 309–339 (1996)
- 15.212 C.S. Cox: Measurements of slopes of high-frequency wind waves, *J. Marine Res.* **16**(3), 199–225 (1958)
- 15.213 J.R. Saylor: Internal reflection beneath capillary water waves: A method for measuring wave slope, *Appl. Opt.* **36**(6), 1121–1129 (1997)
- 15.214 J. Wu, J.M. Lawrence, E.S. Tebay, M.P. Tulin: A multiple purpose optical instrument for studies of short steep water waves, *Rev. Sci. Instrum.* **40**(9), 1209–1213 (1969)
- 15.215 J. Wu: Directional slope and curvature distributions of wind waves, *J. Fluid Mech.* **79**(3), 463–480 (1977)
- 15.216 J.D. Barter, K.L. Beach, P.H.Y. Lee: Collocated and simultaneous measurement of surface slope and amplitude of water waves, *Rev. Sci. Instrum.* **64**(9), 2661–2665 (1993)
- 15.217 B. Jahne, M. Schmidt, R. Rocholz: Combined optical slope/height measurements of short wind waves: Principle and calibration, *Meas. Sci. Technol.* **16**, 1937–1944 (2005)
- 15.218 B. Jahne, J. Klink, S. Waas: Imaging of short ocean wind waves: A critical theoretical review, *J. Opt. Soc. Am. A* **11**(8), 2197–2209 (1994)
- 15.219 X. Liu, J.H. Duncan: The effects of surfactants on spilling breaking waves, *Nature* **421**, 520–523 (2003)
- 15.220 J.M. Killen: The sonic surface-wave transducer, *Am. Towing Tank Conf.*, Univ. Calif., Berkeley (Defense Technical Information Center, Ft. Belvoir 1959)
- 15.221 H. Mitsuyasu, Y.-Y. Kuo, A. Masuda: On the dispersion relation of random gravity waves – Part 2: An experiment, *J. Fluid Mech.* **92**, 731–749 (1979)
- 15.222 D.W. Wang, P.A. Hwang: The dispersion relation of short wind waves from space-time wave measurements, *J. Atmos. Oceanic Technol.* **21**, 1936–1945 (2004)
- 15.223 M. Perlin, H. Lin, C.-L. Ting: On parasitic capillary waves generated by steep gravity waves: An experimental investigation with spatial and temporal measurements, *J. Fluid Mech.* **255**, 597–620 (1993)
- 15.224 J.B. Carneal, C.W. Baumann, P. Atsavapranee, J.H. Hamilton, J. Shan: A global laser rangefinder profilometry system for the measurement of three-dimensional wave surfaces, *Proc. of REDSM05, 2005, ASME Fluids Eng. Div. Summer Meeting and Exhib.*, Houston (Am. Soc. Mech. Eng., Washington 2005)
- 15.225 M.L. Banner, I.S.F. Jones, J.C. Trinder: Wavenumber spectra of short gravity waves, *J. Fluid Mech.* **198**, 321–344 (1989)
- 15.226 J.M. Wanek, C.H. Wu: Automated trinocular stereo imaging system for three-dimensional surface wave measurement, *Ocean Eng.* **33**, 723–747 (2006)
- 15.227 I. Grant, Y. Zhao, G.H. Smith, J.N. Stewart: Split-screen, single-camera, laser-matrix, stereogrammetry instrument for topographical water wave measurements, *Appl. Opt.* **34**(19), 3806–3809 (1995)
- 15.228 I. Grant, N. Stewart, I.A. Padilla-Perez: Topographical measurements of water waves using the projection moire method, *Appl. Opt.* **29**(28), 3981–3983 (1990)
- 15.229 E.J. Bock, T. Hara: Optical measurements of capillary-gravity wave spectra using a scanning laser slope gauge, *J. Atmos. Oceanic Technol.* **12**, 395–403 (1995)
- 15.230 Q. Li, M. Zhao, S. Tang, S. Sun, J. Wu: Two-dimensional scanning laser slope gauge: Measurements of ocean-ripple structures, *Appl. Opt.* **32**(24), 4590–4597 (1993)
- 15.231 B. Jahne, K. Riemer: Two-dimensional wave number spectra of small-scale water surface waves, *J. Geophys. Res.* **95**(C7), 11531–11546 (1990)
- 15.232 W.C. Keller, B.L. Gotwols: Two-dimensional optical measurement of wave slope, *Appl. Opt.* **22**, 3476–3478 (1983)
- 15.233 X. Zhang, C.S. Cox: Measuring the two-dimensional structure of a wavy water surface optically: A surface gradient detector, *Exp. Fluids* **17**, 225–237 (1994)
- 15.234 X. Zhang, D. Dabiri, M. Gharib: Optical mapping of fluid density interfaces: Concepts and imple-

- mentations, *Rev. Sci. Instrum.* **67**(5), 1858–1868 (1996)
- 15.235 J.S. Bendat, A.G. Piersol: *Random Data: Analysis and Measurement Procedures* (Wiley, New York 1986)
- 15.236 A. Papoulis: *Probability, Random Variables and Stochastic Processes*, 2nd edn. (McGraw Hill, New York 1984)
- 15.237 M.K. Ochi: *Applied Probability and Stochastic Processes* (Wiley-Interscience, New York 1990)
- 15.238 M.K. Ochi: *Ocean Waves: The Stochastic Approach* (Cambridge Univ Press, Cambridge 1998)
- 15.239 K.R. Bodge: *The Design, Development, and Evaluation of a Differential Pressure Gauge Directional Wave Monitor*, Coastal Engr Res Center, USACE, Misc Rep 82-11 (U.S. Army Corps of Engineers, Washington 1982)
- 15.240 M.S. Longuet-Higgins, D.E. Cartwright, N.D. Smith: *Observations of the Directional Spectrum of Sea Waves Using the Motions of a Floating Buoy*, Ocean Waves Spectra (Prentice-Hall, Englewood Cliffs 1963)
- 15.241 H.E. Krogstad, S.F. Barstow, S.E. Aasen, I. Rodriguez: Some recent developments in wave buoy measurement technology, *Coastal Eng.* **37**(3-4), 309–329 (1999)
- 15.242 RD Instruments: *Waves User's Guide*, Pub No. 957-6148-00 (RD Instruments, San Diego 2001)
- 15.243 C. Zuffada, G. Hajj, J.B. Thomas: *Sea Height and Roughness with GPS Reflections*, <http://www.nasatech.com/Briefs/Jun02/NP020943.html> (NASA, Washington 2002)
- 15.244 W.H. Graf: *Hydraulics of Sediment Transport* (McGraw-Hill, New York 1971)
- 15.245 S.M. Yalin: *Mechanics of Sediment Transport* (Pergamon, Oxford 1972)
- 15.246 T.E. White: Status of measurement techniques for coastal sediment transport, *Coastal Eng.* **35**(1998), 17–45 (1998)
- 15.247 J.M. Phillips, D.E. Walling: An assessment of the effects of sample collection, storage, and resuspension on the representativeness of measurements of the effective particle size distribution of fluvial suspended sediment, *Water Resour.* **29**, 298–308 (1995)
- 15.248 J.D. Smith, S.R. McLean: Spatially averaged flow over a wavy surface, *J. Geophys. Res.* **83**, 1735–1746 (1977)
- 15.249 L.C. van Rijn: Sediment transport – Part II. Suspended load transport, *J. Hydraul. Eng.* **110**(11), 1613–1641 (1984)
- 15.250 M. García, G. Parker: Entrainment of bed sediment into suspension, *J. Hydraul. Eng.* **117**(4), 414–435 (1991)
- 15.251 E. Meyer-Peter, R. Muller: Formulas for bedload transport, *Proc. 2nd Cong. International Association of Hydraulic Res.*, Stockholm (IAHR, Delft 1948) 39–64
- 15.252 M. Wong: Does the bedload equation of Meyer-Peter and Muller fit its own data?, *Int. Association of Hydraulic Research Congress*, Thessaloniki (IAHR, Delft 2003)
- 15.253 H. Einstein: *The Bed-Load Function for Sediment Transportation in Open Channel Flows*, Technical Bulletin 1026, Soil Conservation Service (U.S. Dept. of Agriculture, Washington 1950)
- 15.254 M.S. Yalin: An expression for bedload transportation, *J. Hydraul. Div. ASCE* **89**(HY3), 221–250 (1963)
- 15.255 F. Engelund, J. Fredsoe: A sediment transport model for straight alluvial channels, *Nordic Hydrol.* **7**, 293–306 (1976)
- 15.256 R. Fernandez Luque, R. van Beek: Erosion and transport of bed sediment, *J. Hydraul. Res.* **14**(2), 127–144 (1976)
- 15.257 R.K. Dewey, W.R. Crawford: Bottom stress estimates from vertical dissipation rate profiles on the continental shelf, *J. Phys. Oceanography* **18**(8), 1167–1177 (1988)
- 15.258 R.L. Soulsby, K.R. Dyer: The form of the near-bed velocity profile in tidally accelerating flow, *J. Geophys. Res.* **86**(C9), 8067–8074 (1981)
- 15.259 K.W. Bedford, O. Wai, C.M. Libicki, R.L.II. van Evra: Sediment entrainment and deposition measurements in long island sound, *J. Hydraul. Div. ASCE* **113**(10), 1325–1342 (1987)
- 15.260 M.W. Schmееckle, J.M. Nelson: Direct numerical simulation of bedload transport using a local, dynamic boundary condition, *Sedimentology* **50**(2), 279–301 (2003)
- 15.261 D.G. Wren, B.D. Barkdoll, R.A. Kuhnle, R.W. Darrow: Field techniques for suspended-sediment measurement, *J. Hydraul. Eng.* **126**(2), 97–104 (2000)
- 15.262 L.C. van Rijn, A.S. Schaafsma: Evaluation of measuring instruments for suspended sediment, *Int. Conf. Measuring Techniques of Hydraulics Phenomena in Offshore, Coastal, and Inland Waters*, London (British Hydraulic Research Association, Cranfield 1986) 401–423
- 15.263 J.J. Bosman, E.T.J.M. van der Velden, C.H. Hulsbergen: Sediment concentration measurement by transverse suction, *Coastal Eng.* **11**, 353–370 (1987)
- 15.264 V.A. Vanoni: Transportation of suspended sediment by water, *ASCE Trans.* **111**(3), 67–102 (1946)
- 15.265 R.P. Apmann, R.R. Rumer: Diffusion of sediment in developing flow, *J. Hydraul. Div. ASCE* **96**(1), 109–123 (1970)
- 15.266 H.E. Jobson, W.W. Sayre: Vertical transfer in open channel flow, *J. Hydraul. Div. ASCE* **96**(3), 703–724 (1970)
- 15.267 N.L. Coleman: Velocity profiles with suspended sediment, *J. Hydraul. Res.* **19**(3), 211–229 (1981)
- 15.268 L.C. van Rijn: *Entrainment of Fine Sediment Particles, Development of Concentration Profiles in a Steady, Uniform Flow Without Initial Sediment Load*, Report on Model Investigation, Delft Hy-

- draulics Laboratory M1531 Part II (Delft Hydraulics Laboratory, Delft 1981)
- 15.269 T.A. Winterstein, H.G. Stefan: *Suspended Sediment Sampling in Flowing Water: Laboratory Study of the Effects of Nozzle Orientation, Withdrawal Rate and Particle Size*, External Memorandum M-168, St. Anthony Falls Hydraulic Laboratory (University of Minnesota, Minneapolis 1983)
  - 15.270 T.K. Edwards, G.D. Glysson: *Field Methods for Measurement of Fluvial Sediment: U.S.G.S. Techniques of Water-Resources Investigations* (USGS, Reston 1999)
  - 15.271 A.E. Hay: Sound scattering from a particle-laden turbulent jet, *J. Acoust. Soc. Am.* **90**(4), 2055–2074 (1991)
  - 15.272 M.E. Nelson, P.C. Benedict: Measurement and analysis of suspended sediment loads in streams, *Proc. ASCE* **76**(31), 1–28 (1950)
  - 15.273 E.T. Baker, J.W. Lavelle: The effect of particle size on the light attenuation coefficient of natural suspensions, *J. Geophys. Res.* **89**(C5), 8197–8203 (1984)
  - 15.274 J.P.-Y. Maa: Laboratory measurements of instantaneous sediment concentration under waves, *IEEE J. Oceanic Eng.* **13**(4), 299–302 (1988)
  - 15.275 N.J. Clifford, K.S. Richards, R.A. Brown, S.N. Lane: Laboratory and field assessment of an infrared turbidity probe and its response to particle size and variation in suspended sediment concentration, *Hydrol. Sci. J.* **40**(6), 771–791 (1995)
  - 15.276 J.P. Downing, R.W. Sternberg, C.R.B. Lister: New instrumentation for investigation of sediment suspension in the shallow marine environment, *Marine Geol.* **42**, 19–34 (1981)
  - 15.277 D&A Instrument Company: *OBS-3 Product Information* (D&A Instrument Company, Port Townsend 2005)
  - 15.278 R.A. Beach, R.W. Sternberg, R. Johnson: A fiber optic sensor for monitoring suspended sediment, *Marine Geol.* **103**, 513–520 (1992)
  - 15.279 P.D. Osborne, C.E. Vincent, B. Greenwood: Measurement of suspended sand concentrations in the nearshore: Field intercomparison of optical and acoustic backscatter sensors, *Continental Shelf Res.* **14**(2/3), 159–174 (1994)
  - 15.280 M.O. Green, J.D. Boon III: The measurement of constituent concentrations in nonhomogeneous sediment suspensions using optical backscatter sensors, *Marine Geol.* **110**, 73–81 (1993)
  - 15.281 T.F. Sutherland, P.M. Lane, C.L. Amos, J. Downing: The calibration of optical backscatter sensors for suspended sediment of varying darkness levels, *Marine Geol.* **162**, 587–597 (2000)
  - 15.282 D.H. Schoellhamer: Biological interference of optical backscatterance sensors in Tampa Bay, Florida, *Marine Geol.* **110**, 303–313 (1993)
  - 15.283 P. Ridd, G. Day, S. Thomas, J. Harradence, D. Fox, J. Bunt, O. Renagi, C. Jago: Measurement of sediment deposition rates using an optical backscatter sensor, *Estuarine, Coastal Shelf Sci.* **52**, 155–163 (2001)
  - 15.284 J.A. Puleo, R.A. Beach, R.A. Holman, J.S. Allen: Swash zone sediment suspension and transport and the importance of bore-generated turbulence, *J. Geophys. Res.* **105**(C7), 17021–17044 (2000)
  - 15.285 D.J. Law, A.J. Bale, S.E. Jones: Adaptation of focused beam reflectance measurement to in-situ particle sizing in estuaries and coastal waters, *Marine Geol.* **140**, 47–59 (1997)
  - 15.286 J.M. Phillips, D.E. Walling: Calibration of a Par-Tec 200 laser back-scatter probe for in situ sizing of fluvial suspended sediment, *Hydrol. Processes* **12**, 221–231 (1998)
  - 15.287 A.R. Heath, P.D. Fawell, P.A. Bahri, J.D. Swift: Estimating average particle size by focused beam reflectance measurement (FBRM), Part. Part. Syst. Char. **19**, 84–95 (2002)
  - 15.288 Y.C. Agrawal, H.C. Pottsmith: Laser diffraction particle sizing in STRESS, *Cont. Shelf Res.* **14**, 1101–1121 (1994)
  - 15.289 Y.C. Agrawal, H.C. Pottsmith: Instruments for particle size and settling velocity observations in sediment transport, *Marine Geol.* **168**, 89–114 (2000)
  - 15.290 Sequoia Scientific Inc.: *LISST-100 Product Information* (Sequoia Scientific, Redmond 2005)
  - 15.291 J.W. Gartner: Estimating suspended solids concentrations from backscatter intensity measured by acoustic Doppler current profiler in San Francisco Bay, California, *Marine Geol.* **211**, 169–187 (2004)
  - 15.292 D.M. Admiraal, R. Musalem, M.H. García: A Study of self-formed ripples using Particle Image Velocimetry (PIV), 4th IAHR Symposium on River, Coastal, and Estuarine Morphodynamics, Barcelona (IAHR, Delft 2003)
  - 15.293 I. Nezu, R. Azuma: Turbulence characteristics and interaction between particles and fluid in particle-laden open channel flows, *J. Hydraul. Eng.* **130**(10), 988–1001 (2004)
  - 15.294 S.C. Knowles, J.T. Wells: In situ aggregate analysis camera (ISAAC): A quantitative tool for analyzing fine-grained suspended material, *Limnol. Oceanogr.* **43**(8), 1954–1962 (1998)
  - 15.295 C. Libicki, K.W. Bedford, J.F. Lynch: The interpretation and evaluation of a 3 MHz acoustic backscatter device for measuring benthic boundary layer sediment dynamics, *J. Acoust. Soc. Am.* **85**(4), 1501–1511 (1989)
  - 15.296 A.E. Hay, J. Sheng: Vertical profiles of suspended sand concentration and size from multifrequency acoustic backscatter, *J. Geophys. Res.* **97**(C10), 15661–15677 (1992)
  - 15.297 C. Shen, U. Lemmin: Application of an acoustic particle flux profiler, *J. Hydraul. Res.* **37**(3), 407–419 (1999)
  - 15.298 D.M. Admiraal, M.H. García: Laboratory measurement of suspended sediment concentration using

- an Acoustic Concentration Profiler (ACP), *Exp. Fluids* **28**, 116–127 (2000)
- 15.299 M.G. Kleinbans, W.B.M. Ten Brinke: Accuracy of cross-channel sampled sediment transport in large sand-gravel-bed rivers, *J. Hydraul. Eng.* **127**(4), 258–269 (2001)
- 15.300 P.D. Thorne, D.M. Hanes: A review of acoustic measurement of small-scale sediment processes, *Continental Shelf Res.* **22**, 603–632 (2002)
- 15.301 A.M. Crawford, A.E. Hay: Determining suspended sand size and concentration from multifrequency acoustic backscatter, *J. Acoust. Soc. Am.* **94**(6), 3312–3324 (1993)
- 15.302 J.F. Lynch, J.D. Irish, C.R. Sherwood, Y.C. Agrawal: Determining suspended sediment particle size information from acoustical and optical backscatter measurements, *Continental Shelf Res.* **14**(10/11), 1139–1165 (1994)
- 15.303 P.D. Thorne, S.C. Campbell: Backscattering by a suspension of spheres, *J. Acoust. Soc. Am.* **92**(2), 978–986 (1992)
- 15.304 P.D. Thorne, P.J. Hardcastle, R.L. Soulsby: Analysis of acoustic measurements of suspended sediments, *J. Geophys. Res.* **98**(C1), 899–910 (1993)
- 15.305 F.H. Fisher, V.P. Simmons: Sound absorption in sea water, *J. Acoust. Soc. Am.* **62**(3), 558–564 (1977)
- 15.306 P.D. Thorne, G.P. Holdaway, P.J. Hardcastle: Constraining acoustic backscatter estimates of suspended sediment concentration profiles using the bed echo, *J. Acoust. Soc. Am.* **98**(4), 2280–2288 (1995)
- 15.307 L. Zedel, A. Hay: A coherent Doppler profiler for high-resolution particle velocimetry in the ocean: Laboratory measurements of turbulence and particle flux, *J. Atmos. Oceanic Technol.* **16**, 1102–1117 (1999)
- 15.308 C. Shen, U. Lemmin: A two-dimensional acoustic sediment flux profiler, *Meas. Sci. Technol.* **8**, 880–884 (1997)
- 15.309 K.F. Betteridge, P.D. Thorne, P.S. Bell: Assessment of acoustic coherent Doppler and cross-correlation techniques for measuring near-bed velocity and suspended sediment profiles in the marine environment, *J. Atmos. Oceanic Technol.* **19**, 367–380 (2002)
- 15.310 G.P. Holdaway, P.D. Thorne, D. Flatt, S.E. Jones, D. Prandle: Comparison between ADCP and transmissometer measurements of suspended sediment concentration, *Continental Shelf Res.* **19**(3), 421–441 (1999)
- 15.311 W.W. Emmett: *A Field Calibration of the Sediment-Trapping Characteristics of the Helley-Smith Bed Load Sampler*, US Geological Survey Professional Paper 1139 (USGS, Washington 1980)
- 15.312 E.J. Helley, W. Smith: Development and calibration of a pressure-difference bedload sampler, *US Geol. Survey Open-File Rep.* **73-108**, 18 (1971)
- 15.313 J.M. Gaudet, A.G. Roy, J.L. Best: Effect of orientation and size of Helley-Smith sampler on its efficiency, *J. Hydraul. Eng.* **120**(6), 758–767 (1994)
- 15.314 D.W. Hubbell, H.H. Stevens Jr., J.V. Skinner, J.P. Beverage: New approach to calibrating bed load samplers, *J. Hydraul. Eng.* **111**(4), 677–694 (1985)
- 15.315 S.M. Sterling, M. Church: Sediment trapping characteristics of a pit trap and the Helley-Smith sampler in a cobble gravel bed river, *Water Resour. Res.* **38**(8), 10.1029/2000WR000052 (2002)
- 15.316 K. Bunte, S.R. Abt, J.P. Potyondy, S.E. Ryan: Measurement of coarse gravel and cobble transport using portable bedload traps, *J. Hydraul. Eng.* **130**(9), 879–893 (2004)
- 15.317 M.T.K. Gaweesh, L.C. van Rijn: Bed-load sampling in sand-bed rivers, *J. Hydraul. Eng.* **120**(12), 1364–1384 (1994)
- 15.318 K.T. Lee, Y.L. Liu, K.H. Cheng: Experimental investigation of bedload transport processes under unsteady flow conditions, *Hydrol. Processes* **18**, 2439–2454 (2004)
- 15.319 D.W.T. Jackson: A new, instantaneous aeolian sand trap design for field use, *Sedimentology* **43**, 791–796 (1996)
- 15.320 B.O. Bauer, S.L. Namikas: Design and field test of a continuously weighing, tipping-bucket assembly for Aeolian sand traps, *Earth Surf. Processes Landforms* **23**, 1171–1183 (1998)
- 15.321 C.D. Rennie, R.G. Millar, M.A. Church: Measurement of bed load velocity using an acoustic Doppler current profiler, *J. Hydraul. Eng.* **128**(5), 473–483 (2002)
- 15.322 C.D. Rennie, R.G. Millar: Measurement of the spatial distribution of fluvial bedload transport velocity in both sand and gravel, *Earth Surf. Processes Landforms* **29**, 1173–1193 (2004)
- 15.323 P.C. Benedict, M.L. Albertson, M.Q. Matejka: Total sediment load measured in turbulence flume, *Trans. ASCE*, Vol. 120 (1955) 457–488, Paper 2750